Quantum Cavity Optomechanics with Phononic Bandgap Shielded Silicon Nitride Membranes

PhD Thesis

William H. P. Nielsen

May 2016

Academic supervisor: prof. Eugene S. Polzik

This thesis has been submitted to the PhD School of The Faculty of Science, University of Copenhagen.

The Ground State is just another word for nothing left to lose…

Tilegnet Maria og hendes søskende.

Acknowledgements

Getting here, to the end of the PhD, was a long haul. I am very grateful to the many people who helped me, in one way or another, to make it this far. In the following, I present my best effort to name and thank each one of you. Should this list be incomplete, I ask for your forgiveness.

First and foremost, I am of course thankful to prof. Eugene Polzik for letting me have four years of opportunities in his research group (in spite of having previously supervised my bachelor's project!). Eugene has proven a patient supervisor in the face of a sometimes very slow progress, and a daring researcher in venturing into optomechanics in the first place. I can still recall my awe when Eugene revealed that my cryostat was the first one he had ever worked with. I admire Eugene's scientific courage and especially his attitude of sharing knowledge and cooperating broadly.

In terms of the work presented here, dr. Albert Schließer, my unofficial supervisor, has been of immense importance in pushing the experiment forwards and interpreting the alternatingly perplexing and encouraging numbers and phenomena seen in the laboratory. I have no doubt that the laboratory I am now leaving is destined for glory.

Life as a PhD student is really about learning. Many people besides Eugene and Albert have taught and trained me. In a semi-chronological order, I would like to thank dr. Koji Usami for alleviating a lot of my initial confusion, pointing me to the relevant literature, and for sharing your deep belief of what science is really about. I agree. Dr. Dalziel Wilson, also for assisting my baby steps, and for an indispensable thesis I have consulted countless times. Dr. Jürgen Appel and dr. Jörg Helge Müller are both masters of the noble art of de-confusing confused students and are both willing to spend hours helping a fellow experimentalist in need. I have benefited massively from your readiness to explain. Also, Jörg plays a mean guitar, but you should really play louder.

Life as a PhD student would be unbearable without the comradeship between students. Of fellow students (and a single post-doc), I would like to thank: Yeghishe

Tsaturyan, without your fabrication and dedication there would hardly even be a membrane lab. You are a true Samaritan in the way you constantly save the rest of us close to deadlines. Christoffer Møller, also a great guy to do time with in the Dungeon, I am amazed by your diligence and persistently good spirits. I apologise for all the foul outbursts of frustration you and Yeghishe had to listen through. Merry chums also include: Willi Carlsen (miss your jokes), Andi Barg (great questions, great drumming), Andreas Næsby (I should have listened more to your advice), Yannick Seis (thanks for trying), Anders Simonsen (I appreciate your honesty), Dr. Stefan Christensen (thank you for everything: my PhD, Python and PGFplots), Dr. Jean-Baptiste Béguin (you are a *true* scientist), Γιώργος Βασιλάκης (let us never finish this conversation), Rodrigo Thomas (the buffest guy I know), and every former, present, and future member of The Unresolved Sideband. Special gratitude: Dominik Vogel, who left the lab but stayed in our hearts.

On the home front, I would first and foremost like to thank my wife for displaying an almost saintly toleration of the long working hours and accompanying absent-mindedness when I was eventually home. Serdecznie dziękuję Ci, kwiatuszku mój, za cierpliwość i miłość. Also my parents should be thanked for their patience. I guess there is no life on Mars, but at least Major Tom may finally reach ground control. True friends Frederik, Martin, and Naja, I thank you for your support. And of course Maria, who never failed to remind me what is important in life, and why I should get myself together and finish the project; how can I possibly repay you?

Regarding the actual document at hand, it would certainly have looked a lot worse had it not been for the amazing generosity of free (as in freedom) software developers. I am extremely indebted to the creators and maintainers of Python, Inkscape, Emacs, LaTeX, and PGFPlots. You are the unsung heroes of science; thank you. Also Alexander Franzen deserves honourable mention for his shared svg-library of optical components.

Finally, above all, I would like to express my gratitude by recalling the words of the Evangelist:

Sic et vos, cum feceritis omnia, quae praecepta sunt vobis, dicite: "Servi inutiles sumus; quod debuimus facere, fecimus."

Lucas 17,10

Abstract

Cavity optomechanics, a field which has matured tremendously over the last decade, has conclusively reached the quantum regime. Noteworthy experimental achievements include cooling of the vibrational motion of macroscopic objects to the quantum ground state, the observation of shot noise of radiation pressure, and the achievement of strong correlations between light at mechanics, manifested as ponderomotive squeezing. The next step invariably seems to be the incorporation of cavity optomechanical systems in more complex constellations, in some sense mimicking what has already been achieved with atoms.

In this work, we report on the progress of bringing a cavity optomechanical system "up to speed" for the later integration into a hybrid atomic-optical-mechanical entanglement experiment. The optomechanical system in consideration consists of a highly stressed stoichiometric silicon-nitride membrane placed between two highly reflective mirrors, all of which are embedded in a helium flow cryostat. In order to reach truly quantum territory, severe shielding of the membrane from the environment is required, as well as meticulous concern for auxiliary sources of noise, both from the laser and mirrors used.

The purpose of this thesis is to document the development of the experiment from its initial stages to its final quantum enabled incarnation, as well as to provide the necessary theoretical machinery to interpret the experimental results. A strong emphasis is placed on the unique challenges posed by our unique *monolithic* cavity design and how to understand and overcome them.

The evolution of the experiment was successful, and we conclude that the quantum regime has been reached. Our main result is the observation of simultaneous ponderomotive squeezing from more than 13 mechanical modes, the strongest of which suppresses the light noise by -2.4 dB, implying the hitherto strongest correlations observed between light and mechanics. A secondary result is the cooling of the mechanical motion close to the quantum ground state.

Sammenfatning

Kavitets-optomekanik, et forskningsfelt der i løbet af det seneste årti har oplevet en rivende udvikling, har endegyldigt nået kvanteregimet. Af spektakulære eksperimentelle bedrifter kan nævnes den lysmedierede køling af en makroskopisk genstands bevægelse til den kvantemekaniske grundtilstand, observationen af lysstrålingstrykkets kvantemekaniske haglstøj samt opnåelsen af stærke korrelationer mellem lys og mekanisk bevægelse, konkret givende sig til kende som ponderomotorisk klemt lys. Det næste skridt i denne udvikling må uundgåeligt være sammenføjningen af kavitets-optomekaniske systemer med andre kvanteoptiske elementer, i en hvis forstand den samme udvikling som atomare ensembler har gennemlevet.

I det foreliggende arbejde beretter vi om de eksperimentelle fremskridt i forbindelse med at klargøre et sådant kavitets-optomekanisk system til senere at kunne indgå som en del af et hybridt atomar-optisk-mekanisk sammenfiltringseksperiment. Det optomekaniske system, der er genstand for vore betragtninger, består af en højst udspændt støkiometrisk mebran af siliciumnitrid anbragt mellem to højreflektive spejle, altsammen indeholdt i en heliumflow-kryostat. For for alvor at kunne sætte vores eksperimentelle fødder på solid kvantegrund, er en betydelig afskærmning af membranen fra dens omgivelse nødvendig, ligesom en omhyggelig keren sig om udefrakommende støjkilder, såvel fra lyset som spejlene, er påkrævet.

Formålet med denne afhandling er at dokumentere eksperimentets udvikling fra dets spæde fase til den endelige inkarnation, såvel som at tilvejebringe den for forståelsen og fortolkningen af de eksperimentelle resultater nødvendige kvantemekaniske teorimængde. Fokus lægges især på beskrivelsen af de for vores *monolitiske* kavitetsdesign særegne udfordringer og hvorledes disse overvindes.

Eksperimentets udvikling var tilfredsstillende, og vi slutter at kvante-regimet er blevet nået. Vores hovedresultat er observationen af samtidig ponderomotorisk lys-klemning hidrørende fra mere end 13 mekaniske svingingstilstande, den kraftigste af hvilke klemmer lysstøjen med end -2.4 dB, hvilket indikerer den hidtil stærkeste korrelation observeret mellem lys og mekanik. Et sekundært resultat

består af kølingen af den mekaniske bevægelse til området nær kvante-grundtilstanden.

Publications and presentations

Peer-review publication

[Nielsen, 2016] Nielsen, W. H. P., Tsaturyan, Y., Møller, C., Schliesser, A. and Polzik, E. S. (2016). Multimode optomechanical system in the quantum regime, *Submitted for publication*

Conference presentations

[Nielsen, 2015] Nielsen, W. H. P., Møller, C., Tsaturyan, Y., Carlsen, W., Schließer, A. and Polzik, E. S. (2015). Membrane-in-the-middle optomechanical system with a quantum cooperavity exceeding unity, *Macroscopic Quantum Coherence*, St. Andrews, poster presentation.

[Nielsen, 2014] Nielsen, W. H. P., Tsaturyan, Y., Møller, C., Barg, A., Simonsen, A., Schließer, A. and Polzik, E. S. (2014). Towards quantum optomechanics with phononic bandgap shielded membranes, *21st Central European Workshop on Quantum Optics*, Brussels, poster presentation.

Contents

Chapter 1

Introduction

In this work, we present the progress of an experimental project, the goal of which was to create an optomechanical system displaying true quantum behaviour. In the course of this PhD project, the system, which consists of a rectangular high-stress silicon nitride (Si_3N_4) membrane placed between two highly reflective mirrors embedded in a helium flow cryostat, was developed from a bare minimum[1] to a fully multimode *quantum enabled* platform. To ascertain the "quantumness" of the system, two separate goals where pursued. First, it was attempted to sideband cool a single vibrational mode of the membrane (as close as possible) to its quantum ground state. Second, ponderomotive squeezing of light, also a clear signature of a quantum enabled interaction, was pursued. The former goal was not conclusively reached, whereas the second certainly was.

The thesis is structured as follows. In this introductory chapter, we first, in section 1.1, take a bird's eye view of the field of optomechanics and present where our own experimental work fits into this diverse picture, and then proceed, in section 1.2, to give a conceptual walkthrough of the experiment. A student new to this field will hopefully find section 1.2 to be a good initial exposition.

Chapter 2 is concerned with the formal theoretical aspects of the system and system dynamics. We cover the subjects necessary to anticipate and interpret the experimental outcomes, and specify the concept of a system being quantum enabled.

Chapter 3 deals with our particular experimental approach to cavity optomechanics, first explaining how the experiment is built and operated, then proceeding to discuss the different optimisation procedures involved in eventually reaching a large quantum cooperativity.

[1] Literally an empty laboratory.

Finally, chapter 4 presents and discusses the evidence that the interaction of our study is indeed showing its quantum nature. An outlook is also given, pointing to the interesting experimental avenues opened up by reaching the quantum regime.

1.1 The Background

1.1.1 A Brief History of Optomechanics Before 2012

On 11 February 2016, a truly historical scientific discovery was announced. In a coordinated live-streamed press conference and paper publication [Abbott et al., 2016], the LIGO scientific collaboration announced the first ever direct observation of gravitational waves. With the detection, which took place on 14 September 2015, and the announcement coinciding with the centennials of respectively Albert Einstein's theory of general relativity [Einstein, 1915] and his prediction of gravitational waves [Einstein, 1916], there was a sense of closure to the discovery. As if though a long and strenuous quest including decades of experimental optimisation of gravitational wave detectors had now *finally* paid off, and Einstein was at long last proven right. For a researcher in the field of optomechanics, however, the groundwork of the gravitational wave detection community had already paid off decades earlier.

In the late 1960's, V. Braginsky and his collaborators, fundamentally concerned with the precision limits of interferometric sensing, pioneered, both theoretically [Braginsky and Manukin, 1967] and experimentally [Braginsky et al., 1970], the field of (microwave) optomechanics by demonstrating how the radiation pressure force may cool or heat a harmonically suspended cavity mirror. That inherently *quantum* effects, namely the quantum fluctuations of the radiation pressure force, pose a limit for the sensitivity of gravitational wave detectors was pointed out by C. Caves in 1980 [Caves, 1980], who one year later proposed a visionary idea to overcome this limitation by the injection of squeezed light [Caves, 1981] into the detection interferometer[2]. The realisation that quantum effects play a role in the interferometric detection of large scale cosmological phenomena such as gravitational waves is in itself remarkable, but it also paves the way for a different field of study: quantum optomechanics. If light and mechanics (as embodied by the moving mirrors in the interferometer) can interact in a way that is intrinsically

[2]This was recently realised experimentally in two different gravitational wave detectors, the British-German GEO 600 [Grote et al., 2013] and the aforementioned American LIGO [The LIGO Scientific Collaboration, 2013].

quantum mechanical, then surely that interaction is worth studying in its own right.

In the 1990's, theoretical work on quantum cavity optomechanics started emerging. Of particular interest to this work is optomechanically induced (ponderomotive) squeezing of light [Fabre et al., 1994] [Mancini and Tombesi, 1994], but as diverse proposals as the generation of non-classical states (both of light and mechanics) [Bose et al., 1997] [Mancini et al., 2002], feedback cooling of the mirror temperature [Mancini et al., 1998], quantum non-demolition measurements of the intra-cavity light field [Braginsky and Khalili, 1992], and even the quantum superposition of a massive mirror [Marshall et al., 2003] emerged. In other words, a broad theoretical foundation was in place, and the world was hungry for experiments.

Roughly a decade later, strong progress in micro- and nano-fabrication technologies had allowed for the realisation of a multitude of devices. Although early feedback cooling results [Cohadon et al., 1999] were achieved with large mirrors, to eventually reach the regime where quantum effects show, small masses, low mechanical dissipation, and good optical qualities were simultaneously needed. It is beyond the scope of this introduction to describe the entire optomechanical device "zoo" and the exciting developments in the first decade of this century (see [Kippenberg and Vahala, 2007] and[Aspelmeyer et al., 2014] for broader reviews), but we nonetheless highlight four alternative approaches, mainly to set the stage for our own project, which began in 2012.

In the microwave regime, μm-small circular drums capacitively coupled to an LC circuit and precooled in a dilution refrigerator to mK-temperatures had been brought to operate in the strong coupling regime [Teufel et al., 2011b] and even sideband cooled to their motional ground state [Teufel et al., 2011a]. In the optical regime, optomechanical crystals allowing for the simultaneous localisation of optical and mechanical resonances [Eichenfield et al., 2009] that interact via radiation pressure, had also been cooled to the motional ground state [Chan et al., 2011], this time from a more modest pre-cooling using a helium flow cryostat. The latter of these approaches uses mechanical resonances in the GHz-regime, whereas the circular drums have resonance frequencies of tens of MHz. Also in the tens of MHz-range, the vibrational breathing modes of microtoroidial whispering-gallery mode resonators [Schliesser, 2010] had been brought to quantum-coherently interact with light [Verhagen et al., 2012]. These three approaches share the same heavy reliance of sophisticated fabrication procedures for the mechanical resonators. A different path was offered by the idea of embedding a *commercially* available Si_3N_4

membrane in a normal Fabry-Perot cavity [Thompson et al., 2008]. This system, also known as a membrane-in-the-middle system (or simply MIM), was not yet in the quantum regime, but showed great promise, owing in particular to the low optical losses and high mechanical quality factors of the membranes [Zwickl et al., 2008] [Wilson et al., 2009].

1.1.2 Our Project: Scope and Purpose

This was the state of the art in 2012, when the author started his project. In the QUANTOP lab, where the main expertise lay in the field of atom-light interaction, in particular that between atomic caesium ensembles and light (see e.g. [Sherson et al., 2006]), there was a wish to utilise the promising new optomechanical platforms as supplements to the caesium cells. In the long term, there was the prospect to entangle one such caesium cell with a mechanical oscillator [Hammerer et al., 2009], in a certain sense mimicking what had already been achieved between two atomic ensembles [Julsgaard et al., 2001]. What was needed was a quantum-enabled cavity optomechanical system. It was decided to pursue a membrane-in-the-middle approach to constitute the mechanical part of the hybrid experiment. The aim of this project then became to establish the mechanical part of said joint experiment, more precisely: to build a cavity optomechanical setup with high-stress silicon nitride membranes definitely operating in the quantum regime. The work at hand details the labour we undertook to finally reach that goal.

1.2 The Membrane in the Middle

We now give an illustrative outline of the experiment. Beyond the mere pedagogical purposes, we also establish most of the terminology and notation regarding cavities to be used throughout this work. We first introduce the basics about optical cavities and from there on guide the reader through the dynamics of our optomechanical system and the goals and objectives of the experiment. The aim of this section is to provide a conceptual overview, whereas chapter 2 deals with the more "nitty-gritty" theoretical aspects of the experiment.

1.2.1 Optical Cavities

All of the interesting physics in cavity optomechanics take place inside an optical cavity. Although cavities are named after the empty space *between* two reflecting surfaces, we here include the surfaces in the definition and take a cavity to consist of two mirrors with amplitude transmissivities t_1 and t_2 separated by a fixed distance L. Light shone into this cavity will be reflected back and forth from the surfaces interfering with itself, and a standing wave forms when the incoming light's frequency is an integer multiple of the cavity's free spectral range, FSR, given by

$$\mathrm{FSR} = \frac{c}{2L}, \tag{1.1}$$

where c is the speed of light. Note that the round-trip time of the cavity, τ, fulfils that $\tau^{-1} = \mathrm{FSR}$. In Figure 1.1 the

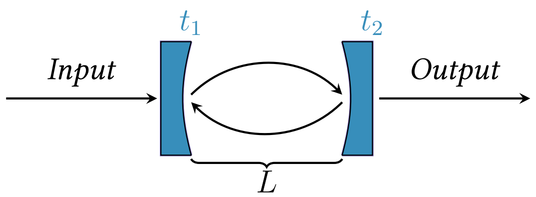

Figure 1.1: A sketch defining the incoupling and outcoupling mirrors.

The light eventually leaves the cavity. We shall consistently take the light to emanate from a monochromatic laser source and enter the cavity via the first mirror. Then the light may either be reflected back out through mirror one, transmitted out through the second mirror, or be lost through some other mechanism. These three processes happen at rates κ_R, κ_T, and κ_L, respectively. The total rate, κ, at which light leaves the cavity is then given by

$$\kappa = \kappa_R + \kappa_T + \kappa_L. \tag{1.2}$$

The reflection and transmission rates relate to the mirror transmissivities as

$$\kappa_R = \frac{1}{\tau}|t_1|^2, \quad \kappa_T = \frac{1}{\tau}|t_2|^2. \tag{1.3}$$

When detecting signals from the cavity, it is useful to quantify the amount of light coming out of the port (mirror) where one is detecting. We always detect in transmission. The quantification is captured by the cavity coupling parameter, η_c, given by

$$\eta_c = \frac{\kappa_T}{\kappa}. \tag{1.4}$$

A cavity for which $\eta_c > 1/2$ is said to be overcoupled[3]. From the viewpoint of the detector, a fraction of $1 - \eta_c$ of the intra-cavitylight is lost (never detected), and

3Similarly, a cavity for which $\eta_c < 1/2$ is undercoupled, whereas $\eta_c = 1/2$ corresponds to a critically coupled cavity.

it is therefore usually advantageous to maximise η_c. We now explore the role of η_c a little. For the rest of this section, we assume κ_L=0. Exactly on resonance, the ratio between incoming power, $|s_{\text{in}}|^2$, and transmitted power, $|s_{\text{out}}|^2$, is given (in the limit of highly reflective mirrors) by [Siegman, 1986, section 11.4]

$$\frac{|s_{\text{out}}|^2}{|s_{\text{in}}|^2} = \frac{4T_1T_2}{(T_1+T_2)^2} = 4\eta_c(1-\eta_c), \tag{1.5}$$

which is clearly maximal when $\eta_c = 1/2$.

It is important to consider what happens when the laser frequency is changed around the cavity resonance. The intracavity field, a, normalised such that $|a|^2$ is the intra-cavity energy, fulfils the following differential equation (derived in [Haus, 1984, chapter 7], cf. equation (2.98)):

$$\frac{\mathrm{d}}{\mathrm{d}t}a(t) = (\mathrm{i}\Delta - \kappa/2)a(t) + \sqrt{(1-\eta_c)\kappa}s_{\text{in}}(t), \tag{1.6}$$

where Δ, the detuning, is the frequency difference between the laser and the cavity resonance. In the steady-state, the intra-cavity field then satisfies that

$$a = \frac{\sqrt{(1-\eta_c)\kappa}s_{\text{in}}}{\mathrm{i}\Delta - \kappa/2}, \tag{1.7}$$

whence it follows that

$$|a|^2 = (1-\eta_c)|s_{\text{in}}|^2\frac{\kappa}{\Delta^2+\kappa^2/4}. \tag{1.8}$$

i.e. the cavity responds to variations of the laser frequency with a Lorentzian curve with a full-width-half-maximum (FWHM) of κ. The resonance is reached when $\Delta = 0$ and the point of steepest slope when $\Delta = \pm\kappa/2\sqrt{3}$, where the slope is $\mp 3\sqrt{3}/\kappa^2$.

The output power is the intra-cavity energy times the output transmission rate; $|s_{\text{out}}|^2 = \eta_c\kappa|a|^2$, implying that on resonance

$$\frac{|s_{\text{out}}|^2}{|s_{\text{in}}|^2} = 4\eta_c(1-\eta_c), \tag{1.9}$$

in agreement with equation (1.5). The intra-cavity power, $|s|^2$, may build up to a very large value, depending on the mirror transmissivities and external losses. On resonance,

$$|s|^2 = \frac{4(1-\eta_c)}{\kappa\tau}|s_{\text{in}}|^2 = \frac{\mathcal{F}}{2\pi}4(1-\eta_c)|s_{\text{in}}|^2, \tag{1.10}$$

where we have introduced the cavity finesse, defined as the ratio between the free spectral range and the FWHM of the cavity response;

$$\mathcal{F} := 2\pi\frac{\text{FSR}}{\kappa}, \tag{1.11}$$

where the 2π accounts for the fact that κ is in angular units whereas the FSR is in Hz. The finesse is the figure of merit for the goodness of an optical cavity, and generally speaking, more is better. In our setup we actually have a *tunable* finesse, which we describe in section 3.5.

1.2.2 Optomechanical Cavities

We now consider the case of a cavity with a moving element. Canonically, this is taken to be the end mirror (see section 2.3), although the system of our study has the moving element inside the cavity. The resulting physics of the two situations are very similar, and for the sake of illustration, it is unnecessary to delve into their differences (we do that in section 2.4). Specifically, a dielectric Si_3N_4 membrane is placed between two highly-reflecting mirrors. In Figure 1.2, three descriptive depictions of the setup are shown.

Since the membrane thickness d is considerably smaller than the wavelength λ of the light (usual numbers: $d \sim 50\,\text{nm}$, $\lambda \sim 800\,\text{nm}$), the membrane changes, as it moves in the intra-cavity standing wave, the effective optical cavity length via its refractive index, which is different from unity. This is illustrated in Figure 1.2B. A small change in cavity length slightly displaces all cavity resonances, which is equivalent to the laser detuning slightly changing. From equation (1.8) we therefore expect a modulation of the intra-cavity field and thus also of the transmitted light. This is the basic mechanism allowing for read-out of the membrane motion. Said modulation is illustrated in Figure 1.2C, where a certain membrane position (green) maps to a particular output power (orange). For a given cavity length, it is clear that higher finesse leads to a higher sensitivity via the increase in cavity line-shape slope. Just how much the frequency changes when the membrane surface moves a given amount is encapsulated by the optomechanical coupling parameter G;

$$G = \frac{\partial \omega_c}{\partial z_m}, \tag{1.12}$$

where ω_c is the cavity resonance (angular) frequency and z_m is the membrane position. For a cavity with a moving end mirror, the model we are adopting in this

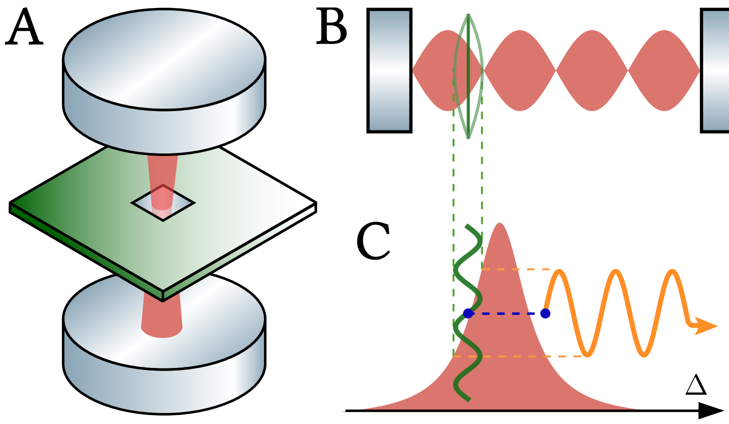

Figure 1.2: Three illustrations of our optomechanical system. A: The actual geometry. B: The membrane moving in the standing wave of the cavity. C: The effect of the membrane's motion on the light transmitted from the cavity. The oscillation amplitudes are highly exaggerated.

chapter[4], it holds that $\omega_c = 2\pi nc/2L$, where n is an integer. As $L \to L + z_m$, we therefore have to first order that

$$G = \frac{\partial}{\partial z_m} \frac{2\pi nc}{2(L+z_m)}\bigg|_{z_m=0} = \frac{\omega_c}{L}. \tag{1.13}$$

It is not only the membrane position that determines amount of intra-cavity light; the light also acts on the membrane via the radiation-pressure force and thereby displaces the membrane. It is this interplay that in a certain sense *is* optomechanics. Each photon scattered off the membrane surface imparts a momentum change Δp, given by

$$\Delta p = 2\hbar k, \tag{1.14}$$

where k is the photon wavenumber. If we designate the total number of intra-cavity photons as $\bar{n}_{\text{cav}}$, the total force arising from the radiation pressure is then

$$F_{\text{RP}} = \frac{\Delta p}{\tau}\bar{n}_{\text{cav}} = \hbar G \bar{n}_{\text{cav}}. \tag{1.15}$$

At this point, we may reflect a little on the design of our optomechanical experiment. In order to achieve a large optomechanical coupling, a high-finesse cavity will be helpful in providing a large build-up of intra-cavity power. Also, a short

[4]We stress that having the mechanically compliant element between the mirrors rather than as the end mirror makes no conceptual difference, and that the differences that nonetheless withstand between the two geometries are discussed in section 2.4.

cavity will yield a large G, suggesting that we should make the cavity as short as possible. Now, as the cavity linewidth is inversely proportional to the cavity length, things are slightly more involved, but it turns out that a short cavity *is* favourable for optimising the light-mechanical interaction (see section 3.4). A short cavity is also helpful in another aspect, namely that of focusing the beam.

The membrane has different mechanical modes, an example of which is shown in Figure 1.3. The modes are characterised by the number of antinodes, n and m, in each direction of the membrane. In order to properly sample the motion of such a mechanical mode, the beam width of the optical mode at the membrane position should be smaller than half the wavelength of the mechanical standing wave (we treat this subject in more depth in section 3.6.1). A typical membrane has a side length of $L_{\text{mem}} \approx 500\,\mu\text{m}$ and the mechanical wavelengths scale according to $\lambda_n^{\text{mech}} = 2L_{\text{mem}}/n$.

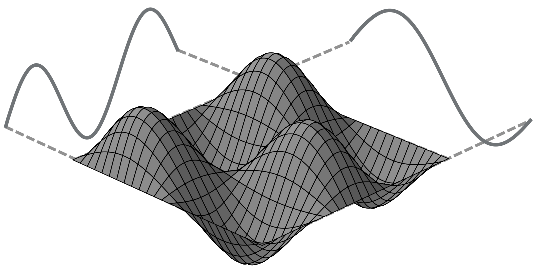

Figure 1.3: An example of a membrane mode. Here, $n = 3$ and $m = 2$.

Our cavity consists of a plano-concave mirror (mirror 1, the incoupler mirror) with a radius of curvature $R = 2.5\,\text{cm}$ and a flat mirror (mirror 2, the outcoupler mirror). From standard Gaussian optics [Milonni and Eberly, 1988, chapter 14], we may then calculate the intra-cavity beam waist, w_0, which for stability reasons must be at the flat mirror, by propagating the complex beam parameter, q, through the cavity. Specifically, q must fulfil that

$$q = \frac{Aq + B}{Cq + D}, \tag{1.16}$$

where

$$\begin{bmatrix} A & B \\ C & D \end{bmatrix} = \begin{bmatrix} 1 - \frac{2L}{R} & L\left(1 - \frac{2L}{R}\right) + L \\ -\frac{2}{R} & 1 - \frac{2L}{R} \end{bmatrix}. \tag{1.17}$$

The cavity waist is then found from the relation

$$w_0 = \left(\text{Im}(q^{-1})\frac{\pi}{\lambda}\right)^{-\frac{1}{2}}, \tag{1.18}$$

and propagated to the membrane position using that

$$w(z) = w_0 \sqrt{1 + \left(\frac{z\lambda}{\pi w_0}\right)^2}. \tag{1.19}$$

In Figure 1.4 we display the resulting beam widths. The length or our optical cavity is $\sim 1.5\,\mathrm{mm}$, yielding a beam width of $40\,\mu\mathrm{m}$, meaning that we can resolve membrane modes up to ~ 10.

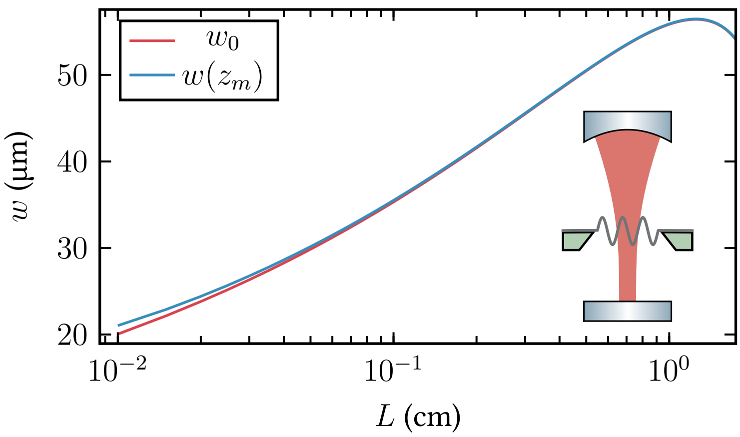

Figure 1.4: The obtainable beam width. The inset illustrates the transverse overlap between the membrane and optical mode.

1.2.3 Quantum Coherent Interaction

After the preliminary considerations regarding the optomechanical cavity, we now turn our attention to the quantum aspects of the light-mechanical interaction. The goal of this work is to realise an optomechanical setup that is somehow *quantum enabled*, meaning, on a conceptual level, that clear quantum mechanical signatures arise from the interaction. Owing to the macroscopic dimensions of the membrane resonators, this is by no means trivial.

In the course of the experiment, any mechanical mode of the membrane will be in a thermal state. A nice intuition is offered by the picture of a system in a thermal state being really always in a *coherent* state, but jumping between these on a time scale of the mechanical decoherence. In this picture, the membrane may interact *coherently* with the light provided that the interaction happens sufficiently quickly. It must, however, be appreciably slow that the membrane mode completes at least *one* oscillation period. Let us recast this intuition in formulae.

In the presence of a thermal bath at temperature T, a membrane mode of frequency ω_m has an equilibrium phonon occupation, $\bar{n}_{\text{th}}$, given by

$$\bar{n}_{\text{th}} = \frac{k_B T}{\hbar\omega_m}. \tag{1.20}$$

The rate at which a phonon jumps in or out of the mechanical mode (making the system transition to a new coherent state) is the occupation times the mechanical dissipation rate, Γ_m. The demand that this rate be lower than the mechanical frequency may then be expressed as

$$\frac{\omega_m}{\Gamma_m \bar{n}_{\text{th}}} > 1, \quad \text{or, equivalently,} \quad \frac{\hbar Q \omega_m}{k_B T} > 1, \tag{1.21}$$

where we have introduced the mechanical quality factor, Q, defined as the ratio ω_m/Γ_m. The condition of equation (1.21) provides a good preconception for the experimental demands on the mechanics. The membranes should be cold, preferably fast and have as high quality factors as possible. For frequencies in the MHz-range as offered by our samples, with ambient temperatures reachable with a helium cryostat (4 K-10 K), quality factors of more than 10^7 are necessary. This is a very high number, not yet available when the author embarked on his project. In section 3.7 we explain how it was eventually reached.

Having quantum "ready" mechanics does not imply having a quantum enabled system. As we shall see repeatedly in chapter 2, the condition for a quantum enabled interaction is that the quantum cooperativty, C_q exceeds unity,

$$C_q = \frac{4g^2}{\kappa \Gamma_m T} > 1, \tag{1.22}$$

where g is the cavity-enhanced coupling rate (to be defined in equation (2.75)). Both conditions can summarised as $\hbar\omega_m^2, 4g^2/\kappa > \Gamma_m \bar{n}_{\text{th}}$, highlighting the necessity of as low mechanical dissipation as possible.

This concludes our tutorial presentation. In the next chapter, where we cover the body of formal theory used in characterising and understanding the system, we shall see more concrete examples of the utility of the quantum cooperativity as a figure of merit for quantum-enabledness.

Chapter 2

Theoretical Considerations

In this chapter we present the body of formal theory needed to describe the experiment. The chapter is meant to be self-contained, although most of the motivation for the theory has to be drawn from the preceding and subsequent chapter. The topics covered span a very wide range, and we do not intend this exposition to be exhaustive. Instead, this chapter can be viewed as the minimal necessary and sufficient requirements for predicting and interpreting the experimental outcomes of the experiment. Despite this formal setting, we attempt to make references to the real experiment throughout the chapter.

2.1 Spectral Analysis

In the end, this work is concerned with examining power spectral densities and extracting optomechanical dynamics from those. We therefore start out with an overview of the spectral analysis involved, thereby also establishing the notation and instituting the conventions followed. This section is very brief in form.

2.1.1 Fourier Transforms

We define the Fourier transform of a signal, $s(t)$, as

$$\mathcal{F}[s](\omega) := \int_{-\infty}^{\infty} s(t)\, \mathrm{e}^{-\mathrm{i}\omega t}\, \mathrm{d}t \tag{2.1}$$

and its inverse, here of a function $p(\omega)$, as

$$\mathcal{F}^{-1}[p](t) := \int_{-\infty}^{\infty} p(\omega)\, \mathrm{e}^{+\mathrm{i}\omega t}\, \frac{\mathrm{d}\omega}{2\pi}. \tag{2.2}$$

In spite of the lucidity of this $\mathcal{F}$-notation, we shall adopt the more careless physicist's notation and let $s(\omega)$ denote the Fourier transform of $s(t)$, i.e.,

$$s(\omega) := \mathcal{F}[s](\omega). \tag{2.3}$$

From the context and argument of the function in question, it should always be clear what is meant.

For quantum operators, the definitions are completely analogous. Note that, with our Fourier transform convention, it holds for a generic quantum operator $\hat{A}$, that $(\hat{A}(\omega))^\dagger \neq \hat{A}^\dagger(\omega)$, since

$$(\hat{A}(\omega))^\dagger = \left(\int_{-\infty}^{\infty} \hat{A}(t)\,\mathrm{e}^{-\mathrm{i}\omega t}\,\mathrm{d}t\right)^\dagger = \int_{-\infty}^{\infty} \hat{A}^\dagger(t)\,\mathrm{e}^{+\mathrm{i}\omega t}\,\mathrm{d}t = \hat{A}^\dagger(-\omega). \tag{2.4}$$

This is completely analogous to the classical case (Fourier transforms of functions), and just like a real function has a Fourier transform symmetric (even) upon complex conjugation, it holds that

$$\hat{A}^\dagger(t) = \hat{A}(t) \;\Rightarrow\; (\hat{A}(\omega))^\dagger = \hat{A}(-\omega). \tag{2.5}$$

Note also that our convention implies that

$$\hat{A}^\dagger(t) = \hat{A}(t) \;\Rightarrow\; \hat{A}^\dagger(\omega) = \hat{A}(\omega). \tag{2.6}$$

2.1.2 Power Spectral Densities

As mentioned above, the power spectral density (PSD) is the main object of our study. Here we give its basic definition, warn about a common pitfall, extend the definition to the quantum case, and finally explain how it may be experimentally estimated. For the sake of clarity and brevity, and since we are ultimately concerned with actual laboratory signals, we assume all non-quantum signals to be real.

There is no universal consensus on what is the *fundamental* definition of the PSD (cf. e.g. [Gardiner, 2009, chapter 1] and [Saulson, 1994, chapter 4]). Here we first define the finite-time Fourier transform, $s_T(\omega)$, of a signal $s(t)$ as

$$s_T(\omega) := \int_{-T/2}^{T/2} s(t)\,\mathrm{e}^{-\mathrm{i}\omega t}\,\mathrm{d}t. \tag{2.7}$$

Next, we define the PSD of s as

$$S_{ss}(\omega) := \lim_{T\to\infty} \frac{1}{T}|s_T(\omega)|^2. \tag{2.8}$$

If s has units of V, the units of S_{ss} is V^2/Hz. Note that the PSD exists even for signals that do not have a well-defined Fourier transform. Sometimes it is useful to consider the *energy* spectral density, $\tilde{S}$, of a signal. This may be defined as

$$\tilde{S}_{ss}(\omega) := \lim_{T\to\infty} |s_T(\omega)|^2 = |s(\omega)|^2. \tag{2.9}$$

The energy spectral density has units of V^2/Hz^2 and clearly only exists when the Fourier transform of s exists. The PSD may very well exist even if the energy spectral density does not, which reflects the fact that some signals[1] have infinite energy but finite power.

We mention the energy density here mainly to remedy some confusion about the subject. Not all authors are very strict in distinguishing the two densities, but they are different, and one should be careful to use the correct one. If all else fails, at least the units should be correct.

The PSD definition of equation (2.8) is straightforwardly extended to the case of two different signals, s and u, as

$$S_{su}(\omega) := \lim_{T\to\infty} \frac{1}{T} s_T(\omega) u_T(\omega). \tag{2.10}$$

S_{us} is referred to as the *cross* spectral density. To gain a better intuition for what S_{us} represents, it is useful to introduce the cross-correlation function between s and u, given by

$$s \star u(t) := \lim_{T\to\infty} \frac{1}{T} \int_{-T/2}^{T/2} s(t')u(t'+t)\mathrm{d}t'. \tag{2.11}$$

Note that $s \star s$ is denoted as the *auto*-correlation of s. The Wiener-Khinchin theorem now states that

$$S_{su}(\omega) = \mathcal{F}[s \star u](\omega), \tag{2.12}$$

which, in the special case of $u = s$, attests that the PSD is the Fourier transform of the auto-correlation function. It may be shown without too much effort (see [Riley et al., 2006, chapter 13] for the energy spectral density case) that equations (2.10) and (2.12) agree.

In the course of this work, we shall deal primarily with stochastic signals, whether the stochasticity arises from classical noise such as thermal fluctuations or from the more dignified quantum fluctuations. It will be an understood assumption throughout the remaining chapters that all stochastic signals are stationary,

[1] Stationary processes, in particular.

meaning that their statistical properties are constant in time, and ergodic, meaning that an *ensemble average* over a large number of realisations equals a long time *time average* of a single realisation. In such a case, we may also re-express the cross-correlation function as

$$s \star u(t) = \langle s(0)u(t) \rangle \,, \tag{2.13}$$

where $\langle \cdot \rangle$ should be understood as an ensemble average, and thus write

$$S_{su}(\omega) = \int_{-\infty}^{\infty} \langle s(0)u(t) \rangle \, \mathrm{e}^{-\mathrm{i}\omega t} \, \mathrm{d}t. \tag{2.14}$$

As ensemble averaging does not change the physical units of the quantity averaged (x and $\langle x \rangle$ have the same units), this definition has the same units as equation (2.8). The form of equation (2.14) is very suggestive as to what the quantum definition should be. For two operators, $\hat{A}$ and $\hat{B}$, we define their cross spectal density[2] as

$$S_{AB}(\omega) = \int_{-\infty}^{\infty} \left\langle \hat{A}^{\dagger}(0)\hat{B}(t) \right\rangle \mathrm{e}^{-\mathrm{i}\omega t} \, \mathrm{d}t = \int_{-\infty}^{\infty} \left\langle \hat{A}^{\dagger}(\omega')\hat{B}(\omega) \right\rangle \frac{\mathrm{d}\omega'}{2\pi} \,, \tag{2.15}$$

where $\langle \cdot \rangle$ now refers to the quantum mechanical expectation value. For the special but very relevant case of the PSD of a *Hermitian* operator, $\hat{X}$, we then have

$$S_{XX}(\omega) = \int_{-\infty}^{\infty} \left\langle \hat{X}(\omega')\hat{X}(\omega) \right\rangle \frac{\mathrm{d}\omega'}{2\pi} \,. \tag{2.16}$$

All quantum spectra of interest to us will belong to this group. We return to the subject of actually calculating these in section 2.3.3.

2.1.3 Measuring PSD's: The Periodogram

Finally, we address the issue of experimentally estimating the PSD. For stochastic processes, it holds that one can strictly speaking never *measure* what, say, the mean value of a signal is, but only acquire some data and *estimate* the mean value. There is in principle some freedom in the choice of estimator to use, although only one makes sense in the case of the mean[3]. For the PSD, the freedom is more outspoken, and here we take the *periodogram* as our estimator of choice. Before defining the periodogram, we need to briefly touch upon life's inescapable finiteness.

[2] The assumption of stationary statistics carries over to the quantum operators.
[3] To wit, the sum of all samples divided by the number of samples.

In the discussion above we used continuous time and frequency, but no actual data acquisition device offers this. Instead, one invariably deals with a finite number of samples acquired over a finite time. In such a case, the Fourier transform may be approximated by the discrete Fourier transform (DFT). For a set s_n of N samples of a signal s, sampled with a sampling rate F_S, the DFT is given by

$$\mathrm{DFT}[s](m) := \sum_{n=0}^{N-1} s_n \,\mathrm{e}^{-2\pi\mathrm{i}mn/N}, \tag{2.17}$$

where the m index runs from 0 to $N-1$ and maps to a real frequency as

$$m \mapsto m \times F_S/N. \tag{2.18}$$

The frequency increment F_S/N is also known as the resolution bandwidth (RBW). Spectral features more narrow than the RBW will not be resolved by the DFT. Note that the RBW is equal to the inverse of the acquisition time. The (finite continuous time) Fourier transform is approximated as

$$s_T(\omega) = \int_{-T/2}^{T/2} s(t)\,\mathrm{e}^{-i\omega t}\,\mathrm{d}t \approx \sum_{n=0}^{N} s_n \,\mathrm{e}^{-2\pi\mathrm{i}m/N}\,\Delta t = \mathrm{DFT}[s](m)\Delta t, \tag{2.19}$$

where we have introduced $\Delta t = 1/F_S$. It then follows, by comparison with equation 2.8, that the periodogram, P_s, defined as

$$P_s(m) = \frac{1}{T}\left|\mathrm{DFT}[s](m)\Delta t\right|^2 = \frac{1}{NF_S}\left|\mathrm{DFT}[s](m)\right|^2, \tag{2.20}$$

does indeed converge to the PSD as $T \to \infty$. Note that, since the input signal is real, half of the periodogram is redundant. Thus, one may only discern signals up to $F_S/2$, the so-called *Nyquist* frequency. As a final remark, we recognise that the periodogram is not a very efficient estimator. Without going into a serious discussion about spectral estimation[4], an intuitive understanding can be gained by comparing to the estimator for the mean. When estimating the mean, N data points go together to form a single number, whereas the periodogram estimates N different frequency bin values with N data points. The result is rather imprecise, which shows as noise in the measurement. This noise may be overcome by averaging together multiple periodograms, thereby using several data points per frequency bin estimate.

[4]Such a discussion may be found in [Broersen, 2006] and [Priestley, 1981] and is worthwhile the read.

We are now in a position to understand the basic data acquisition procedure of our experiment. All membrane mode frequencies of interest fall below $5\,\mathrm{MHz}$. We measure PSD's by sampling the output of our photodetector with a sample rate of $10\,\mathrm{MHz}$. To get a good frequency resolution, N is usually 10^6. The time trace thus acquired is then subjected to a fast Fourier transform, absolute squared and divided by NF_S. The procedure is repeated and outcomes are averaged together as required.

2.2 Mechanical Oscillators

The membrane resonators, although very thin, are of course three dimensional objects. The theory used to describe their interaction with light fields, to be developed in the next section, does however treat the coupling of two one-dimensional oscillators. To establish a connection to that treatment, we now discuss the mechanical properties of the membranes and in particular develop an effective one-dimensional one-mode description of their vibration.

2.2.1 Membranes: from three dimensions to one

The general problem of plate vibrations is very complicated, due to the many possible internal degrees of freedom of a plate. Luckily, not much of this freedom applies to the membranes we consider, and in fact a very simple two-dimensional wave equation captures the essential physics. Let us nonetheless begin in a slightly more general setting.

We consider the out-of-plane displacements, $w(x, y, t)$, of a thin rectangular plate ($d \ll L_x, Ly$). See Figure 2.1 for a sketch of the coordinate system.

For a plate of an isotropic material with uniform inplane tension, the unforced equation satisfied by the out-of-plane displacement $w(x, y, t)$, is a fourth-order partial differential equation [Leissa, 1969, chapter 10] [Landau and Lifshitz, 1986, chapter 2] of the form

$$\frac{D}{d}\nabla^4 w(x,y,t) - \mathcal{T}\nabla^2 w(x,y,t) + \rho\frac{\partial^2}{\partial t^2}w(x,y,t) = 0, \tag{2.21}$$

where ρ is the uniform material density (per unit volume), $\mathcal{T}$ is the tensile stress, d is the thickness of the membrane, and D is the flexural rigidity, which relates to the Young's modulus, E, and the Poisson ratio, ν, via

$$D = \frac{Ed^3}{12(1-\nu^2)}. \tag{2.22}$$

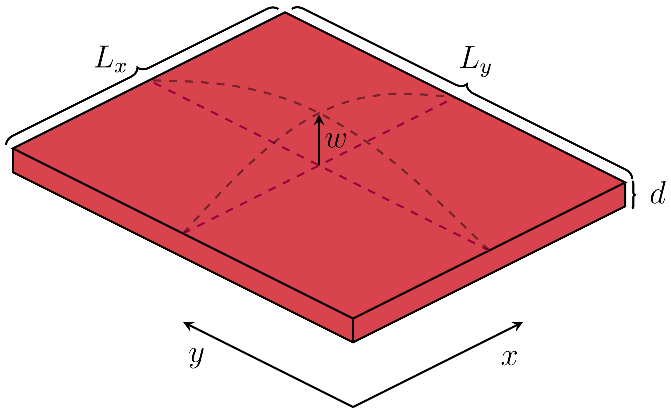

Figure 2.1: The coordinate system. Note that w and d as well as the ratio L_y/L_x are grossly exaggerated.

The first term of equation (2.21) represents the "energy cost" of bending [Landau and Lifshitz, 1986, chapter II], whereas the next two terms can be seen as the inplane force arising from the tension. For plates with negligible bending resistance, which can even be taken as the *definition* of a membrane (see [Rao, 2011, section 8.6]), the first term can be neglected. To get a feel for the orders of magnitudes involved, we can anticipate the (separable) solution of the wave equation, and take

$$w(x, y) \propto \sin(nk_x x)\sin(mk_y y), \tag{2.23}$$

with $k_{x,y} = \pi/L_{x,y}$. Let us for the time being consider a square membrane, i.e. $L_x = L_y = L$ and $k_x = k_y = k$. The number we are taking to be far less than one is then the following ratio, R_{nm}, given by

$$R_{nm} = \frac{Dnmk^2}{d\mathcal{T}}. \tag{2.24}$$

We note that R_{nm} is increasing in wavenumbers n and m, which is intuitively appealing as very short wavelengths "bend more" than long ones. Inserting typical values for our membranes found in Table 2.1 and checking along the fast growing diagonal ($n = m$), we find that R only approaches unity for $n = m = 570$ and is still less than $1\ \%$ for $n = m = 58$. In this work, we only ever consider mode numbers of $n < 15$ and $m < 15$, and we thus feel comfortable neglecting the bending resistance.

What then remains to be solved is the well-known two-dimensional wave equation:

$$\nabla^2 w(x, y, t) = -\frac{1}{c^2}\frac{\partial^2}{\partial t^2} w(x, y, t), \tag{2.25}$$

Quantity	Symbol	Value	Reference
Tensile stress	$\mathcal{T}$	$1.0\,\mathrm{GPa}$	[Tabata et al., 1989]
Poisson's ratio	ν	0.25	[Edwards et al., 2004]
Young's modulus	E	$350\,\mathrm{GPa}$	[Kaushik et al., 2005]
Density	ρ	$3.2\,\mathrm{g}\cdot\mathrm{cm}^{-3}$	[Pierson, 1999]
Membrane thickness	d	$50\,\mathrm{nm}$	Own measurement
Membrane sidelength	L	$500\,\mu\mathrm{m}$	Own measurement
Fundamental frequency	ω_{11}	$2\pi\times 791\,\mathrm{kHz}$	Equation (2.30)

Table 2.1: Typical membrane material parameters.

with the propagation speed c given by $c=\sqrt{\frac{\mathcal{T}}{\rho}}$, subject to the boundary conditions that

$$w(x,0,t)=w(x,L_y,t)=w(0,y,t)=w(L_x,y,t)=0 \tag{2.26}$$

and the initial condition that

$$\frac{\partial}{\partial t}w(x,y,0)=0, \tag{2.27}$$

where the former condition represents the actual clamping constraint of the membrane, and the latter an arbitrary phase choice.

By a standard separation of variables, we obtain the solution

$$w_{nm}(x,y,t) = z_{nm}(t)\sin(nk_x x)\sin(mk_y y), \tag{2.28}$$

$$z_{nm}(t) = z_0\cos(\omega_{nm}t), \tag{2.29}$$

where z_0 is a for now arbitrary amplitude constant[5], and the mode vibrational frequency satisfies that[6]

$$\omega_{nm}=c\sqrt{n^2k_x^2+m^2k_y^2}=\pi\sqrt{\frac{\mathcal{T}}{\rho}}\sqrt{\frac{n^2}{L_x^2}+\frac{m^2}{L_y^2}}. \tag{2.30}$$

For a square membrane, the following rewriting is often very helpful:

$$\omega_{nm}=\frac{\pi}{L}\sqrt{\frac{2\mathcal{T}}{\rho}}\sqrt{\frac{n^2+m^2}{2}}=\omega_{11}\sqrt{\frac{n^2+m^2}{2}}. \tag{2.31}$$

[5]The amplitude of the membrane oscillations will be determined once forces are allowed to act on the membrane. This happens in section 2.2.2.

[6]Here we anticipate that no relevant mode number will ever exceed 9, so that no ambiguity arises in the notation (e.g. ω_{132} will never occur).

Equation (2.28) is usually considered either for a fixed time or a fixed point in the plane. In the former case, each pair (n, m) gives rise to a characteristic mode shape of the vibration. The first four such modes are sketched in Figure 2.2 with z_0 set to unity. In the latter case, the membrane motion is a simple harmonic oscillator, the amplitude of which we shall now determine.

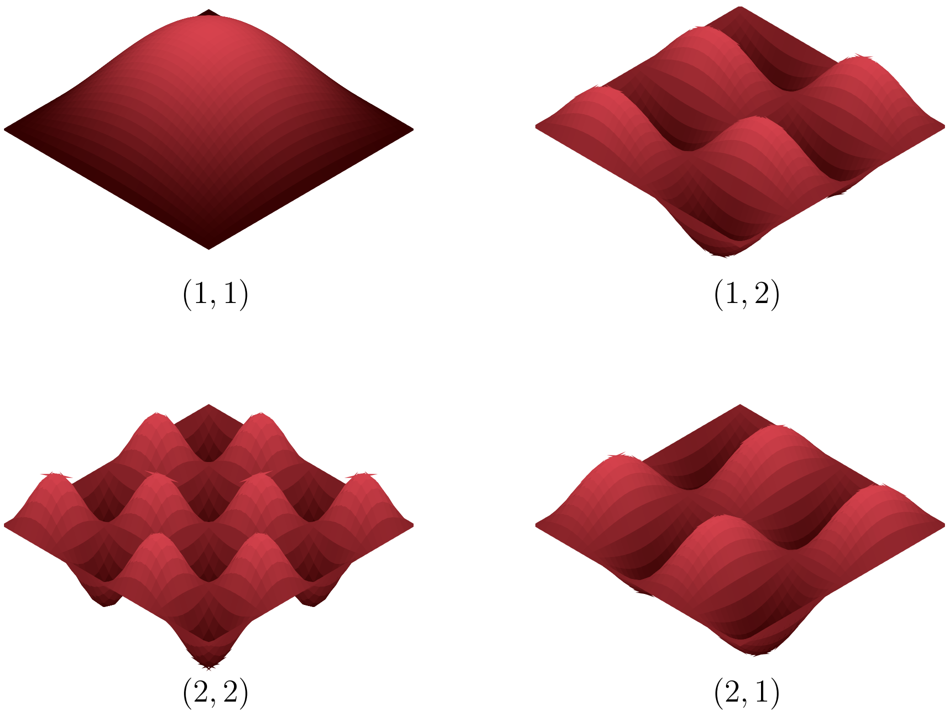

Figure 2.2: The first few excitations of a square membrane at time $t = 0$.

We are now ready to take the final step mapping the three-dimensional membrane vibrations onto a one-dimensional motion. We do so by requiring that the potential energy of each vibrational mode be equal to that of a one-dimensional oscillator with a new (possibly mode dependent) *effective mass*, m_{eff}. In formulae, we demand that

$$V_{\text{osc}} = \frac{1}{2} m_{\text{eff}} \omega_{nm}^2 z^2, \tag{2.32}$$

whilst physically, by integrating each small mass element,

$$\begin{aligned} V_{\text{osc}} &= \frac{1}{2} \int_0^{L_x} \int_0^{L_y} \mathrm{d}x \, \mathrm{d}y \, w^2(x, y, t) \rho d && \text{(2.33a)} \\ &= \frac{1}{2} z^2(t) \omega_{nm}^2 \times \frac{1}{4} \rho s L_x L_y. && \text{(2.33b)} \end{aligned}$$

As the last factor in equation (2.33b) is the physical mass, m_{phys}, of the membrane, we obtain the mode-independent relation

$$m_{\text{eff}} = \frac{1}{4} m_{\text{phys}}. \tag{2.34}$$

While this procedure is generally valid for any geometry, we note that it is peculiar to rectangular resonators that the effective mass is the same for all modes (see e.g. [Serra et al., 2015] for an experiment with circular membranes). As will become apparent in chapter 3, choosing the right mechanical mode to work with usually involves difficult trade-offs between equally important parameters, meaning that it is a virtue having at least one of these parameters being fixed.

2.2.2 Damped Harmonic Oscillators

Let us now consider a single mechanical mode at a fixed point, (x, y), on the membrane. This is the experimentally relevant situation, as one may imagine the tightly focused light beam to see only a very small region of the membrane. In section 3.6.1 we discuss the effects of finite beam widths. In this one-dimensional setting, we now allow forces to act on the membrane. In particular, we introduce a viscous damping force and a generic driving force, so that the equation of motion reads

$$\frac{\partial^2}{\partial t^2} z(t) - \Gamma_m \frac{\partial}{\partial t} z(t) + \omega_m^2 z(t) = \frac{1}{m_{\text{eff}}} F(t), \tag{2.35}$$

where we have allowed ourselves to drop the mode-indexing subscripts. We introduce the mechanical susceptibility, $\chi_m(\omega)$, via a Fourier transform to the frequency domain;

$$z(\omega) = \frac{m_{\text{eff}}^{-1}}{\omega_m^2 - \omega^2 + i\omega\Gamma_m} F(\omega) \tag{2.36a}$$

$$=: \chi_m(\omega) F(\omega). \tag{2.36b}$$

Equation (2.36) clarifies an important point about the membrane resonators, namely that they are indeed resonators rather than oscillators[7]; in the absence of a driving force[8] there is no motion whatsoever.

From equation (2.8), it then follows that the power spectral density of displacements is

$$S_{zz}(\omega) = S_{FF}(\omega) |\chi_m(\omega)|^2. \tag{2.37}$$

[7]Although neither the literature nor this work is always very strict in distinguishing the two.
[8]And with the initial conditions far back in the past.

It is sometimes useful to consider the time domain. From equation (2.36) it is seen that the solution to equation (2.35) is a convolution of F and the Fourier transform of χ_m. Indeed, assuming zero initial displacement and velocity [Uhlenbeck and Ornstein, 1930],

$$z(t) = \frac{1}{m_{\text{eff}}\omega_1} \int_0^t F(\tau)\,\mathrm{e}^{-\Gamma_m(t-\tau)/2} \sin(\omega_1 \tau)\,\mathrm{d}\tau, \tag{2.38}$$

where $\omega_1 = \sqrt{\omega_m^2 - \Gamma_m^2/4}$, which for any actual membrane used in this work is identical to ω_m, due to the smallness of the damping[9]. The ratio of mechanical frequency to damping is known as the *quality factor*, Q, of the resonator. For reasons that will be expanded upon in the next section, the quality factor is a key figure of merit for the usefulness of a given membrane.

The Q-value may be measured by applying a large initial displacement to the membrane. The full solution to (2.35) is given by

$$\begin{aligned} z(t) = {} & \frac{\Gamma_m z_0 + 2\dot{z}_0}{2\omega_1}\,\mathrm{e}^{-\Gamma_m t/2} \sin(\omega_1 t) + z_0\,\mathrm{e}^{-\Gamma_m t/2} \cos(\omega_1 t) \\ & + \frac{1}{m_{\text{eff}}\omega_1} \int_0^t F(\tau)\,\mathrm{e}^{-\Gamma_m(t-\tau)/2} \sin(\omega_1 \tau)\,\mathrm{d}\tau. \end{aligned} \tag{2.39}$$

For a fluctuating driving force such as a thermal driving force (to be introduced in the next section) the convolution term may be neglected for sufficiently large z_0 and short times, and we may write

$$z(t) = z_X(t)\cos(\omega_1 t) + z_Y(t)\sin(\omega_1 t), \tag{2.40}$$

with obvious definitions of z_X and z_Y. A lock-in measurement of $z(t)$ will then yield a response $z_R(t)$, given by

$$z_R(t) = \sqrt{z_X^2(t) + z_Y^2(t)} = \sqrt{\left(\frac{\Gamma_m z_0 + 2\dot{z}_0}{2\omega_1}\right)^2 + z_0^2}\,\mathrm{e}^{-\Gamma_m t/2}, \tag{2.41}$$

i.e. an exponentially decaying signal with a ring-down time $\tau_0 = 2/\Gamma_m$. In section 3.7.2 the measurements of Q are described.

2.2.3 Brownian Harmonic Oscillators

A very relevant driving force to consider is the stochastic thermal drive force of an equilibrium situation. Equation (2.35) then turns into a Langevin equation with

[9]As we shall see, ω_m/Γ_m is on the order of millions.

a stochastic driving force[10], F_{th}. Here we shall not worry about the mathematical subtleties of Langevin equations such as properly interpreting the derivative of a non-differentiable trajectory, but instead simply use the results to elucidate the relevant physics. The interested reader is referred to (in order of accessibility) [Gillespie, 1996], [van Kampen, 2007], and [Gardiner, 2009].

If the membrane has equilibrated to a reservoir at temperature T, then F_{th} must fulfil the fluctuation-dissipation theorem (see e.g. [Saulson, 1994, chapter 7]) and therefore have a power spectral density given by

$$S_{F_{\text{th}}F_{\text{th}}}(\omega) = 4k_B T\Gamma_m m_{\text{eff}}, \tag{2.42}$$

where k_B is Boltzmann's constant.

A comment about this spectrum is in order. At a glance, the thermal force seems to have infinite energy, as the power spectral density is not integrable. By virtue of the Wiener-Khinchin theorem, we may write the auto-correlation of the thermal force as

$$\langle F_{\text{th}}(t)F_{\text{th}}(t+\tau)\rangle = 2k_B T\Gamma_m \delta(\tau) m_{\text{eff}}. \tag{2.43}$$

It should now be clear that the "un-physicalness" of the power spectral density arises from the equally un-physical delta function correlation, the latter being however easier to understand. As long as the *actual* (non-zero) correlation time of the bath is much shorter than any other time scale involved, a zero-correlation time approximation may be made. Similarly in frequency space; the PSD actually falls off at some very high frequency, but this makes no difference to the physics of our interest and the flat response approximation is a good one.

Returning to the main track, equations (2.36), (2.37), and (2.42) yield the PSD of the mechanical displacements:

$$S_{zz}(\omega) = \frac{4\Gamma_m k_B T m_{\text{eff}}^{-1}}{(\omega_m^2 - \omega^2)^2 + \omega^2\Gamma_m^2}, \tag{2.44}$$

which, for Fourier frequencies close to the mechanical resonance, may be approximated as

$$S_{zz}(\omega) \approx \frac{\Gamma_m k_B T}{\omega_m^2 m_{\text{eff}}} \frac{1}{(\omega_m - \omega)^2 + (\Gamma_m/2)^2}, \tag{2.45}$$

i.e. a Lorentzian with a full-width at half maximum (FWHM) of Γ_m.

Now, from the equipartition theorem of statistical mechanics, every quadratic term in the system Hamiltonian, which in our case reads

$$H = \frac{1}{2} m_{\text{eff}}\omega_m^2 z^2 + \frac{1}{2} m_{\text{eff}}\dot{z}^2, \tag{2.46}$$

[10]Strictly speaking: a stationary and ergodic zero-mean time-uncorrelated Gaussian process.

will have a mean energy of $k_BT/2$. Therefore, in particular,

$$\left\langle z^2 \right\rangle = \frac{k_B T}{m_{\text{eff}}\omega_m^2}. \tag{2.47}$$

As the process driving the resonator is ergodic (by assumption), ensemble averaging and time averaging are equivalent. By virtue of Parseval's theorem, then,

$$\left\langle z^2 \right\rangle = \int_{-\infty}^{\infty} S_{zz}(\omega)\, \frac{\mathrm{d}\omega}{2\pi} = \frac{k_B T}{m_{\text{eff}}\omega_m^2}, \tag{2.48}$$

and the integral of the displacement PSD is thus proportional to the temperature of the resonator.

We now try to intuitively explain the damping term. In the presence of a thermal bath, the damping describes the rate at which phonons are exchanged with the environment. These exchanges happen in a random, phase non-coherent manner, sometimes exciting the mechanical motion, sometimes damping it. This leads to the following observation: the smaller the damping term, the longer the time of coherent oscillation once the resonator has been excited, and the slower the oscillation amplitude changes. For our experimental purposes, lower damping is thus always to be preferred.

This can be seen in Figure 2.3, where we have simulated three trajectories of the resonator by inserting a realisation of Gaussian white noise with standard deviation $\sqrt{2k_BT\Gamma_m m_{\text{eff}}/\mathrm{d}t}$ into equation (2.38). As the quality factor increases, the amplitude of the time traces modulates more slowly, and at the same time the peak in the frequency space becomes more well-defined around the mechanical frequency.

As a final subject of this section, it is interesting to now consider the case of equilibrium when coupling to two different thermal reservoirs. We may simply modify the governing Langevin equation to read

$$\ddot{z} + \Gamma_1\dot{z} + \Gamma_2\dot{z} + \omega_m^2 z = \frac{1}{m_{\text{eff}}}(F_1 + F_2). \tag{2.49}$$

Taking the forces F_1 and F_2 to be thermal and have PSDs each given by a fluctuation-dissipation theorem [Fogedby and Imparato, 2011], i.e. having

$$S_{F_1F_1} = 4k_BTm_{\text{eff}}\Gamma_1 T_1, \quad S_{F_2F_2} = 4k_BTm_{\text{eff}}\Gamma_2 T_2, \tag{2.50}$$

the corresponding PSD of the mechanical displacements then becomes

$$S_{zz}^{(\text{two baths})}(\omega) = \frac{k_B m_{\text{eff}}^{-1}(\Gamma_1 T_1 + \Gamma_2 T_2)}{(\omega_m^2 - \omega^2)^2 + \omega^2(\Gamma_1 + \Gamma_2)^2}. \tag{2.51}$$

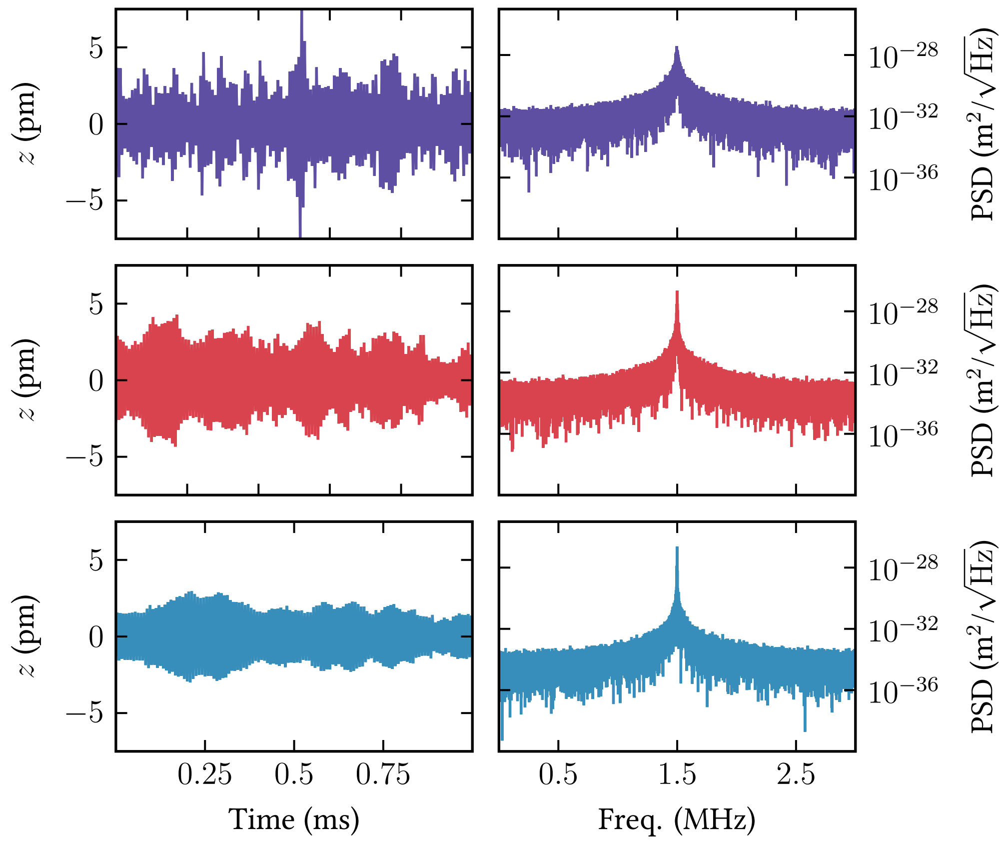

Figure 2.3: Simulated trajectories and corresponding periodograms of the Brownian oscillator for three different Q-values: 10^2 (purple), 10^3 (red), and 10^4 (blue). Other parameters: $\omega_m = 2\pi \times 1.5\,\text{MHz}$, $T = 300\,\text{K}$, $m_{\text{eff}} = 200\,\text{ng}$.

We may now use the relation between the PSD, the mean square displacement and the equipartition theorem (equations (2.47) and (2.48)) to calculate an *effective temperature* of the resonator;

$$T_{\text{eff}} = \left(\frac{k_B}{m_{\text{eff}}\omega_m^2}\right)^{-1} \int_{-\infty}^{\infty} S_{zz}^{\text{(two baths)}}(\omega)\, \mathrm{d}\omega = \frac{\Gamma_1 T_1 + \Gamma_2 T_2}{\Gamma_1 + \Gamma_2}. \tag{2.52}$$

In this classical picture, one can thus, irrespective of the first reservoirs temperature, always cool (or heat) the resonator arbitrarily close to the second reservoir's temperature, simply by increasing the coupling strength to said reservoir. Although non-classical effects, in particular *radiation-pressure quantum back-action*, will, as we shall see in the next section, impose a lower limit to the achievable cooling, it is nonetheless instructive to consider a semi-classical laser cooling theory[11]

[11]One could argue that the description is entirely classical. The use of bosons urge us to call it

to see how large a cooling rate ratio (i.e. Γ_2/Γ_1) one needs to reach the ground state of the resonator.

For any bosonic mode, such as the phonons of a mechanical membrane mode or the photons of a cavity field, the thermal occupancy is given by the Bose-Einstein distribution[12]:

$$\bar{n}_{\text{th}} = \frac{1}{e^{\hbar\omega_{\text{mode}}/k_B T} - 1}. \tag{2.53}$$

For a light field at 300 THz, the room temperature occupation is on the order of 10^{-21}. For a resonator coupled to such a field, its bath temperature can thus *classically* be taken to be zero. For a membrane mode coupled to a cavity mode, we therefore find, in agreement with [Aspelmeyer et al., 2014], a final temperature of

$$T_{\text{final}} = T_{\text{init}} \frac{\Gamma_m}{\Gamma_m + \Gamma_{\text{opt}}}, \tag{2.54}$$

where we have anticipated the notation of the next section.

The prediction for final occupancy by a laser cooled membrane mode is shown in Figure 2.4.

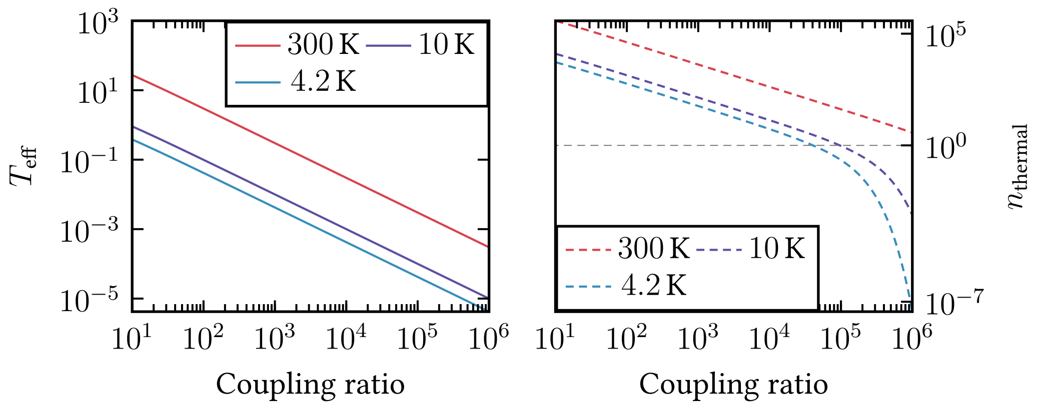

Figure 2.4: Semi-classical laser cooling prediction for a membrane mode of frequency $\omega_m = 2\pi \times 1.5$ MHz for different ambient temperatures T_{init}.

A coupling rate ratio of more than 5×10^4 seems necessary to reach the ground state. This already consolidates the urgent importance of high mechanical quality factors as well as the need for a cryogenic environment.

We conclude this section by recasting the equilibrium in terms of *jumping rates* to obtain the correct formula for the phonon occupancy. We may view a harmonic

semi-classical, but the main thing to keep in mind is the complete absence of quantum fluctuations.

[12]Here we take the chemical potential to be zero.

oscillator as an infinite chain of energy states and consider the system dynamics as jump between these (see Figure 2.5).

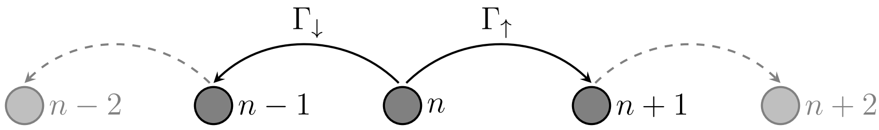

Figure 2.5: Jump rates in a harmonic oscillator.

The jump rates may in general be complicated expressions, encompassing information about the many possible baths perturbing the resonator. Here we only assume that they are constant in time. In this setting, the dynamics of the system are readily described by a *master equation* [van Kampen, 2007, chapter V] for the evolution of the probability p_n of the system to be in state n;

$$\frac{\mathrm{d}}{\mathrm{d}t}p_n = n\Gamma_\uparrow p_{n-1} + (n+1)\Gamma_\downarrow p_{n+1} - n\Gamma_\downarrow p_n - (n+1)\Gamma_\uparrow p_n. \tag{2.55}$$

To find the average phonon number, we may multiply through by n and perform a sum over n, using that the average phonon number is given by

$$\bar{n} = \sum_{n=0}^{\infty} n p_n. \tag{2.56}$$

Doing this (and shifting the sums a little), one finds for the steady state, where $\frac{\mathrm{d}}{\mathrm{d}t}p_n = 0$, that

$$\bar{n} = \frac{\Gamma_\uparrow}{\Gamma_\downarrow - \Gamma_\uparrow}. \tag{2.57}$$

An alternative way at arrive to the same result is by the principle of *detailed balance* [Clerk et al., 2010]. In equilibrium, we demand that

$$\frac{\Gamma_\uparrow}{\Gamma_\downarrow} = \mathrm{e}^{\frac{-\hbar\omega_{\text{mode}}}{k_B T_{\text{eff}}}}. \tag{2.58}$$

From this principle and the fact that we are dealing with bosons (see equation (2.53)), it follows that the mean equilibrium phonon number is given by

$$\bar{n} = \frac{1}{\mathrm{e}^{\hbar\omega_{\text{mode}}/k_B T_{\text{eff}}} - 1} = \frac{\Gamma_\uparrow}{\Gamma_\downarrow - \Gamma_\uparrow}. \tag{2.59}$$

In the simple case of coupling only to a single heat bath, it is not hard to verify that the jump rates $\Gamma_\uparrow^{\text{th}} = \bar{n}_{\text{th}}\Gamma_m$ and $\Gamma_\downarrow^{\text{th}} = (\bar{n}_{\text{th}} + 1)\Gamma_m$ yield the correct mean occupation.

This last equation, which may of course be recast to provide an effective temperature, turns out to be the proper replacement for the (semi-) classical result of equation (2.52). In section 2.3.4.2 we calculate the jump rates using the full quantum machinery.

2.3 Optomechanical Dynamics

In this section we introduce the full quantum mechanical model needed to describe the dynamics of our system. Our approach consists of three steps. First, write up a Hamiltonian appropriate for the particular limit in question. Next, work out the Heisenberg-Langevin equations of motion to get the system dynamics. Finally, apply the input-output relations to calculate what will actually be measured outside of the cavity. What we present here is the so-called *canonical* quantum optomechanical system, in which one cavity field mode is coupled parametrically to one mechanical mode, modelled by canonical quantisation of a cavity with one mirror on a spring. This simple model maps surprisingly well onto a wide range of different systems (see [Aspelmeyer et al., 2014] for a review) with more complex geometries, including our own system. We discuss that particular mapping in section 2.4. For the remainder of this section, since the model is explicitly one-dimensional, and to keep consistency with the notation used in the majority of the literature, we let x rather than z denote the mechanical degree of freedom.

In Figure 2.6 we show an overview of the canonical quantum cavity optomechanical system, where a light field ($\hat{a}$, $\hat{a}^\dagger$) couples to a mechanical resonator with the coupling rate g, while both photons and phonons dissipate out of the cavity and a laser drive s_{in} feeds the cavity.

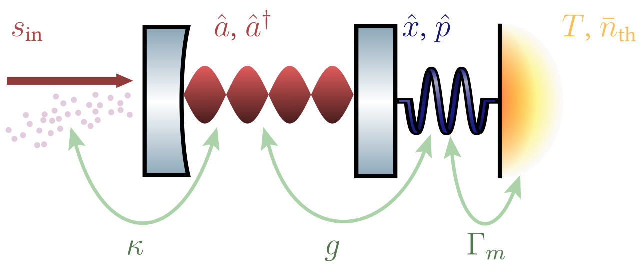

Figure 2.6: A sketch of the canonical optomechanical system. The purple dots to the far left indicate vacuum noise of the light field.

2.3.1 The Ground State

Before embarking on the description of the light-mechanical interaction dynamics, we briefly discuss the quantum mechanical aspects of the mechanical resonator and in particular clarify what is strictly speaking meant by ground state cooling.

The Hamiltonian for the mechanics alone reads

$$\hat{H}_{\text{mech}} = \frac{\hat{p}^2}{2m_{\text{eff}}} + \frac{m_{\text{eff}}\omega_m^2}{2}\hat{x}^2 = \hbar\omega_m\left(\hat{b}^\dagger\hat{b} + \frac{1}{2}\right), \tag{2.60}$$

where we have introduced the phononic creation/annihilation operators $\hat{b}^\dagger$ and $\hat{b}$. The last $1/2$-term implies a finite displacement amplitude even when no quanta of motion are in the resonator. To see this, one may take the expectation value of both sides of (the last equality sign of) equation (2.60). Setting the phonon number equal to zero and assuming equipartition of energy between the kinetic and potential energy,

$$\langle T_{\text{mech}}\rangle + \langle V_{\text{mech}}\rangle = \frac{\hbar\omega_m}{2}, \quad \langle V_{\text{mech}}\rangle = \frac{\hbar\omega_m}{4}, \tag{2.61}$$

whence it follows that

$$\sqrt{\langle\hat{x}^2\rangle} = \sqrt{\frac{\hbar}{2m_{\text{eff}}\omega_m}}. \tag{2.62}$$

The root mean square of the ground state displacement is denoted as the *zero-point fluctuation amplitude*, x_{ZPF}. Completely analogously, one may derive zero-point fluctuations for the momentum by looking at the kinetic rather than the potential energy. One then arrives at

$$p_{\text{ZPF}} = \sqrt{\langle\hat{p}^2\rangle} = \sqrt{\frac{\hbar m_{\text{eff}}\omega_m}{2}}. \tag{2.63}$$

The state used to calculate the expectation values above was the *true* ground state, the Fock state $|0\rangle$. In reality, the mechanical resonator will never be quite in that state, but always in a *thermal* state, an incoherent mixture of different Fock states. For a thermal state, the corresponding density operator can be expressed in terms of Fock states as

$$\hat{p}_{\text{th}} = \sum_{n=0}^{\infty} P_n\,|n\rangle\,\langle n|\,, \tag{2.64}$$

where the P_n, the probabilities of finding n phonons in the state, can be cast as

$$P_n = \frac{\bar{n}^n}{(1+\bar{n})^{n+1}}, \tag{2.65}$$

with $\bar{n}$ being the mean phonon occupancy. Considering $n = 0$, it is seen that when $\bar{n} = 1$, the probability P_0 is exactly one half. Whenever $\bar{n} < 1$, the resonator spends *most of its time* in the state $|0\rangle$. It then makes sense to define the following as ground state cooling: achieving a thermal state with a mean phonon occupancy strictly less than unity. This is the definition commonly accepted when discussing optomechanical ground state cooling and also the definition that we shall adopt.

To really reach the true ground state, one would have to perform a strong projective measurement of $\hat{n}$, an experimental tasks much beyond the scope of this work.

2.3.2 The Optomechanical Hamiltonian

The appropriate Hamiltonian for an optomechanical system must include the two harmonic oscillators, their interaction and the laser drive "feeding" new photons to the system. Therefore,

$$\hat{H} = \hat{H}_{\text{opt}} + \hat{H}_{\text{mech}} + \hat{H}_{\text{int}} + \hat{H}_{\text{drive}}, \tag{2.66}$$

with

$$\hat{H}_{\text{opt}} = \hbar\omega_c \left(\hat{a}^\dagger \hat{a} + \frac{1}{2} \right), \tag{2.67}$$

$$\hat{H}_{\text{mech}} = \frac{\hat{p}^2}{2m_{\text{eff}}} + \frac{m_{\text{eff}}\omega_m^2}{2}\hat{x}^2 = \hbar\omega_m \left(\hat{b}^\dagger \hat{b} + \frac{1}{2} \right), \tag{2.68}$$

$$\hat{H}_{\text{int}} = \hbar G \hat{x} \hat{a}^\dagger \hat{a}, \tag{2.69}$$

$$\hat{H}_{\text{drive}} = \mathrm{i}\hbar\sqrt{\kappa_R} \left(\bar{s}_{\text{in}} \hat{a}^\dagger \,\mathrm{e}^{-\mathrm{i}\omega_L t} - \bar{s}_{\text{in}}^* \hat{a} \,\mathrm{e}^{\mathrm{i}\omega_L t} \right) \tag{2.70}$$

That no further optical modes are involved is reasonable in the limit where the free spectral range of the cavity is much larger than the optical linewidth, i.e. when the cavity finesse is large. As our system operates with $\mathcal{F} \approx 10^3 - 10^5$, this approximation is completely justified. Also, scattering of photons from the mechanical resonator into other cavity modes must be suppressed, which is the case if the mechanical frequency is much smaller than the cavity FSR [Law, 1995]. Here we are in even better shape, as FSR ≈ 1 THz, whereas $\omega_m \approx 1$ MHz. Finally, by the same logic, it holds for the mechanical modes that their inter-modal spacing must be much larger than their linewidths for us to neglect all but one of them. As we shall see in chapter 4, this is actually not always the situation. It does, however, serve as the appropriate starting point of our analysis.

We now turn to the interaction. First, we find that the radiation pressure force has the expected form (cf. equation (1.15)),

$$\hat{F}_{\mathrm{RP}} = -\frac{\partial \hat{H}_{\mathrm{int}}}{\partial \hat{x}} = -\hbar G \hat{a}^\dagger \hat{a}, \tag{2.71}$$

that is, the force is proportional to the photon number. Next, it is seen that a frequency shift is induced as the coupling parameter G is varied away from zero, as

$$\hbar\omega_{\mathrm{c}}\hat{a}^\dagger\hat{a} \to \hbar(\omega_{\mathrm{c}} + G\hat{x})\hat{a}^\dagger\hat{a} = \hbar\omega_{\mathrm{cav}}\hat{a}^\dagger\hat{a}. \tag{2.72}$$

The optomechanical coupling parameter describes how much the cavity resonance shifts per unit mechanical displacement;

$$G = \frac{\partial \omega_{\mathrm{cav}}}{\partial \hat{x}}. \tag{2.73}$$

The coupling is in general dependent of the system geometry (we explore our own membrane-in-the-middle geometry in section 2.4), but has the value ω_c/L for the canonical geometry. This "raw" coupling rate is easily on the order of hundreds of $\mathrm{PHz}\cdot\mathrm{m}^{-1}$, which has little relation to any number achieved in our experiment. It is natural to scale the raw coupling rate down by the relevant unit of motion of the membrane, namely the zero-point fluctuations, to obtain the so-called *vacuum* optomechanical coupling rate g_0,

$$g_0 = x_{\mathrm{ZPF}} G, \tag{2.74}$$

which in our experiment is on the order of a few hundred Hz. Finally, as more light entails more interaction, it makes sense to define a *cavity enhanced* coupling rate, g, as

$$g = \sqrt{\bar{n}_{\mathrm{cav}}}\, g_0, \tag{2.75}$$

where $\bar{n}_{\mathrm{cav}}$ is the steady-state photon occupation of the cavity.

Viewing the optomechanical system dynamics as a fight between coherent interaction and incoherent losses, we may define a figure of merit quantifying which side is "winning". This is the so-called *cooperativity*, C, which is the ratio between "good" coupling rates and "evil" loss rates;

$$C = \frac{4g^2}{\kappa\Gamma_m}. \tag{2.76}$$

One may intuitively understand the cooperativity by envisioning a photon's round trip in the cavity. The photon may interact with a phonon and thereby become correlated with it, which happens at a rate g, or it may be lost out of the cavity. Similarly, the phonon that interacted may also escape out of the mechanical resonator, thus losing the correlations. If both light and mechanics are only replenished with vacuum, the cooperativity as it stands is good figure of merit. In the presence of a very warm thermal bath, one should weight the mechanical loss rate by the thermal bath occupancy, and a better figure of merit is the *quantum cooperativity*, C_q, given by

$$C_q = \frac{C}{\bar{n}_{\text{th}}} = \frac{4g^2}{\kappa\Gamma_m\bar{n}_{\text{th}}}. \tag{2.77}$$

As we shall see in section 2.3.4.2, having $C_q > 1$ is indeed a necessary condition for ground-state cooling.

Although we are in principle finished with the Hamiltonian by now, there are two re-writings that greatly improve the usability of the Hamiltonian for the equations of motion. First, as all our measurements will be relative to the laser frequency rather than to an absolute frequency reference, it makes sense to transform to a frame rotating with the laser frequency, where the discrepancy between laser and cavity frequency is given by the detuning, $\Delta = \omega_L - \omega_c$. We do so by letting [Bowen and Milburn, 2016, chapter 1]

$$\hat{H} \rightarrow \hat{U}^\dagger \hat{H} \hat{U} - \hat{T}, \quad \text{where} \quad \hat{T} = \hbar\omega_L \hat{a}^\dagger\hat{a},\ \hat{U} = \mathrm{e}^{-\mathrm{i}\hat{T}t/\hbar}. \tag{2.78}$$

The full form of the interaction given in equation (2.69) is, however seemingly simple, sometimes too unwieldy. By setting $\hat{a} = \bar{\alpha} + \delta\hat{a}$ (and, without loss of generality, $\arg(\bar{\alpha}) = 0$) we may expand and approximate the interaction as

$$\begin{aligned} \hat{H}_{\text{int}} &= \hbar G\hat{x}(\bar{\alpha} + \delta\hat{a}^\dagger)(\bar{\alpha} + \delta\hat{a}) && (2.79)\\ &\approx \hbar G|\alpha|^2\hat{x} + \hbar G(\bar{\alpha}\delta\hat{a} + \bar{\alpha}\delta\hat{a}^\dagger)\hat{x}. && (2.80) \end{aligned}$$

The first term corresponds to a constant shift of the mechanics, which we may absorb back[13] into the mechanical displacement and detuning by letting $\hat{x} \rightarrow \hat{x} - \hbar G|\alpha|^2/m_{\text{eff}}\omega_m^2$ and $\Delta \rightarrow \Delta - \hbar G^2|\alpha|^2/m_{\text{eff}}\omega_m^2$. This approximation yields the so-called *linearised* interaction[14], with which, in the rotating frame, the Hamiltonian now reads

$$\begin{aligned} \hat{H}_{\text{lin}} = &- \hbar\Delta\hat{a}^\dagger\hat{a} + \hbar\omega_m\hat{b}^\dagger\hat{b} + \hbar g(\hat{a}^\dagger + \hat{a})(\hat{b}^\dagger + \hat{b}) \\ &+ \mathrm{i}\hbar\sqrt{\eta_c\kappa}(\bar{s}_{\text{in}}\hat{a}^\dagger - \bar{s}_{\text{in}}^*\hat{a}), \end{aligned} \tag{2.81}$$

where we have also disregarded the factors of $\hbar\Delta/2$ and $\hbar\omega_m/2$, as they have no effect on the dynamics of the system, and redefined the light operators to encompass the shift by their mean value, i.e. we let $\hat{a} \rightarrow \hat{a} + \bar{\alpha}$.

[13] We do not introduce new notation for these shifted quantities, but hope that it is always clear from the context whether the shifted or unshifted quantity is in play.

[14] Since, as we shall see, the equations of motion become linear in $\hat{a}$ and $\hat{b}$.

2.3.3 Heisenberg-Langevin Equations

Once the system Hamiltonian has been determined, the next step is to insert it into the general form of the Heisenberg-Langevin equations to obtain the equations of motions for the operators of interest. We now briefly outline how the relevant equations of motion come about. Detailed accounts may be found in [Gardiner, 1991, chapter 3] and [Bowen and Milburn, 2016, chapter 1].

What we are seeking is the quantum analogue of the classical Langevin equation for an oscillator[15], an example of which is equation (2.35) when the driving force F is stochastic. By making the assumption that the heat bath consists of an ensemble of independent bosonic oscillator modes coupling only to $\hat{x}$ of our particle under consideration, and, furthermore, that said coupling, γ, is frequency independent[16], one then arrives at the following Heisenberg-Langevin equation for a general operator $\hat{A}$:

$$\frac{\mathrm{d}}{\mathrm{d}t}\hat{A} = \frac{1}{i\hbar}[\hat{A}, \hat{H}] - \frac{1}{i\hbar}[\hat{A}, \hat{x}]\hat{F} + \frac{m}{2i\hbar}\left\{[\hat{A}, \hat{x}], \gamma\hat{x}\right\}. \tag{2.82}$$

With the replacements of m_{eff} for m and Γ_m for γ and the proper choice of $\hat{F}$ (see below), this will be the governing equation for the mechanics. It is seen that equation (2.82) has the form of the normal Heisenberg equation plus additional terms describing the bath coupling. Furthermore, the coupling to the bath only influences the equation of motion for $\hat{p}$, as taking $\hat{A} = \hat{x}$ obviously makes the last two terms on the right hand side vanish. The appropriate thermal force operator, $\hat{F}_{\text{th}}$, for the mechanics fulfils that[17]

$$\begin{aligned}\left\langle \hat{F}_{\text{th}}(t)\hat{F}_{\text{th}}(t+\tau) + \hat{F}_{\text{th}}(t+\tau)\hat{F}_{\text{th}}(t)\right\rangle = 2m_{\text{eff}}\Gamma_m k_B T& \\ \times \frac{\mathrm{d}}{\mathrm{d}\tau}\left(\coth\left[\frac{\pi k_B T}{\hbar}\tau\right]\right).&\end{aligned} \tag{2.83}$$

Curiously, this is not a memoryless process, in spite of the frequency-independent coupling assumption. It is, however, a very sharply peaked function, and may be approximated by a δ-function. That approximation will hold as long as the

[15]Note that non-harmonic potentials also are included in this treatment. We shall, however, never consider them.

[16]The assumption of frequency-indepedence is called the *first Markov approximation*, since it leads to damping terms only depending on the current time, thus being memoryless [Gardiner and Collett, 1985]. See however equation 2.83 and the comment below.

[17]On this point, we follow [Bowen and Milburn, 2016]. See also [Giovannetti and Vitali, 2001] for a discussion of the appropriate form of the thermal noise operator.

characterstic bath time scale, $\hbar/k_B T$, is much shorter than the mechanical decay time (or, as we shall call it in section 3.7.2, ring-down time), $1/\Gamma_m$. At 1 K, for a 2 MHz mechanical mode with a quality factor of 10 M, $\hbar/k_B T \approx 8$ ps whereas $1/\Gamma_m \approx 0.8$ s. We therefore introduce no big error when making the Markovian approximation for the bath and setting

$$\left\langle \hat{F}_{\text{th}}(t)\hat{F}_{\text{th}}(t+\tau) + \hat{F}_{\text{th}}(t+\tau)\hat{F}_{\text{th}}(t) \right\rangle = 4m_{\text{eff}}\Gamma_m k_B T\delta(\tau). \tag{2.84}$$

For the light operators, it is first of all customary to work with the creation and annihilation operators rather than the dimensionful quadrature operators, and secondly to make the rotating wave approximation for the bath interaction. When doing so, the following Heisenberg-Langevin equation for a general operator $\hat{A}$ emerges:

$$\frac{\mathrm{d}}{\mathrm{d}t}\hat{A} = \frac{1}{i\hbar}[\hat{A},\hat{H}] - [\hat{A},\hat{a}^\dagger]\left(\frac{\gamma}{2}\hat{a} - \sqrt{\gamma}\hat{a}_{\text{in}}\right) + \left(\frac{\gamma}{2}\hat{a}^\dagger - \sqrt{\gamma}\hat{a}^\dagger_{\text{in}}\right)[\hat{A},\hat{a}]. \tag{2.85}$$

In equation 2.85, the bath noise, expressed through the input operators $\hat{a}_{\text{in}}$ and $\hat{a}^\dagger_{\text{in}}$, enters symmetrically in both quadratures. By letting $\gamma \to \kappa$ we obtain the appropriate Heisenberg-Langevin equation for the light modes. The input noise operators have the following correlation functions:

$$\left\langle \hat{a}_{\text{in}}(t)\hat{a}^\dagger_{\text{in}}(t') \right\rangle = \delta(t-t'), \tag{2.86}$$

$$\left\langle \hat{a}^\dagger_{\text{in}}(t)\hat{a}_{\text{in}}(t') \right\rangle = \left\langle \hat{a}^\dagger_{\text{in}}(t)\hat{a}^\dagger_{\text{in}}(t') \right\rangle = \langle \hat{a}_{\text{in}}(t)\hat{a}_{\text{in}}(t')\rangle = 0 \tag{2.87}$$

Applying the transformation to the rotating frame (equation (2.78)) to the full Hamiltonian of equation (2.66) and using the resulting Hamiltonian to generate Heisenberg-Langevin equations for light and mechanics, we obtain the following set of equations of motion:

$$\frac{\mathrm{d}}{\mathrm{d}t}\hat{a} = \left(\mathrm{i}\Delta - \frac{\kappa}{2} - \mathrm{i}G\hat{x}\right)\hat{a} + \sqrt{\kappa_R}\bar{s}_{\text{in}} + \sqrt{\kappa}\hat{a}_{\text{in}} \tag{2.88}$$

$$\frac{\mathrm{d}}{\mathrm{d}t}\hat{a}^\dagger = \left(-\mathrm{i}\Delta - \frac{\kappa}{2} + \mathrm{i}G\hat{x}\right)\hat{a}^\dagger + \sqrt{\kappa_R}\bar{s}^*_{\text{in}} + \sqrt{\kappa}\hat{a}^\dagger_{\text{in}} \tag{2.89}$$

$$\frac{\mathrm{d}}{\mathrm{d}t}\hat{x} = \frac{1}{m_{\text{eff}}}\hat{p} \tag{2.90}$$

$$\frac{\mathrm{d}}{\mathrm{d}t}\hat{p} = -m_{\text{eff}}\omega_m^2\hat{x} - \hbar G\hat{a}^\dagger\hat{a} - \Gamma_m\hat{p} + \hat{F}_{\text{th}}. \tag{2.91}$$

These are the governing equations in their most general form. From these equations, one may derive a myriad of interesting optomechanical effects, usually in different limits where different terms may be neglected. In the next four sections we explore three important phenomena arising from the dynamical light-mechanical interaction in greater detail. In section 2.3.3.1 we consider an even simpler example, namely a *static*, classical phenomenon, the static bistability. Before doing so, let us demonstrate the versatility of equations (2.82) and (2.85) by deriving the linearised equations of motion. This is simply done by inserting the linearised Hamiltonian of equation (2.81) into the aforementioned equations, whereby we obtain that

$$\frac{\mathrm{d}}{\mathrm{d}t}\hat{a} = \left(\mathrm{i}\Delta - \frac{\kappa}{2}\right)\hat{a} - \mathrm{i}G|\alpha|\hat{x} + \sqrt{\kappa_R}\bar{s}_{\mathrm{in}} + \sqrt{\kappa}\hat{a}_{\mathrm{in}} \tag{2.92}$$

$$\frac{\mathrm{d}}{\mathrm{d}t}\hat{a}^\dagger = \left(-\mathrm{i}\Delta - \frac{\kappa}{2}\right)\hat{a}^\dagger + \mathrm{i}G|\alpha|\hat{x} + \sqrt{\kappa_R}\bar{s}^*_{\mathrm{in}} + \sqrt{\kappa}\hat{a}^\dagger_{\mathrm{in}} \tag{2.93}$$

$$\frac{\mathrm{d}}{\mathrm{d}t}\hat{x} = \frac{1}{m_{\mathrm{eff}}}\hat{p} \tag{2.94}$$

$$\frac{\mathrm{d}}{\mathrm{d}t}\hat{p} = -m_{\mathrm{eff}}\omega_m^2\hat{x} - \hbar G|\alpha|(\hat{a}^\dagger + \hat{a}) - \Gamma_m\hat{p} + \hat{F}_{\mathrm{th}}. \tag{2.95}$$

These linearised equations of motion will serve as the starting point for most of our subsequent analysis, and in particular in section 2.3.5 we exploit their linearity to recast them in matrix form.

2.3.3.1 Static bistability

In the steady-state classical limit (with a constant drive), equations (2.88) and (2.91) take on the simple forms:

$$|\alpha| = \frac{\sqrt{\kappa_R}\ \bar{s}_{\mathrm{in}}}{\mathrm{i}\Delta - \kappa/2 - \mathrm{i}G\bar{x}}, \tag{2.96}$$

$$\bar{x} = -\frac{\hbar G}{m_{\mathrm{eff}}\omega_m^2}|\alpha|^2. \tag{2.97}$$

Evidently, for a given intracavity field amplitude $|\alpha|$, the corresponding mechanical displacement $\bar{x}$ is the root of a third-order polynomial. The condition for more than one real root to exist can be understood from Figure 2.7, where equations (2.96) and (2.97) are plotted; when the slope of the Lorentzian cavity response to the displacement exceeds that of the linear displacement caused by the static radiation pressure (purple line), more than one solution can exist. Note that the cavity response peak occurs when $\Delta = G\bar{x}$, which experimentally means that the regime of multiple stable points is entered as the detuning is scanned closer to the cavity resonance. In Figure 2.7, this corresponds to the dashed curve moving towards the solid curve as the detuning is decreased.

In practice, this bistability imposes an upper limit to the amount of intracavity power achievable in the experiment. For a given input power, there is (if the power is large enough) a critical detuning for which the system becomes unstable. We return to this point in chapter 3.

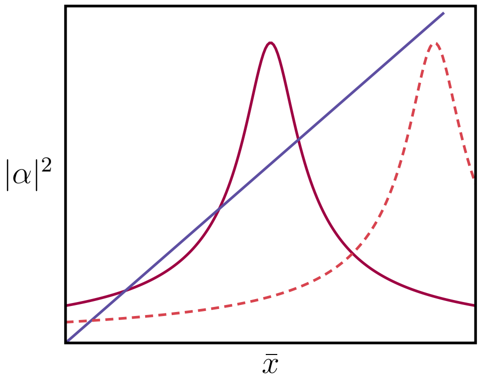

Figure 2.7: Static bistability illustrated. The dashed red line is made with the same parameters as the solid burgundy line, except for the detuning, which 1.8 times higher for the dashed line.

2.3.4 Optomechanical Sideband Cooling

Of considerable experimental interest is the possibility of using the laser field as an effectively zero-temperature bath to which we couple the mechanical resonator. A brief discussion of this was already given in section 2.2.3. Now we derive the coupling rate of the mechanics to said cold bath, Γ_{opt}, as we analyse the dynamical effects of the interaction. We do so first in a classical picture, capturing most of the relevant physics and then proceed to examine the quantum effects induced by fluctuations of the light field, specifically the minimal achievable phonon number even at zero ambient temperature.

2.3.4.1 Classical picture

From the linearised equations of motion, equations (2.92)- (2.95), we may recover the classical limit by replacing operators with classical variables and neglecting the noise terms (or more properly: replace them by their zero expectation values). We also assume a constant input drive, and thus neglect the s_{in} term. We then have that

$$\dot{a} = (\mathrm{i}\Delta - \kappa/2)a - \mathrm{i}G|\alpha|x, \tag{2.98}$$

$$m_{\text{eff}}\ddot{x} = -m_{\text{eff}}\omega_m^2\,\mathrm{d}x - m_{\text{eff}}\Gamma_m\delta\dot{x} - \hbar G|\alpha|(a + a^*). \tag{2.99}$$

Solving these equations in the frequency domain reveals mechanically induced sidebands to the light field[18];

$$a(\omega) = \frac{-\mathrm{i}G|\alpha|}{-\mathrm{i}(\Delta+\omega)+\kappa/2}x(\omega), \tag{2.100}$$

$$a^*(\omega) = \frac{\mathrm{i}G|\alpha|}{\mathrm{i}(\Delta-\omega)+\kappa/2}x(\omega), \tag{2.101}$$

which in turn, when inserted in equation (2.99), reveals a modified mechanical susceptibility;

$$x(\omega)\left(\chi_m^{-1}(\omega) + \chi_{\text{opt}}^{-1}(\omega)\right) = 0, \tag{2.102}$$

where

$$\chi_m^{-1}(\omega) = m_{\text{eff}}(-\omega^2 - \mathrm{i}\omega\Gamma_m + \omega_m^2), \tag{2.103}$$

and

$$\chi_{\text{opt}}^{-1}(\omega) = \hbar G|\alpha|\left(\frac{-\mathrm{i}G|\alpha|}{-\mathrm{i}(\Delta+\omega)+\kappa/2} + \frac{\mathrm{i}G|\alpha|}{\mathrm{i}(\Delta-\omega)+\kappa/2}\right) \tag{2.104a}$$

$$= \hbar G^2|\alpha|^2\left[i\left(\frac{\kappa/2}{(\Delta+\omega)^2+\kappa^2/4} - \frac{\kappa/2}{(\Delta-\omega)^2+\kappa^2/4}\right)\right.$$
$$\left. + \left(\frac{\Delta+\omega}{(\Delta+\omega)^2+\kappa^2/4} - \frac{\Delta-\omega}{(\Delta-\omega)^2+\kappa^2/4}\right)\right]. \tag{2.104b}$$

By defining an effective susceptibility as[19]

$$\chi_{\text{eff}}^{-1}(\omega) := \left(\chi_m^{-1}(\omega) + \chi_{\text{opt}}^{-1}(\omega)\right), \tag{2.105}$$

and setting

$$\chi_{\text{eff}}^{-1}(\omega) = m_{\text{eff}}(\omega^2 - i\omega\Gamma_{\text{eff}} + \omega_{\text{eff}}^2), \tag{2.106}$$

it follows that

$$\Gamma_{\text{eff}} = \Gamma_m + \frac{1}{\omega m_{\text{eff}}}\mathrm{Im}(\chi_{\text{opt}}^{-1}), \tag{2.107}$$

[18] In order to avoid disorientation we recall our Fourier transformation convention; $a^*(\omega) = \mathcal{F}[a^*](\omega)$.

[19] It is perhaps a bit confusing with the subscript "eff" now referring both to the effective mass and optically modified spring qualities, two completely unrelated origins of "effectiveness", but this is standard notation in the field.

and similarly that

$$\omega_{\text{eff}} = \sqrt{\omega_m^2 + \frac{1}{m_{\text{eff}}}\text{Re}(\chi_{\text{opt}}^{-1})} \approx \omega_m + \frac{1}{2}\frac{\text{Re}(\chi_{\text{opt}}^{-1})}{m_{\text{eff}}\omega_m}, \tag{2.108}$$

provided that the frequency shift is small compared to the mechanical frequency. Thus, we identify the optically induced damping and frequency shift (often denoted respectively *optical damping* and *optical spring* [Aspelmeyer et al., 2014]) as

$$\Gamma_{\text{opt}}(\omega) = \frac{2g^2\omega_m}{\omega}\left(\frac{\kappa/2}{(\Delta+\omega)^2+\kappa^2/4} - \frac{\kappa/2}{(\Delta-\omega)^2+\kappa^2/4}\right), \tag{2.109}$$

and

$$\delta\omega_{\text{opt}}(\omega) = g^2\left(\frac{\Delta+\omega}{(\Delta+\omega)^2+\kappa^2/4} - \frac{\Delta-\omega}{(\Delta-\omega)^2+\kappa^2/4}\right), \tag{2.110}$$

where we utilise that $\hbar/m_{\text{eff}} = 2x_{\text{ZPF}}^2\omega_m$ to rewrite the prefactor in terms of the experimentally more readily accessible coupling g. Finally, for coupling rates much smaller than the cavity linewidth ($g \ll \kappa$), we may replace the full frequency dependent damping and resonance shift by their values evaluated at the mechanical frequency. We thus define the optical damping and frequency shift as

$$\Gamma_{\text{opt}} := \Gamma_{\text{opt}}(\omega_m), \quad \delta\omega_{\text{opt}} := \delta\omega_{\text{opt}}(\omega_m). \tag{2.111}$$

By furthermore invoking the standard Lorentzian approximation for the mechanical susceptibility (see equation (2.45)) and keeping the effective temperature in mind (see equation (2.52)), a clear prediction emerges for the behaviour of the mechanical response; as the coupling is increased a Lorentzian peak shifts, broadens and becomes smaller. In Figure 2.8 we show a comparison between spectral data from our experiment and model prediction as we, for a fixed input power, gradually decrease the laser detuning and thereby increase the amount of light present in the cavity. There is very good qualitative agreement between data and model.

One important consequence of the modified susceptibility of equation (2.106) is the emergence of a new *effective* mode temperature. Replacing $\chi_m(\omega)$ with $\chi_{\text{eff}}(\omega)$ in equation 2.37 for the displacement PSD, and carrying out the integral of equation (2.48), one finds that

$$\int_{-\infty}^{\infty} S_{xx}(\omega)\frac{\mathrm{d}\omega}{2\pi} = \int_{-\infty}^{\infty} S_{F_{\text{th}}F_{\text{th}}}(\omega)|\chi_{\text{eff}}(\omega)|^2\frac{\mathrm{d}\omega}{2\pi} = \frac{\Gamma_m}{\Gamma_{\text{opt}}}\frac{k_BT}{m_{\text{eff}}\omega_{\text{eff}}^2}. \tag{2.112}$$

At the new mechanical frequency, the mechanics respond to the bath as if it were a bath of temperature T_{eff}, where

$$T_{\text{eff}} = \frac{\Gamma_m}{\Gamma_{\text{eff}}}T = \frac{\Gamma_m}{\Gamma_m + \Gamma_{\text{opt}}}T, \tag{2.113}$$

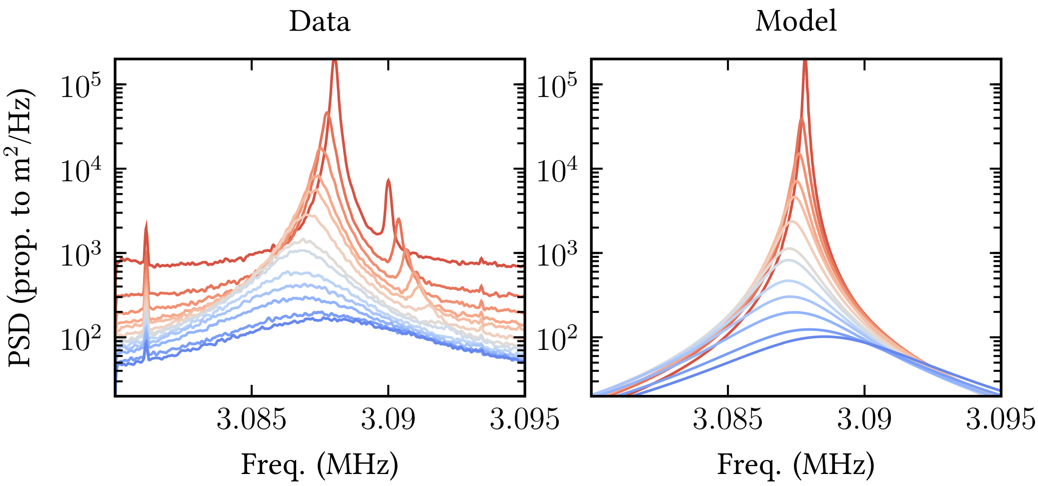

Figure 2.8: Cooling in practice. Left: measured spectral response of the (4, 1) mode. Right: The model using equation (2.111) and independently measured values of κ, Δ and g. The amplitude is fixed from a single fit to the first data trace.

in agreement with the treatment of section 2.2.3 (in particular equation (2.54)).

Note that the effective mechanical temperature only decreases when the optical broadening is positive. From equation (2.109) we see that only negative detunings yield a positive broadening. For positive detunings, the broadening is negative, leading to a heating (amplification) of the mechanics. When $\Gamma_{\text{opt}} = -\Gamma_m$, the so-called *parametric instability* sets in. From an experimental viewpoint, this is very disadvantageous. We discuss this further in chapter 3.

It is of general interest and particular necessity in section 3.7.2 to examine when the optically induced damping is largest, for a given cavity linewidth and mechanical frequency. In other words, we are interested in the detuning Δ_{ex} for which

$$\left.\frac{\mathrm{d}\Gamma_{\text{opt}}}{\mathrm{d}\Delta}\right|_{\Delta=\Delta_{ex}} = 0. \tag{2.114}$$

With a bit of algebra[20] we find that

$$\Delta_{ex} = \pm\sqrt{-\frac{\kappa^2}{12} + \frac{\omega_m^2}{3} + \frac{1}{6}\sqrt{\kappa^4 + 4\kappa^2\omega_m^2 + 16\omega_m^4}}, \tag{2.115}$$

with the positive solution corresponding to the minimum (largest heating) and the negative solution corresponding to the maximum (largest cooling). Equation (2.115), although a bit unwieldy at first sight, is easily interpreted in the two limits

[20] In this case performed with the aid of SymPy.

of respectively $\omega_m \gg \kappa$ and $\kappa \gg \omega_m$. In both cases, a zeroth-order approximation suffices. In the former case, one obtains

$$\Delta_{ex} \approx \pm\omega_m \quad (\omega_m \gg \kappa), \tag{2.116}$$

which, by inspection of equation (2.109), is expected, as the two Lorentzian contributions are well separated (resolved) and the maximum (minimum) will simply be at the peak position of either Lorentzian. In the latter case,

$$\Delta_{ex} \approx \pm\frac{\kappa}{\sqrt{12}} \quad (\omega_m \ll \kappa), \tag{2.117}$$

which is also expected, as this is the steepest point of the cavity Lorentzian, and therefore the point of maximal sideband asymmetry in the relevant limit where ω_m is small. In Figure 2.9 we display some graphs to aid this intuition. Note that it only holds classically that the largest Γ_{opt} by necessity corresponds to the lowest effective temperature. We explore this more in the next section.

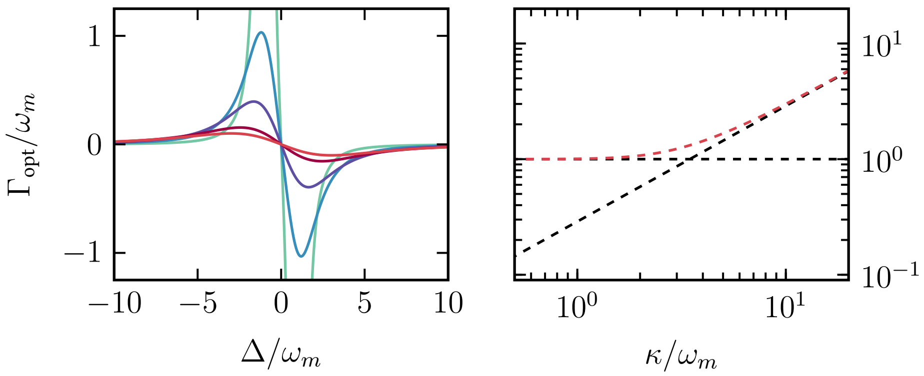

Figure 2.9: Optimal detuning. Left: Γ_{opt} as a function of detuning for different κ-values; κ/ω_m is 1 (green), 3 (blue), 5 (purple), 8 (burgundy), 10 (red), and $g = \omega_m$. Right: the optimal detuning (for heating) over a large range of sideband-resolution degrees. Also shown are the two asymptotes, $\Delta_{ex} = \omega_m$ and $\Delta_{ex} = \kappa/\sqrt{12}$.

The classical cooling theory presented so far already captures the main features of optomechanical sideband cooling. It does not, however, correctly predict the ultimate limit on the achievable occupation. Nothing we have said in this section contradicts the classical picture of coupled reservoirs presented in section 2.2.3, and equation (2.113) evidently allows for arbitrarily low phonon occupation. To obtain the proper limit and thereby answer the burning question of whether and when ground state cooling is (at least theoretically) possible is the goal of the next section.

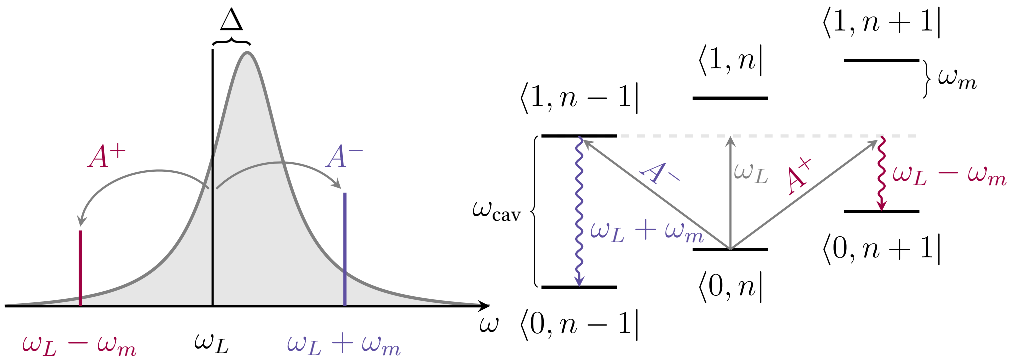

Figure 2.10: Quantum sideband picture of cooling. In the level diagram to the right, we have set $\Delta = -\omega_m$ and taken $\kappa \ll \omega_m$. The quantum states are joint Fock states of light and mechanics and the ratio $\omega_m/\omega_{\text{cav}}$ is exaggerated for clarity.

2.3.4.2 Quantum picture

As is often the case in physics, much can be learned from simple energy considerations. We saw in equations (2.100) and (2.101) that the mechanical motion generates sidebands on the laser drive. The frequency and thus the energy of the sideband photons differ from that of the carrier field by exactly a mechanical phonon energy, and the creation/annihilation of phonons in the mechanical resonator is therefore required for the sideband appearance to conserve energy. The presence of a cavity creates an imbalance between the sidebands and thereby favour either cooling or heating. This is indeed the essence of the sideband cooling mechanism. In Figure 2.10 we display a diagrammatic overview and introduce the two scattering rates A^+ and A^-. The rest of this section will be devoted to calculating these rates and obtaining a final cooling prediction.

For the final occupation number, we invoke the jump rate picture introduced in section 2.2.3. We remind ourselves that the final phonon number will be given by (see equation (2.58))

$$\bar{n}_f = \frac{\Gamma_\uparrow}{\Gamma_\downarrow - \Gamma_\uparrow}. \tag{2.118}$$

As the two baths are completely independent, the effective jump rates are simply the sums of the contributions from the thermal bath and the light field;

$$\Gamma_\uparrow = A^+ + A^+_{\text{th}}, \quad \Gamma_\downarrow = A^- + A^-_{\text{th}}, \tag{2.119}$$

where, as discussed in section 2.2.3, $A^+_{\text{th}} = \bar{n}_{\text{th}}\Gamma_m$ and $A^-_{\text{th}} = (\bar{n}_{\text{th}} + 1)\Gamma_m$. To get actual expressions for A^+ and A^-, one may invoke Fermi's Golden Rule [Clerk et al., 2010]. For an oscillator subject to a Hamiltonian of the form[21]

$$\hat{H} = \hbar\omega_m \left(\hat{b}^\dagger\hat{b} + \frac{1}{2}\right) - \hbar G\hat{x}\hat{F}, \tag{2.120}$$

the transition rates (*not* the jump rates, see below) from state $|n\rangle$ to $|n+1\rangle$ respectively are given by

$$\Gamma_{n\to n+1} = G^2 |\langle n+1|\,\hat{x}\,|n\rangle|^2 S_{FF}(-\omega_m), \tag{2.121}$$

respectively

$$\Gamma_{n\to n-1} = G^2 |\langle n-1|\,\hat{x}\,|n\rangle|^2 S_{FF}(\omega_m). \tag{2.122}$$

As in our case $\hat{F} = \hat{n}$, the relevant PSD is the photon number spectrum $S_{nn}(\omega)$. This can be calculated [Marquardt et al., 2007] to be given by

$$S_{nn}(\omega) = \bar{n}_{\text{cav}} \frac{\kappa}{(\omega+\Delta)^2 + (\kappa/2)^2}. \tag{2.123}$$

The matrix elements of equations (2.121) and (2.122) are directly evaluated to yield $x_{\text{ZPF}}^2(n+1)$ and $x_{\text{ZPF}}^2 n$, that is,

$$\Gamma_{n\to n+1} = (n+1) g_0^2 S_{nn}(-\omega_m), \tag{2.124}$$

and

$$\Gamma_{n\to n-1} = g_0^2 n S_{nn}(\omega_m). \tag{2.125}$$

By direct comparison with the master equation (2.55), we see that $\Gamma_{n\to n-1} = nA^-$ and $\Gamma_{n\to n+1} = (n+1)A^+$, which leads us to identify

$$A^- - A^+ = \bar{n}_{\text{cav}} g_0^2 \left(\frac{\kappa}{(\omega+\Delta)^2 + (\kappa/2)^2} - \frac{\kappa}{(-\omega+\Delta)^2 + (\kappa/2)^2} \right) \tag{2.126a}$$

$$= \Gamma_{\text{opt}}. \tag{2.126b}$$

This result is intuitively appealing; the broadening of the mechanical mode can indeed be viewed as a damping, both in the form of a coupling to a reservoir and a net dissipation rate. With all this in place, the full expression for the phonon occupation may finally be evaluated. We find that

$$\bar{n}_f = \frac{A^+ + \bar{n}_{\text{th}}\Gamma_m}{\Gamma_{\text{opt}} + \Gamma_m}. \tag{2.127}$$

[21] For clarity, we omit the terms involving only light.

It is of course interesting to inquire what the *minimal* obtainable occupation is in the absence of mechanical dissipation. It follows directly that

$$\bar{n}_{\text{min}} = \frac{A^+}{\Gamma_{\text{opt}}} = \left(\frac{(\omega_m - \Delta)^2 + (\kappa/2)^2}{(\omega_m + \Delta)^2 + (\kappa/2)^2} - 1 \right)^{-1}, \tag{2.128}$$

whence we can rewrite equation (2.127) in the slightly more suggestive form

$$\bar{n}_f = \frac{\Gamma_{\text{opt}} \bar{n}_{\text{min}} + \bar{n}_{\text{th}} \Gamma_m}{\Gamma_{\text{opt}} + \Gamma_m}. \tag{2.129}$$

This expression very closely resembles equation (2.52), only expressed in phonon numbers rather than temperatures. Now we may clearly pinpoint where the classical prediction of equation (2.54) went wrong; the effective temperature of the light field is not simply zero. Instead, one can re-express equation (2.128) in terms of an effective light noise temperature to find that

$$T_{\text{eff, light}} = \frac{\hbar \omega_{\text{cav}}}{k_B (\log(S_{nn}(\omega_m)) - \log(S_{nn}(-\omega_m)))}. \tag{2.130}$$

In other words, the quantum fluctuations of the light act as a stochastic force, mediated by radiation pressure, heating the membrane. Without going into a detailed discussion, we emphasise that *classical* fluctuations of the laser will have a similar effect. Random phase of amplitude fluctuations of the laser in a spectral region near the mechanics are added on top of the shot noise, leading to an even higher effective occupation of the laser. For a ground state cooling experiment, it is therefore of utmost importance to be limited by only shot noise in the laser. We return to this subject again in section 3.3.1 when we characterise the light source used in the experiment.

Aside from that, we note from equation (2.129) that the presence of $\bar{n}_{\text{min}}$ can shift the detuning yielding the lowest phonon occupancy away from the detuning yielding the largest optical broadening. This is most pronounced in the unresolved sideband regime, where $\bar{n}_{\text{min}}$ is larger. In Figure 2.11 we plot the quantum limit for sideband cooling for a range of different ratios κ/ω_m. It is seen that sideband resolution (having $\omega > \kappa$) is, although desirable, not strictly necessary in order for the ground state to be reachable[22].

Finally, it is interesting to cast the condition for ground state cooling in terms of the quantum cooperativity. In the highly resolved sideband limit, $\omega_m \gg \kappa$, the

[22]Where, as always, we by "ground state" mean $\bar{n} < 1$

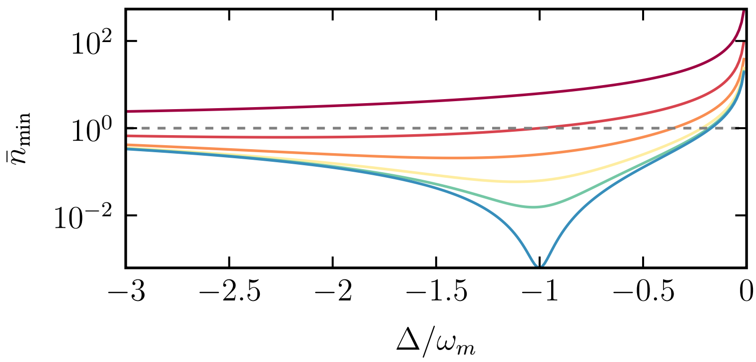

Figure 2.11: Minimal achievable phonon number for different degrees of sideband resolution. The "resolution parameter" κ/ω_m is varied; blue: 0.1, green: 0.5, yellow: 1, orange: 2, red: 4, burgundy: 10.

following two approximations can be made:

$$\bar{n}_f \approx \frac{\Gamma_m \bar{n}_{\rm th}}{\Gamma_{\rm opt}}, \quad \Gamma_{\rm opt} \approx \frac{4g^2}{\kappa}. \tag{2.131}$$

In that limit, we then obtain the important result that

$$C_q > 1 \Rightarrow \bar{n}_f < 1. \tag{2.132}$$

Outside the highly resolved sideband regime things get a bit more murky, so we turn to numerical solutions. For a given ratio between the cavity linewidth and the mechanical frequency, we ask what the minimal quantum cooperativity needed to achieve $\bar{n}_f < 1$ is. This of course hinges on the detuning (but not on $\bar{n}_{\rm th}$!), and we must make some choice for this parameter. We have not been able to find a closed-form expression for the detuning generally yielding the lowest phonon occupancy, but we know that equation (2.115) is optimal in the resolved sideband limit and that $\Delta = -\kappa/2$ is optimal in the very unresolved limit [Aspelmeyer et al., 2014]. By combining the results of those two limits, the picture of Figure 2.12 emerges. As the mechanical frequency grows relatively to the cavity linewidth, a larger quantum cooperativity is called for, but the demand is not dramatically increased even in the moderately unresolved regime.

2.3.5 Quantum Power Spectral Densities

We now turn our attention to the linearised equations of motion and the important task of calculating the measured spectra coming out of the cavity. Our goal

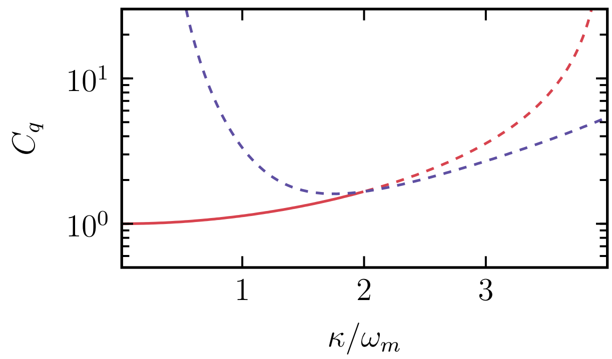

Figure 2.12: The quantum cooperativity required for ground state cooling. The red curve corresponds to the detuning yielding maximal broadening. The purple curve corresponds to $\Delta = -\kappa/2$.

is to develop a numerical model that we may compare directly to data. The calculation is done in two steps; first we calculate all intra-cavity quantities using the linearised Heisenberg-Langevin equations and next we apply input-output theory to calculate the spectra of light coming out of the cavity.

2.3.5.1 Inside the Cavity

When considering the power spectral densities of light and mechanics, the most natural point of departure is to cast the equations in terms of quadrature operators. We define

$$\hat{Q} := \frac{1}{\sqrt{2}}(\hat{b}^\dagger + \hat{b}), \quad \hat{P} := \frac{i}{\sqrt{2}}(\hat{b}^\dagger - \hat{b}), \tag{2.133}$$

and

$$\hat{X} := \frac{1}{\sqrt{2}}(\hat{a}^\dagger + \hat{a}), \quad \hat{Y} := \frac{i}{\sqrt{2}}(\hat{a}^\dagger - \hat{a}), \tag{2.134}$$

and note that

$$\hat{Q} = \frac{1}{\sqrt{2}x_{\text{ZPF}}}\hat{x}, \quad \hat{P} = \frac{1}{\sqrt{2}p_{\text{ZPF}}}\hat{p}. \tag{2.135}$$

By direct substitution, the linearised equations of motion for the mechanics, equations (2.94) and (2.95), may then be recast as

$$\frac{\mathrm{d}}{\mathrm{d}t}\hat{Q} = \omega_m \hat{P}. \tag{2.136}$$

and

$$\frac{\mathrm{d}}{\mathrm{d}t}\hat{P} = -\Gamma_m \hat{P} - \sqrt{2\Gamma_m}\hat{P}_{\text{in}} - \omega_m \hat{Q} - 2g\hat{X}, \tag{2.137}$$

where we have introduced the mechanical input noise operator $\hat{P}_{\text{in}}$, given by

$$\hat{P}_{\text{in}} = \frac{x_{\text{ZPF}}}{\hbar\sqrt{\Gamma_m}}\hat{F}_{\text{th}}. \tag{2.138}$$

Similarly, we have for $\hat{X}$ and $\hat{Y}$ that

$$\frac{\mathrm{d}}{\mathrm{d}t}\hat{X} = -\frac{\kappa}{2}\hat{X} - \Delta\hat{Y} + \sqrt{\kappa}\hat{X}_{\text{in}}, \tag{2.139}$$

$$\frac{\mathrm{d}}{\mathrm{d}t}\hat{Y} = -\frac{\kappa}{2}\hat{Y} + \Delta\hat{X} + 2g\hat{Q} + \sqrt{\kappa}\hat{Y}_{\text{in}}. \tag{2.140}$$

Now, the great virtue of these equations is their linearity, which allows us to compactly recast them in matrix form;

$$\frac{\mathrm{d}}{\mathrm{d}t}\begin{pmatrix}\hat{X}\\ \hat{Y}\\ \hat{Q}\\ \hat{P}\end{pmatrix} = \begin{pmatrix}-\kappa/2 & -\Delta & 0 & 0\\ \Delta & -\kappa/2 & 2g & 0\\ 0 & 0 & 0 & \omega_m\\ 2g & 0 & -\omega_m & -\Gamma_m\end{pmatrix}\begin{pmatrix}\hat{X}\\ \hat{Y}\\ \hat{Q}\\ \hat{P}\end{pmatrix} + \begin{pmatrix}\hat{\mathcal{X}}_{\text{in}}\\ \hat{\mathcal{Y}}_{\text{in}}\\ \hat{\mathcal{Q}}_{\text{in}}\\ \hat{\mathcal{P}}_{\text{in}},\end{pmatrix} \tag{2.141}$$

with proper (re-)definitions of the input noise operators;

$$\begin{pmatrix}\hat{\mathcal{X}}_{\text{in}}\\ \hat{\mathcal{Y}}_{\text{in}}\\ \hat{\mathcal{Q}}_{\text{in}}\\ \hat{\mathcal{P}}_{\text{in}},\end{pmatrix} = \begin{pmatrix}\sqrt{\kappa}\hat{X}_{\text{in}}\\ \sqrt{\kappa}\hat{Y}_{\text{in}}\\ 0\\ \sqrt{2\Gamma_m}\,\hat{P}_{\text{in}}\end{pmatrix}. \tag{2.142}$$

Using matrix notation to rewrite equation (2.141) as

$$\frac{\mathrm{d}}{\mathrm{d}t}\mathbf{V}(t) = \underline{\mathbf{M}}\mathbf{V}(t) + \mathbf{V}^{\text{in}}(t), \tag{2.143}$$

we obtain the following solution in the frequency domain:

$$\mathbf{V}(\omega) = -(\mathrm{i}\omega\mathbb{1} + \underline{\mathbf{M}})^{-1}\mathbf{V}^{\text{in}}(\omega). \tag{2.144}$$

From the solution hereto, we may calculate all spectra, once the noise correlators have been specified. The noise correlators may be compactly expressed in the covariance matrix, $\underline{\Sigma}$, given by

$$\Sigma_{ij}(\omega', \omega) = \left\langle \mathbf{V}_i^{\text{in}}(\omega')\mathbf{V}_j^{\text{in}}(\omega)\right\rangle. \tag{2.145}$$

If we define a new matrix $\underline{\mathbf{L}}$ as

$$\underline{\mathbf{L}} = -(\mathrm{i}\omega\mathbb{1} + \underline{\mathbf{M}})^{-1}, \tag{2.146}$$

equation (2.144) can be re-expressed as

$$\mathbf{V}_i(\omega) = \sum_{j=1}^{4} L_{ij}(\omega)\mathbf{V}_j^{\text{in}}(\omega). \tag{2.147}$$

We may then compactly write the spectrum of any quadrature operator as

$$\begin{aligned} S_{\mathbf{V}_i\mathbf{V}_i}(\omega) &= \int_{-\infty}^{\infty} \langle \mathbf{V}_i(\omega')\mathbf{V}_i(\omega)\rangle \frac{\mathrm{d}\omega'}{2\pi} &(2.148)\\ &= \int_{-\infty}^{\infty} \sum_{j,l=1}^{4} L_{ij}(\omega')\Sigma_{jl}(\omega',\omega)L_{il}(\omega)\frac{\mathrm{d}\omega'}{2\pi} &(2.149)\\ &= \int_{-\infty}^{\infty} \frac{\mathrm{d}\omega'}{2\pi} \left(\underline{\mathbf{L}}(\omega')\underline{\Sigma}(\omega',\omega)\underline{\mathbf{L}}^T(\omega)\right)_{ii}. &(2.150) \end{aligned}$$

In the Markovian limit, $\underline{\Sigma}$ takes the following simple form:

$$\underline{\Sigma} = \underline{\mathbf{T}}\delta(\omega' + \omega), \tag{2.151}$$

where

$$\underline{\mathbf{T}} = \begin{pmatrix} \kappa/2 & i\kappa/2 & 0 & 0 \\ -i\kappa/2 & \kappa/2 & 0 & 0 \\ 0 & 0 & 0 & 0 \\ 0 & 0 & 0 & 2\Gamma_m(\bar{n}_{\text{th}} + 1/2) \end{pmatrix}, \tag{2.152}$$

and the expression for the spectrum simplifies somewhat to become

$$S_{\mathbf{V}_i\mathbf{V}_i}(\omega) = \left(\underline{\mathbf{L}}(-\omega)\underline{\mathbf{T}}\underline{\mathbf{L}}^T(\omega)\right)_{ii}. \tag{2.153}$$

This last equation, although difficult to penetrate analytically, is easily evaluated numerically, since the matrix inversion of equation (2.146) only ever needs to be performed once. Note that some simplification takes place when one considers the symmetrised PSD. Upon the symmetrisation, terms proportional to non-diagonal elements of $\underline{\mathbf{T}}$ cancel out, such that

$$\bar{S}_{\mathbf{V}_i\mathbf{V}_i}(\omega) = \sum_{j=1}^{4} L_{ij}(-\omega)L_{ij}(\omega)T_{jj}. \tag{2.154}$$

As an example, we consider $\bar{S}_{QQ}(\omega)$.

$$\begin{aligned} \bar{S}_{QQ}(\omega) = \frac{\kappa}{2}L_{31}(-\omega)L_{31}(\omega) + \frac{\kappa}{2}L_{32}(-\omega)L_{32}(\omega) \\ +2\Gamma_m(\bar{n}_{\text{th}} + 1/2)L_{34}(-\omega)L_{34}(\omega). \end{aligned} \tag{2.155}$$

Even this rewriting is, however, somewhat intractable analytically due to the involved expressions for the L_{ij}. In section 2.3.6 we solve the Heisenberg-Langevin equations exactly for the light amplitude quadrature. For now we proceed with the numerical modelling.

2.3.5.2 Outside the Cavity

The spectrum we measure is that of the light field emanating from the cavity. To calculate the output operator of this field, we must account for extraneous losses. Not all light that has interacted with the mechanics is being collected by the photodetector. Some is lost through the input port (remember that we measure in transmission), some disappears due to lossy optics on the way to the detector, and some might even be scattered out of the cavity. Whatever the reason, all these losses may be lumped together into a single vacuum noise term replacing a part of the correlated signal. The input-output relation for $\hat{X}$ then reads

$$\hat{X}_{\text{out}} = \sqrt{\eta}(\hat{X}_{\text{in}} + \sqrt{\kappa}\hat{X}) + \sqrt{1-\eta}\hat{X}_{\text{vac}}. \tag{2.156}$$

The losses are parametrised through the detection efficiency η, which is bounded from above by the cavity coupling parameter η_c. Having $\eta = \eta_c$ corresponds to perfect detection with light only escaping through the cavity input port.

Using the machinery and notation of section 2.3.5.1, the spectrum of $\hat{X}_{\text{out}}$ is found to be

$$\begin{aligned}\bar{S}_{X_{\text{out}}X_{\text{out}}}(\omega) = \eta\kappa S_{XX}(\omega) + \frac{1}{2}[1 - \eta\kappa(L_{11}(-\omega) + L_{11}(\omega))]\\ -\frac{1}{2}[\eta\kappa(L_{12}(-\omega) + L_{21}(\omega))].\end{aligned} \tag{2.157}$$

Upon symmetrisation, this expression takes the even simpler form

$$\bar{S}_{X_{\text{out}}X_{\text{out}}}(\omega) = \eta\kappa\bar{S}_{XX}(\omega) + \frac{1}{2} - \eta\kappa\bar{L}_{11}(\omega). \tag{2.158}$$

Although still intended for numerical evaluation, it is possible to argue a bit for the correctness of this last equation. First of all, it is compelling that what comes out is indeed the intracavity spectrum, only with some added noise modifications. Both of these modifications have a clear interpretation. For $\eta = 0$, one measures only vacuum noise, which does not have a zero value, but rather (in our convention) a value of $1/2$, explaining the presence of a constant term. Secondly, when $g = 0$ we should also expect a flat spectrum, which is not guaranteed by $\bar{S}_{XX}$, since this quantity describes the amount of intra-cavity fluctuations, and these are modulated by the cavity response. The third term can be thought of as "ensuring" the cancellation of the cavity response so as to generate a flat spectrum of shot noise. In Figure 2.13 we show an explanatory picture of $\bar{S}_{XX}(\omega)$ and $\bar{S}_{X_{\text{out}}X_{\text{out}}}(\omega)$ in two important regimes. We also show the very important $\bar{S}_{QQ}(\omega)$, which we shall use in chapter 4 to calculate phonon occupations (see below).

The plots in Figure 2.13 illustrate several important points. We see that $\bar{S}_{XX}$ does indeed have some overall shape plus a mechanical response, whereas $\bar{S}_{X_{\text{out}}X_{\text{out}}}$ is flat everywhere except near the mechanics. Furthermore, the spectral features of the output light do not exactly mimic the shape of the mechanics, unlike in the classical limit (cf. Figure 2.8). In fact, in a certain spectral region, the output light noise is *squeezed* below the shot noise level. This effect, a clear quantum signature, is denoted *ponderemotive squeezing* and further explored in the next section. Finally, we see the expected shift and damping of the mechanical spectrum. We stress that since the model makes a simultaneous prediction for $\bar{S}_{X_{\text{out}}X_{\text{out}}}$ and $\bar{S}_{QQ}$, it suffices to measure one in order to determine the other.

Finally, we show how the mechanical phonon occupation follows from $\bar{S}_{QQ}(\omega)$. First, we realise that the symmetrised PSD of $\hat{x}$ in the classical limit should equal the PSD of the classical variable z, i.e.

$$\bar{S}_{xx}(\omega) = S_{zz}(\omega). \tag{2.159}$$

Next, using argument similar to the ones used in section 2.2.3, we may write

$$\int_{-\infty}^{\infty} \bar{S}_{xx}(\omega)\frac{\mathrm{d}\omega}{2\pi} = \frac{1}{m_{\text{eff}}\omega_m^2}\left\langle \hat{H} \right\rangle = \frac{\hbar\omega_m}{m_{\text{eff}}\omega_m^2}\left(\bar{n} + \frac{1}{2}\right). \tag{2.160}$$

Finally, since $\sqrt{2}x_{\text{ZPF}}\hat{Q} = \hat{x}$, it follows that

$$\int_{-\infty}^{\infty} \bar{S}_{QQ}(\omega)\frac{\mathrm{d}\omega}{2\pi} = \frac{m_{\text{eff}}\omega_m}{\hbar}\int_{-\infty}^{\infty} \bar{S}_{xx}(\omega)\frac{\mathrm{d}\omega}{2\pi} = \bar{n} + \frac{1}{2}. \tag{2.161}$$

This of course agrees with the results of section 2.2.3 in the classical limit where $\left\langle \hat{H} \right\rangle \to k_B T$.

2.3.6 Ponderemotive Squeezing

On an intuitive level, it is reasonable that the optomechanical interaction will squeeze the cavity light field. After all, an amplitude-dependent phase shift is what the mechanics impinge, meaning that the phase and amplitude quadratures

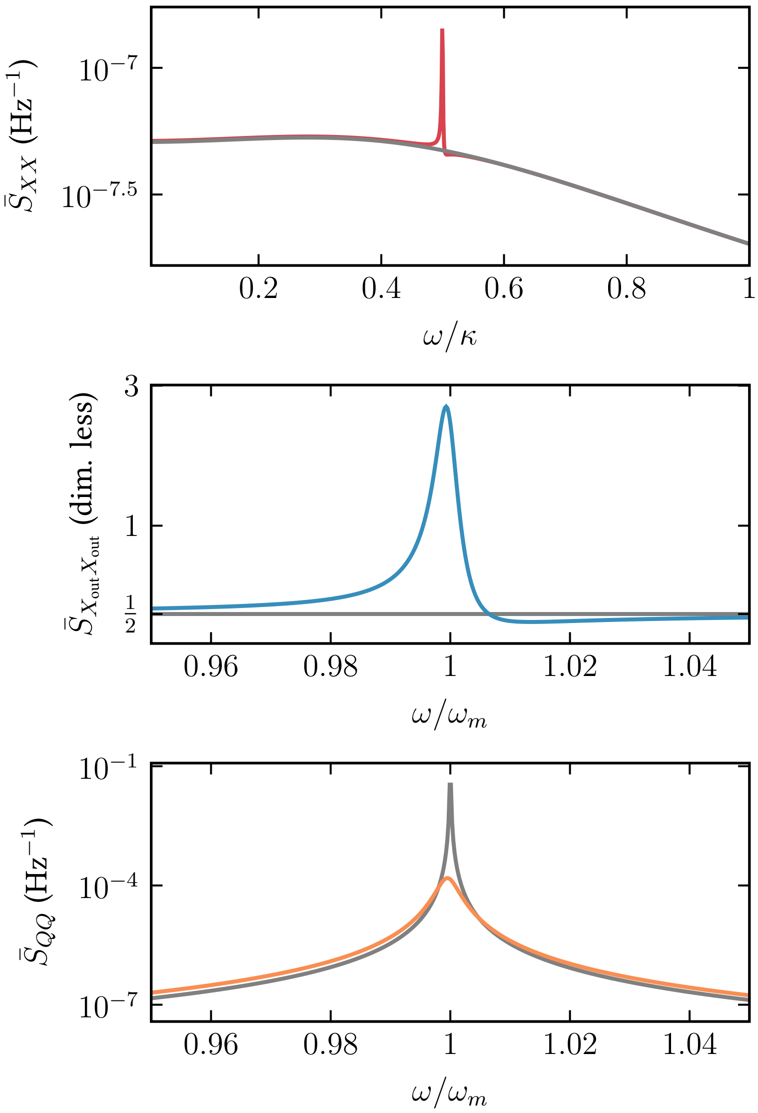

Figure 2.13: Quantum spectra. For each plot, the corresponding spectrum for $g = 0$ is shown in grey. Parameters used: $\kappa/2\pi = 4\,\text{MHz}$, $-\Delta/2\pi = 1.5\,\text{MHz}$, $\omega_m/2\pi = 2\,\text{MHz}$, $T = 10\,\text{K}$, $Q = 12 \times 10^7$, $g = 0.025\kappa$. Note the different frequency axes.

of the light will become correlated. In Figure 2.14 a conceptual model is shown, where two originally uncorrelated quadratures become correlated as the phase ($\hat{Y}$) is shifted proportionally to the amplitude ($\hat{X}$) value. If the correlation is strong enough, there exists a cut through the centre of the cloud along which the variance is less than of the vacuum. In such a case, we say that quantum noise is being squeezed.

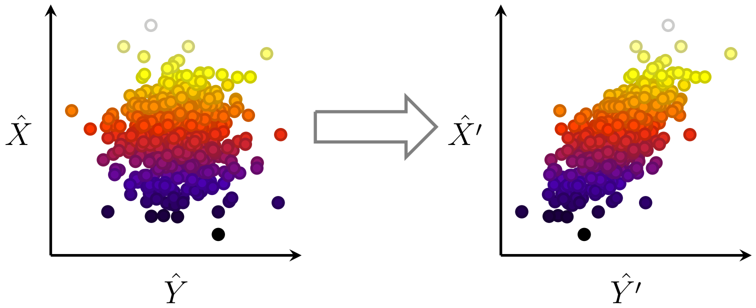

Figure 2.14: Conceptual squeezing model. A point of a certain colour on the left is mapped to a point with the same colour on the right.

We now analytically solve the Heisenberg-Langevin equations for the light quadratures. The overall plan of attack is to express first $\hat{X}$ and then $\hat{X}_{\text{out}}$ solely in terms of input noise operators, so that the output spectrum may be evaluated.

By introducing two cavity response functions, c_1 and c_2, defined by

$$c_1 := \frac{-2\Delta}{4\Delta^2 + (\kappa - 2\mathrm{i}\omega)^2}\kappa, \quad c_2 := \frac{\kappa - 2\mathrm{i}\omega}{4\Delta^2 + (\kappa - 2\mathrm{i}\omega)^2}\kappa, \tag{2.162}$$

we may recast equations (2.139) and (2.136) in the frequency domain as

$$\hat{X}(\omega) = \frac{4gc_1}{\kappa}\hat{Q}(\omega) + \frac{2}{\sqrt{\kappa}}(c_1\hat{Y}_{\text{in}}(\omega) + c_2\hat{X}_{\text{in}}(\omega)), \tag{2.163}$$

$$\hat{Q}(\omega) = \chi_m(\omega)\left(2g\hat{X}(\omega) + \sqrt{2\Gamma_m}\hat{P}_{\text{in}}(\omega)\right), \tag{2.164}$$

where we now define the mechanical susceptibility, χ_m, as

$$\chi_m(\omega) = \frac{\omega_m}{\omega_m^2 - \omega^2 - \mathrm{i}\Gamma_m\omega}. \tag{2.165}$$

Substituting the value of $\hat{X}$ of equation (2.163) into (2.164) then gives that

$$\hat{Q}(\omega) = \chi_{\text{eff}}(\omega)\left(\frac{4g}{\kappa}[c_1\hat{Y}_{\text{in}}(\omega) + c_2\hat{X}_{\text{in}}(\omega)] + \sqrt{2\Gamma_m}\hat{P}_{\text{in}}(\omega)\right), \tag{2.166}$$

where the effective susceptibility, χ_{eff}, is the same as the one of equation (2.106) with m_{eff} replaced by $1/\omega_m$, arising from us working now with the dimensionless quadrature operators. Finally, this expression may be substituted for $\hat{Q}$ in equation (2.163) to yield

$$\begin{aligned}\hat{X}(\omega) = \left(16\frac{g^2c_1}{\kappa}\chi_{\text{eff}}(\omega) + 2\right)\frac{1}{\sqrt{\kappa}}[c_1\hat{Y}_{\text{in}}(\omega) + c_2\hat{X}_{\text{in}}(\omega)] \\ + \frac{4gc_1}{\kappa}\chi_{\text{eff}}(\omega)\sqrt{2\Gamma_m}\hat{P}_{\text{in}}(\omega).\end{aligned} \tag{2.167}$$

Assuming for the sake of illustration an ideal detection efficiency $\eta = 1$, the output quadrature is given by

$$\hat{X}_{\text{out}}(\omega) = \hat{X}_{\text{in}}(\omega) - \sqrt{\kappa}\hat{X}(\omega) \tag{2.168}$$

$$\begin{aligned}= &- \left(16\frac{g^2c_1^2}{\kappa}\chi_{\text{eff}}(\omega) + 2c_1\right)\hat{Y}_{\text{in}}(\omega) \\ &- \left(16\frac{g^2c_1c_2}{\kappa}\chi_{\text{eff}}(\omega) + 2c_2 - 1\right)\hat{X}_{\text{in}}(\omega) \\ &- 4gc_1\chi_{\text{eff}}(\omega)\sqrt{2\Gamma_m}\hat{P}_{\text{in}}(\omega).\end{aligned} \tag{2.169}$$

The symmetrised PSD of the output fluctuations can be found using equation (2.154). One then obtains

$$\begin{aligned}\bar{S}_{X_{\text{out}}X_{\text{out}}}(\omega) = \frac{1}{2} &+ \left(\frac{16g^2}{\kappa\sqrt{2}}\right)^2|\chi_{\text{eff}}(\omega)|^2|c_1(c_1+c_2)|^2 \\ &+ \frac{16g^2}{\kappa}|\chi_{\text{eff}}(\omega)|^2|c_1|^2 2\Gamma_m(\bar{n}_{\text{th}} + \frac{1}{2}) \\ &+ \frac{16g^2}{\kappa}\text{Re}\left(\chi_{\text{eff}}(\omega)c_1(2c_1^2 + 2c_2^2 - c_2)\right).\end{aligned} \tag{2.170}$$

In order for squeezing of quantum noise to occur, the value of $\bar{S}_{X_{\text{out}}X_{\text{out}}}(\omega)$ must fall below $1/2$. The first three terms of equation are strictly positive and thus counteract any squeezing. We may physically interpret these contributions as the constant imprecision noise of the measurement, the quantum back-action and the transduced thermal noise. Finally, the fourth term embodying the light-mechanical correlations may become negative and thereby potentially produce squeezing. It is not immediately clear from these expressions what effect different optical parameters have on the squeezing, but it is directly seen that a low bath temperature and mechanical dissipation rate are desirable.

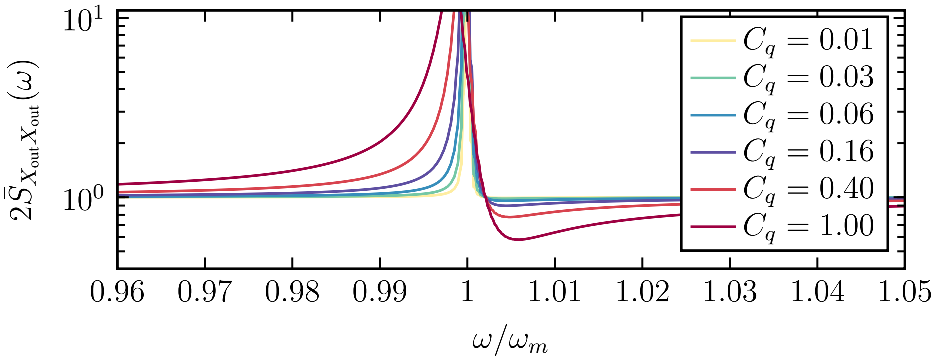

Figure 2.15: Squeezing improving with cooperativity. Parameters used: $\kappa/2\pi = 14\,\text{MHz}$, $\Delta/2\pi = -1.8\,\text{MHz}$, $\omega_m/2\pi = 2.5\,\text{MHz}$, $Q = 10\,\text{M}$, $T = 10\,\text{K}$.

In Figure 2.15 we illustrate how the degree of achieved squeezing grows with the quantum cooperativity, calculated with parameters similar to those of our experiment, but for an ideal detection efficiency.

In terms of experimental parameters, good squeezing is not achieved in the same region as good sideband cooling. Sideband resolution, so tremendously helpful for cooling, is of no aid in the squeezing endeavour. In Figure 2.16 we display the maximal amount of ponderomotive squeezing present in the output spectrum as the cavity linewidth and detuning are varied. For each trace, the cavity-enhanced coupling is adjusted so that the quantum cooperativity is one.

2.3.7 OMIT

Another interesting phenomenon emerging from the Heisenberg-Langevin equations of motion is that of *optomechanically induced transparency* (OMIT). First proposed in [Schließer, 2009, chapter 2] and shortly thereafter further theorised [Agarwal and Huang, 2010] and verified experimentally [Weis et al., 2010], the effect is now routinely demonstrated in optomechanical experiments. Indeed, to our ends, it serves as a diagnostic tool to measure three key parameters on which all of the previous effects depend, namely κ, Δ and g.

A weak phase modulation (probe) is applied to the input field will, by the cavity, be turned into an amplitude modulation which, at the mechanical frequency, will interfere with the sidebands already created by the mechanics on the strong laser drive (see equations (2.100) and (2.101)). This interference may be destructive or constructive, leading to either induced transparency or opaqueness.

For our purposes, the effect is purely classical in the sense that quantum noise

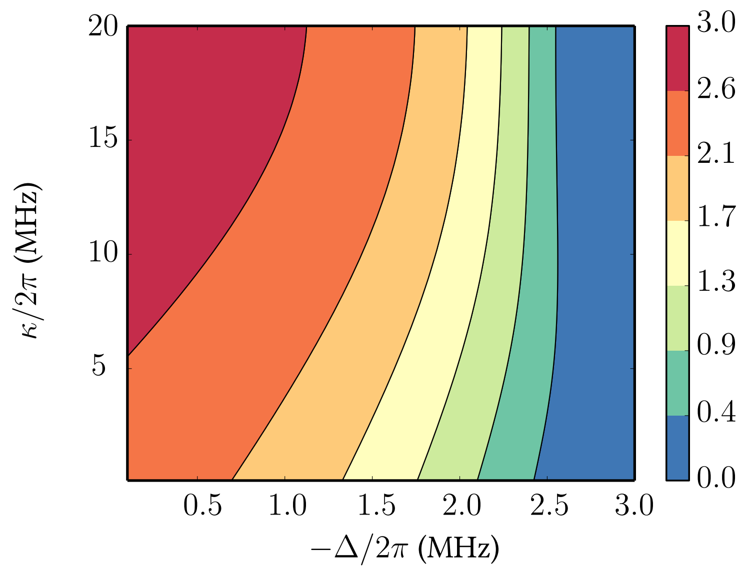

Figure 2.16: Maximal degree of squeezing (in dB) for unit quantum cooperativity. Other parameters are the same as those used in Figure 2.15.

plays no role in it. Our starting point is the linearised equations with all operators replaced by their (shifted) expectation values. This is once again equations (2.98) and (2.99), but keeping now the drive term, which will constitute the weak probe. In the frequency domain, these equations read

$$(-\mathrm{i}(\Delta+\omega)+\kappa/2)a(\omega) = \sqrt{\eta_c\kappa}\delta s_{\text{in}} - \mathrm{i}G\alpha\, x(\omega), \tag{2.171}$$

$$(\mathrm{i}(\Delta-\omega)+\kappa/2)a^*(\omega) = \sqrt{\eta_c\kappa}\delta s_{\text{in}}^* + \mathrm{i}G\alpha\, x(\omega), \tag{2.172}$$

$$(\omega_m^2-\omega^2-\mathrm{i}\Gamma_m\omega)x(\omega) = -\frac{\hbar G}{m_{\text{eff}}}\alpha(a^*+a). \tag{2.173}$$

Now, the cavity rotates the quadratures of the input field. Adopting the convention that our intracavity field is real, for the drive to be turned into intra-cavity amplitude modulations, δX, the phase of the drive must fulfil that (see [Schließer, 2009, appendix B])

$$\delta s_{\text{in}} = \frac{\mathrm{i}}{2}\frac{-\mathrm{i}\Delta+\kappa/2}{\sqrt{\Delta^2+(\kappa/2)^2}}\,\delta X, \qquad \delta s_{\text{in}}^* = -\frac{\mathrm{i}}{2}\frac{\mathrm{i}\Delta+\kappa/2}{\sqrt{\Delta^2+(\kappa/2)^2}}\,\delta X. \tag{2.174}$$

Note that δX is real. The signal measured at the output is

$$S(\omega) = \sqrt{\kappa_{\text{out}}}(a^*(\omega)+a(\omega)), \tag{2.175}$$

where the output coupling κ_{out} will actually play no role in the end. Insertion of

(2.173) into equations (2.171) and (2.172) yields that

$$a(\omega) = \chi_c(\omega)\left(\sqrt{\eta_c\kappa}\delta s_{\text{in}} + 2\mathrm{i}g^2\chi_m(\omega)(a^* + a)\right) \tag{2.176a}$$
$$a^*(\omega) = \chi_c^*(-\omega)\left(\sqrt{\eta_c\kappa}\delta s_{\text{in}}^* - 2\mathrm{i}g^2\chi_m(\omega)(a^* + a)\right), \tag{2.176b}$$

where

$$\chi_c(\omega) = \frac{1}{-i(\omega+\Delta)+\kappa/2}, \quad \chi_m(\omega) = \frac{\omega_m}{\omega_m^2 - \omega^2 - \mathrm{i}\Gamma_m\omega}, \tag{2.177}$$

and we have used that $\hbar G\alpha/m_{\text{eff}} = 2\omega_m g$. Solving equations (2.176) for $a^* + a$, we find that

$$S(\omega) = \kappa_{\text{out}}\frac{C(\omega)}{1 - M(\omega)}, \tag{2.178}$$

where

$$C(\omega) = \sqrt{\eta_c\kappa}\left(\chi_c(\omega)\delta s_{\text{in}} + \chi_c^*(-\omega)\delta s_{\text{in}}^*\right) \tag{2.179a}$$
$$= \sqrt{\eta_c\kappa}\,\delta X\left(\chi_c(\omega)\frac{\mathrm{i}}{2}\frac{|\chi_c(0)|}{\chi_c(0)} - \chi_c^*(-\omega)\frac{\mathrm{i}}{2}\frac{|\chi_c(0)|}{\chi_c^*(0)}\right), \tag{2.179b}$$

and

$$M(\omega) = 2\mathrm{i}g^2\chi_m(\omega)(\chi_c(\omega) - \chi_c^*(-\omega)). \tag{2.180}$$

In both functions, $C(\omega)$ and $M(\omega)$, the signal is seen to be the sum of the two sidebands present in the cavity at respectively $\pm\omega$. We may understand $C(\omega)$ as the response from the bare cavity, whereas $M(\omega)$ is the mechanical contribution to the signal. In Figure 2.17 we display the evolution of the two different contributions as the detuning is varied. As the overall amplitude is of no interest, we normalise the $C(\omega)$ plot such that the peak response is 1. An easily understandable pattern is observed; as the Fourier frequency approaches (minus) the detuning, the cavity responds with a response as wide as the cavity linewidth. Similarly, to ease gauging the depth of the OMIT dips, we have "normalised" by plotting just the $(1 - M(\omega))^{-1}$ part of $S(\omega)$ plots such that the asymptotic value is 1. Here, asymptotic should be understood as meaning that $\chi_{\text{eff}}(\omega)$ (as given by equation (2.106)) has become negligible. The true asymptotic value of $S(\omega)$ is of course $\approx C(\omega_m)$. As will be further described in section 3.2.2.2, this response is, once the amplitude has been normalised away, our door to gain access to κ, Δ and g.

2.3.7.1 Multi-mode OMIT

Whereas the previous section dealt with the interaction of a single mechanical mode and the light field, many real mechanical resonators, and indeed our mem-

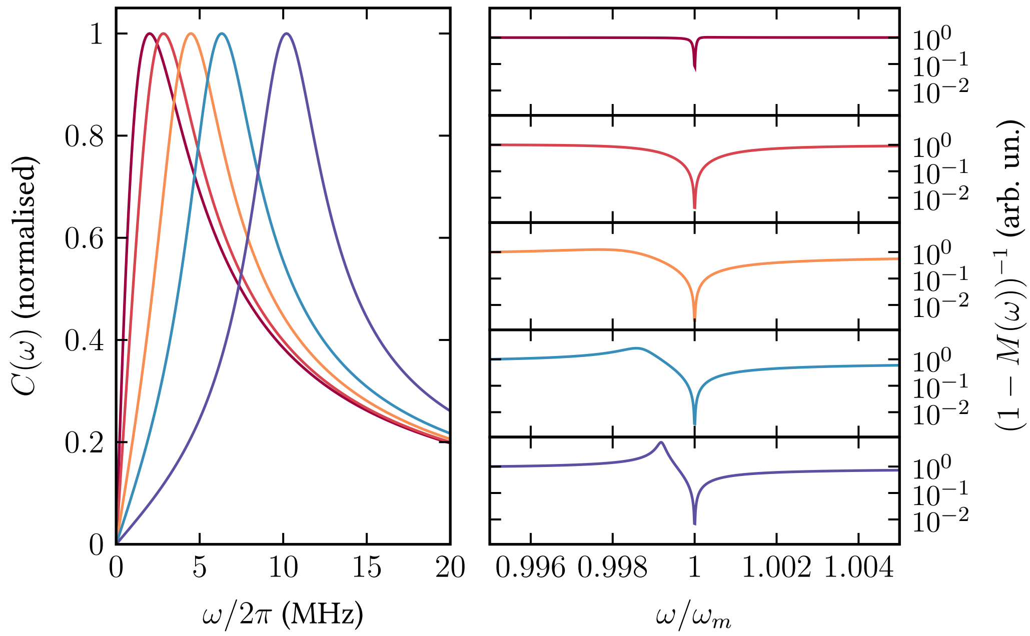

Figure 2.17: OMIT prediction. The plots show the broad (left) and narrow (right) features for different detunings. $\Delta/(2\pi\times 1\,\mathrm{MHz}) = \{0.1, 2, 4, 6, 10\}$ corresponding to respectively burgundy, red, orange, blue, and purple. Other parameters: $g/2\pi = 100\,\mathrm{kHz}$, $\kappa/2\pi = 4\,\mathrm{MHz}$, $\Gamma_m/2\pi = 0.125\,\mathrm{Hz}$, $\omega_m/2\pi = 2.5\,\mathrm{MHz}$. Normalisation explained in main text.

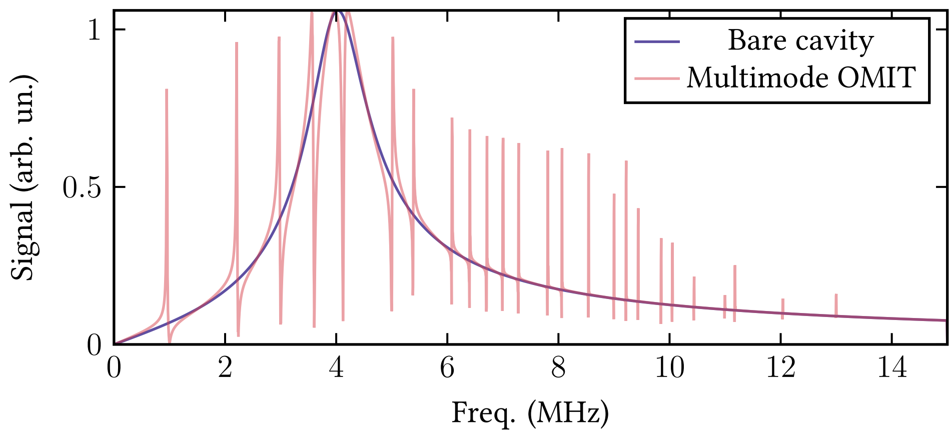

Figure 2.18: Multimode OMIT response and the bare cavity. Parameters used: $\Delta/2\pi = 4\,\mathrm{MHz}$, $\kappa/2\pi = 2\,\mathrm{MHz}$, $\omega_{11}/2\pi = 1\,\mathrm{MHz}$, $g_{11}/2\pi = 1.8\,\mathrm{MHz}$.

branes, sport a multitude of mechanical modes. Assuming these modes to be non-interacting, the model just developed is easily extended to encompass an arbitrary number of mechanical modes. For m mechanical modes, here for clarity labelled with a single index i, the equations of motion read

$$\chi_c^{-1}(\omega)a(\omega) = \sqrt{\eta_c\kappa}\delta s_{\text{in}} - \mathrm{i}\alpha\sum_i^m G_i x_i, \tag{2.181}$$

$$\chi_c^{-1}(\omega)a^*(\omega) = \sqrt{\eta_c\kappa}\delta s_{\text{in}}^* + \mathrm{i}\alpha\sum_i^m G_i x_i, \tag{2.182}$$

$$\chi_{m,i}^{-1}(\omega)x_i(\omega) = -\omega_{m,i}\frac{\hbar G_i}{m_{\text{eff},i}}\alpha(a^* + a). \tag{2.183}$$

Following a derivation completely analogous to the single mode case, one ends up with the very same expressions as equations (2.178) and (2.179), only with a modified M-function. The multi-mode version reads

$$M(\omega) = 2\mathrm{i}(\chi_c(\omega) - \chi_c^*(-\omega))\sum_i^m g_i^2\chi_{m,i}(\omega), \tag{2.184}$$

of which equation (2.180) is just the special case when $m = 1$. In Figure 2.18 we show a plot of the expected OMIT response of the first 105 modes[23] of a square membrane. We calculate the mode frequencies using equation (2.31) and calculate the different couplings using both the different zero-point fluctuations (equation (2.62)) for each mode and the *transverse overlap*, to be discussed in section 3.6.1, which makes the coupling to many of the modes vanish for a laser beam centred on the membrane.

The actual OMIT traces one encounters in the laboratory are very similar to that of Figure 2.18. The reader may compare with trace 2 of Figure 3.6.

2.4 Transfer Matrix Model

Having now concluded the discussion of optomechanical effects arising in the canonical system, it is time to develop the mapping from our MIM system to the canonical one. The main difference between the two systems consists in our mechanically compliant part, the membrane, being sandwiched *between* the mirrors

[23] We plot all (n, m) modes for $n = 1, \dots, 14, m = 1, \dots, 14$ where only one of each $(1, 3)$-$(3, 1)$ type pair is included.

rather than displacing one of the mirrors. This introduces a few extra complications into the analysis, most noticeably that the coupling of the membrane to the light field depends on the membrane's position relatively to the intracavity standing wave.

In order to analyse this situation we turn to the transfer matrix model. This section is based on the work presented in [Jayich et al., 2008] and [Wilson, 2012, chapter 3]. The idea is to simply track the circling intra-cavity fields to obtain all the parameters of the total cavity. This approach approximates all fields by infinite plane waves, an approximation we justify by noting that the Rayleigh range of our cavity mode is roughly ten times the distance from the end mirror to the membrane.

The starting point of the analysis is the situation illustrated in Figure 2.19, where we diagrammatically show the seven fields of interest.

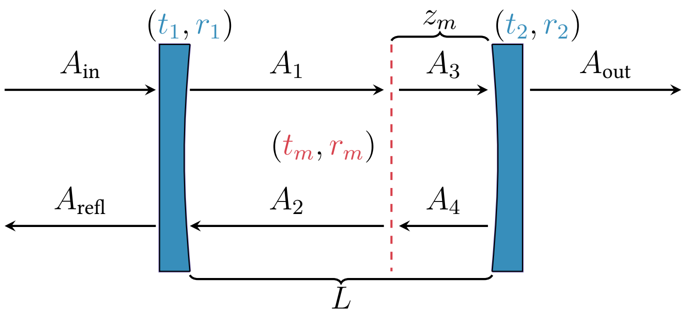

Figure 2.19: Overview of the six field amplitudes to be determined from the nine (including wavenumber) input parameters.

Evidently, the field amplitudes obey the following set of equations:

$$A_1 = \mathrm{i}t_1 A_{\text{in}} + r_m A_2 \, \mathrm{e}^{\mathrm{i}kL - z_m}, \tag{2.185}$$

$$A_2 = r_m A_1 \, \mathrm{e}^{\mathrm{i}k(L-z_m)} + \mathrm{i}t_m A_4 \, \mathrm{e}^{\mathrm{i}kz_m}, \tag{2.186}$$

$$A_3 = \mathrm{i}t_m A_1 \, \mathrm{e}^{\mathrm{i}k(L-z_m)} + r_m A_4 \, \mathrm{e}^{\mathrm{i}kz_m}, \tag{2.187}$$

$$A_4 = r_2 A_3 \, \mathrm{e}^{\mathrm{i}kz_m}, \tag{2.188}$$

$$A_{\text{refl}} = \mathrm{i}t_2 A_2 \, \mathrm{e}^{\mathrm{i}k(L-z_m)} + r_1 A_{\text{in}}, \tag{2.189}$$

$$A_{\text{tran}} = \mathrm{i}t_2 A_3 \, \mathrm{e}^{\mathrm{i}kz_m}, \tag{2.190}$$

where r_m and t_m are the amplitude reflection respectively transmission coefficients of the membrane. To calculate these, one treats the membrane as thin dielectric plate to obtain that

$$r_m = \frac{(n^2-1)\sin(knd)}{2in\cos(knd)+(n^2+1)\sin(knd)}, \tag{2.191}$$

$$t_m = \frac{2n}{2in\cos(knd)+(n^2+1)\sin(knd)}, \tag{2.192}$$

where d is the membrane thickness and n is the index of refraction of the membrane. For our Si_3N_4 membranes, at a wavelength of roughly 800 nm and a stress of 1.1 GPa, this is has a value of 2.0 [Philipp, 1973], [Campillo and Hsu, 2002]. The imaginary part of the refractive index, corresponding to light absorption in the membrane, has been found to be immeasurably small. From a measurement of the finesse of our cavity before and after the insertion of a membrane, we obtain $\mathcal{F}_{\text{cavity}} = 130\times10^3 \pm 7\times10^3$ and $\mathcal{F}_{\text{MIM}} = 125\times10^3 \pm 5\times10^3$, respectively, meaning that within the uncertainties, the two finesses are the same. Using the mean values from the finesse measurements and knowledge about the mirror reflectivities (see section 3.5), we may place an upper bound for the optical losses of the membrane of 4 ppm. Denoting this loss as $\mathcal{L}$, it then holds (for small losses) that

$$1-\mathcal{L} = \mathrm{e}^{2\,\mathrm{Im}(n)kd} \approx 1 + 2\,\mathrm{Im}(n)kd. \tag{2.193}$$

For $2\pi/k = 837$ nm and $d = 50$ nm, one obtains that $\mathrm{Im}(n) \approx 5\times10^{-6}$.

It is worth noting, at this point, that the membrane thickness is an important experimental parameter in the pursuit of the highest possible coupling, as a higher membrane reflectivity obviously yields more imparted light momentum. In Figure 2.20 we illustrate the periodic dependence of $|r_m|$ on the membrane thickness. The optimal working point turns out to be at a thickness of ≈ 65 nm, rather than at 100 nm, since also the membrane mass increases with the thickness, which in turn will decrease the zero-point fluctuations and thus the coupling achieved.

Returning from this small digression, we may solve the system of equations (2.185)-(2.190) for the A_i ($i = 1,2,3,4$) by setting the input field, A_{in}, to be 1. This yields somewhat lengthy expressions, that are, however, easily evaluated numerically. From the intra-cavity fields, we can then build all quantities of interest.

Although the A_i ($i = 1,2,3,4$), given fixed input parameters $\{t_1,\, r_1,\, t_2,\, r_2,\, n,\, d,\, L,\, z_m\}$, can be calculated for all values of k, it is of course most relevant to assert what happens on resonance. To find the resonances, we simply demand that the two fields A_{in} and A_{refl} be π out of phase with each other, which for our transmission/reflection phase convention[24] corresponds to having $\arg(A_2) = 0$.

[24]See [Siegman, 1986, section 11.1].

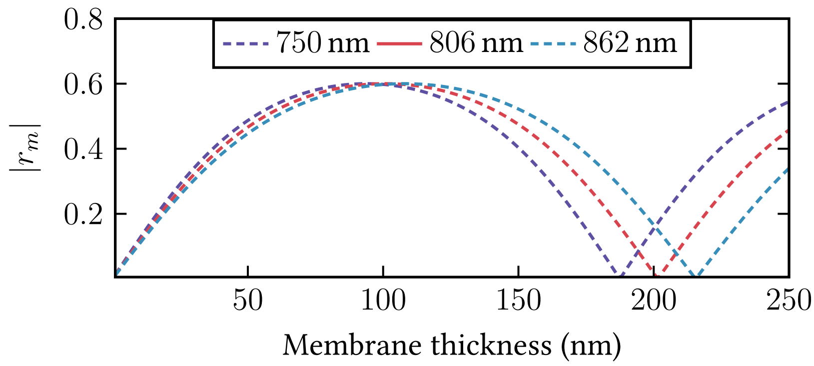

Figure 2.20: A plot of equation (2.191). Note the very weak wavelength dependence.

Before calculating the quantities of interest, we address the question of periodicity. As already mentioned, the main difference between such a dispersively coupled system and the canonical end mirror coupled system is that not all cavity resonances have the same optical properties; it all depends on the relative position of the membrane in the intra-cavity standing light wave. For our particular system, the *monolithic* cavity design does not allow us to vary the membrane position, so the expected periodicity with membrane position is more conveniently cast as a periodic behaviour in light wavenumber, k. To do so, we note that the *relative* position of membrane to standing wave is unaffected by changing the wavenumber as $k \to k + \Delta k$, where $\Delta k = L/z_m k_0$, and k_0 is the fundamental cavity resonance; $k_0 = \pi/L$. In order words, the period in k, T_k, fulfils that $T_k = \pi/z_m$. To lend from normal sinusoidal intuition, it has become customary in our group to work with $2k$ rather than k, since then everything is $2kz_m$-periodic with period 2π. On an intuitive level, we can understand this period as the membrane moving through one "bubble" of light field, as sketched in Figure 2.21.

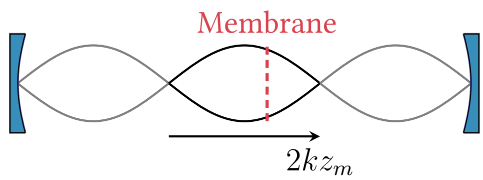

Figure 2.21: An intuitive sketch.

This intuition may also be cast into formulas. From [Jayich et al., 2008] and [Wilson, 2012, chapter 3], in the limit of a closed, lossless cavity with low mem-

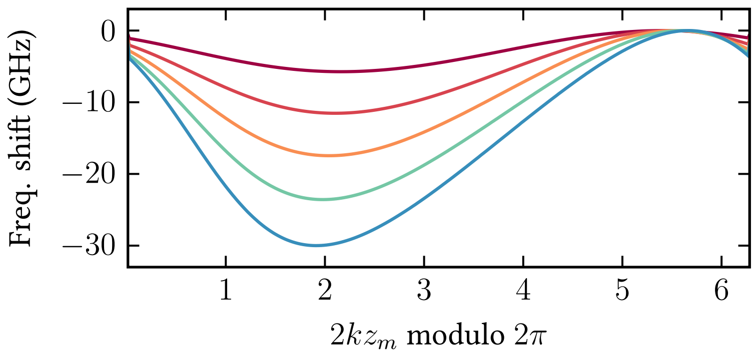

Figure 2.22: Frequency shifts folded back into 2π for membrane reflectivities $|r_m| = \{0.1, 0.2, 0.3, 0.4, 0.5\}$ (burgundy, red, orange, turquois, blue). The bare FSR is 90 GHz.

brane reflectivity, the following formula holds for the resonance wavenumber, k_{res}:

$$|r_m|\cos(2k_{\text{res}}\Delta z) = \cos(k_{\text{res}}L + \phi), \tag{2.194}$$

where $\Delta z = z_m - L/2$ and $\phi = \arg(r_m)$. By neglecting the constant phase, approximating the k_{res} on the left hand side by the "bare" cavity resonance wavenumber $k_{0,n}$ ($k_{0,n} = nk_0 = n\pi/L$, $n \in \mathbb{N}$) and adding an extra term of $k_{0,n}$ to account for multiple resonances, we obtain

$$k_{\text{res}} = \frac{1}{L}\arccos(|r_m|\cos(2k_{0,n}\Delta z)) + k_{0,n}, \tag{2.195a}$$

$$\approx \frac{1}{L}|r_m|\sin(2k_{0,n}z_m) + k_{0,n}, \tag{2.195b}$$

which is easily interpreted as the membrane causing periodic frequency shifts of the cavity resonance. In Figure 2.22 we let $k_{0,n}$ be a continuous variable and plot the resulting frequency shifts of equation (2.195) *folded back* into a single "bubble" (in the sense of Figure 2.21), that is $\frac{1}{L}|r_m|\sin(2k_{0,n}z_m)$ versus $\operatorname{mod}(2k_{\text{res}}z_m, 2\pi)$. In spite of the many approximations made, the behaviour of the full model is nicely captured.

This is as far as we go analytically. Turning now to solving the model numerically to understand our system, we plot a number key quantities in Figure 2.23. Here we go through them one-by-one to explain how they are built from the A_i ($i = 1, 2, 3, 4$).

The frequency shift. As the membrane has an index of refraction larger than air (and vacuum), its presence can only *increase* the optical path length of the cavity, and therefore *decrease* the cavity's resonance frequencies. As this decrease, for membrane thicknesses relevant here, is never more than one free spectral range of the cavity, it makes sense to identify to each cavity resonance, f_{res}, a "bare cavity" resonance, f^0_{res}, and calculate the shift in frequency induced by the membrane. This is most elegantly done by assigning the shift, Δ_f, as

$$\Delta_f = f^0_{\text{res}} - f_{\text{res}} = \text{mod}(f_{\text{res}}, c/2L). \tag{2.196}$$

Note that the two positions in $2kz_m$ that yield maximal or minimal shift of frequency correspond to the membrane being at respectively a field anti-node or node.

The output power ratios. These are simply the reflected and transmitted power ratios for the cavity as a whole, and are given by

$$T_{\text{cav}} = \frac{|A_{\text{tran}}|^2}{|A_{\text{in}}|^2}, \tag{2.197}$$

$$R_{\text{cav}} = \frac{|A_{\text{refl}}|^2}{|A_{\text{in}}|^2}. \tag{2.198}$$

Shown in Figure 2.23 are also the "bare cavity" values, given by (equation (1.5)),

$$T_0 = \frac{4|t_1|^2|t_2|^2}{(|t_1|^2 + |t_2|^2)^2}, \tag{2.199}$$

and $R_0 = 1 - T_0$.

The cavity coupling parameter. The degree of overcoupling (or undercoupling) of the cavity is the ratio between how much light leaves the cavity through the output port and how much light leaves in total. In the MIM picture, this ratio is given not only by the mirror transmissivities, but also by the different amounts of light in each subcavity. Specifically,

$$\eta_c = \frac{|t_2|^2|A_3|^2}{|t_2|^2|A_3|^2 + |t_1|^2|A_2|^2}. \tag{2.200}$$

The cavity linewidth. A simple formula for the cavity linewidth in this model is not known to us. Instead, we numerically calculate the FWHM of the cavity resonance by varying k around each resonance. Shown in Figure 2.23 is also the bare cavity linewidth, calculated as

$$\frac{\kappa_0}{2\pi} = \frac{\text{FSR}}{\mathcal{F}}, \quad \mathcal{F} = \frac{2\pi}{|t_1|^2 + |t_2|^2}. \tag{2.201}$$

The clean fact that the membrane modulates the cavity linewidth, can, however, be expressed in simple formulae. For a membrane-less cavity, the linewidth is given by $\kappa_0 = (|t_1|^2 + |t_2|^2)/\tau$, where $\tau = 2L/c$. As the membrane enters the picture, we have two subcavities for which the linewidths are

$$\kappa_1 = \frac{c|t_1|^2}{2(L - z_m)}, \quad \kappa_2 = \frac{c|t_2|^2}{2z_m}. \tag{2.202}$$

The resulting MIM linewidth will be a convex combination of κ_1 and κ_2, and the non-trivial part consists in determining exactly which combination. In [Wilson et al., 2009] a comprehensive data set exploring this linewidth modulation is presented[25].

The optomechanical coupling rate. As opposed to the canonical optomechanical system, where all photons contribute to the radiation pressure force, we now have pressure from both sides of the membrane, allowing for a possible cancellation of optomechanical effects. This behaviour is all contained in the optomechanical *coupling* rate. It is useful to compare to the canonical situation. There, the net radiation pressure force, F_{net}, fulfils that

$$F_{\text{net}} = \frac{2\hbar k \bar{n}_{\text{cav}}}{\tau_c} = \hbar G \bar{n}_{\text{cav}}, \tag{2.203}$$

where τ_c is the cavity round-trip time; $\tau_c = 2L/c$. In our case, we *define* G such that the right hand side stays the same, whilst the net force is obviously the difference between the radiation pressure from the left and right subcavity, i.e.

$$F_{\text{net}} = F_1 - F_2 = 2\hbar k \left(\frac{\bar{n}_1}{\tau_1} - \frac{\bar{n}_2}{\tau_2} \right) = \hbar G \bar{n}_{\text{cav}}, \tag{2.204}$$

whence it follows that

$$G = 2k \frac{\bar{n}_1/\tau_1 - \bar{n}_2/\tau_2}{\bar{n}_1 + \bar{n}_2}. \tag{2.205}$$

Recast in terms of the A_i and normalised to become $g_0/2\pi$ (in Hz), we then have that

$$g_0 = \frac{2k x_{\text{ZPF}}}{2\pi} \frac{|A_1|^2 + |A_2|^2 - |A_3|^2 - |A_4|^2}{\tau_1(|A_1|^2 + |A_2|^2) + \tau_2(|A_3|^3 + |A_4|^2)}, \tag{2.206}$$

where we have used that the A_i are *fluxes*, so that $n_1 = \tau_1(|A_1|^2 + |A_2|^2)$ (and similarly for n_2).

The map thus compiled of how the cavity parameters vary with membrane position inside the cavity nicely illustrates the differences between the canonical system and our membrane-in-the-middle system. More importantly, it also

[25] The authors recast it as a finesse modulation.

provides an indispensable experimental tool for choosing the right wavelength to work with. For wavelengths around $800\,\mathrm{nm}$, the product $2kz_m$ is of order 10^4, meaning that variations of tenths of a per-mill will vastly displace mod($2kz_m$, 2π). Operationally, the strategy is therefore to record a series of subsequent cavity resonance frequencies and from their frequency shift deduce their position in $2kz_m$ and, ultimately, with which one of them it is favourable to work.

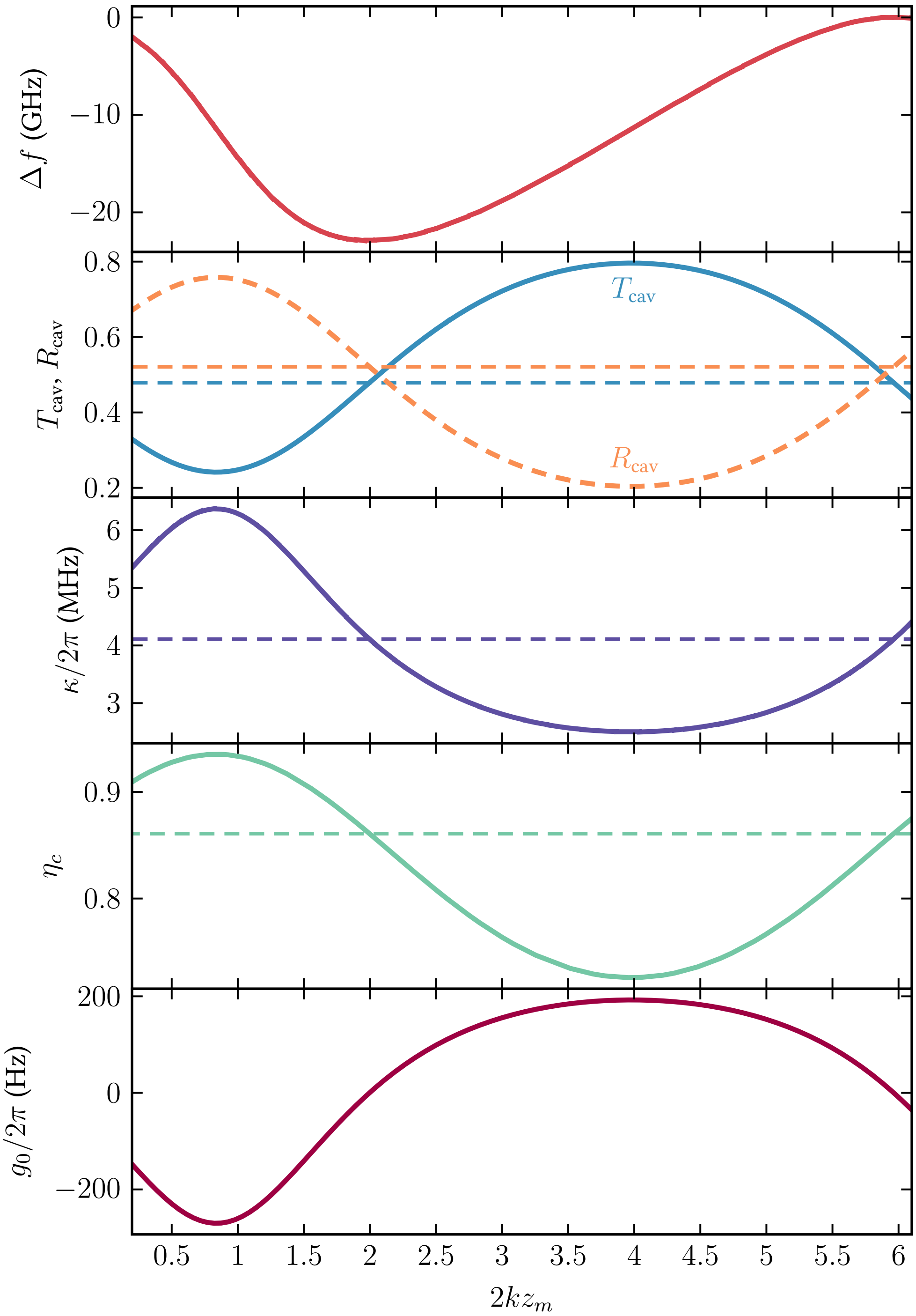

Figure 2.23: The periodic modulation of cavity parameters with k. For the three central plots, the dashed curves indicate the bare cavity values. The following set of parameters was used: $T_1 = 41$ ppm, $T_2 = 255$ ppm, $z_m = 500\,\mu$m, $L = 1.72$ mm, $d_m = 40$ nm, $\lambda_0 = 806$ nm, $m_{\text{eff}} = 2$ ng, $\omega_m = 2\pi \times 2.5$ MHz, $n = 2.0$.

Chapter 3

Experimental Realisation

We now turn to the description of the actual experiment performed. As one may imagine, the experiment underwent many incarnations before reaching the "final" form, in which it produced the results presented in the next chapter. The current chapter falls in two parts. In the first part (sections 3.1-3.4), we explain the chain of spectral data acquisition, present an overview of the setup, and discuss selected parts of it. In the second part (sections 3.5-3.8), we focus on how to reach the quantum-enabled regime. As the figure of merit hereof we take, as always, the quantum cooperativity, given by

$$C_q = \frac{4g^2}{\kappa \Gamma_m \bar{n}_{\mathrm{th}}}. \tag{3.1}$$

Four experimental parameters constitute this relation, namely κ, the cavity linewidth, g, the cavity-enhanced optomechanical coupling rate, Γ_m, the mechanical dissipation rate, and $\bar{n}_{\mathrm{th}}$, the thermal phonon occupation number, in which the membrane effective bath temperature hides. In the second part of the chapter, we go through these four parameters one by one, explaining for each of them how the setup was designed with optimisation regarding that particular parameter in mind, as well as how said parameter was measured.

3.1 Spectral Measurements

With the notable exception of the ring-down measurements presented in section 3.7, we exclusively perform measurements in the frequency domain. In fact, all we ever consider is different power spectral densities. In this section we explain the acquisition of spectra, i.e. how the displacement fluctuations of the membrane get transduced through the detection chain to ultimately become the voltage fluctuations measured by our spectrum analyser/ADC card. This chain consists of five steps shown in Figure 3.28.

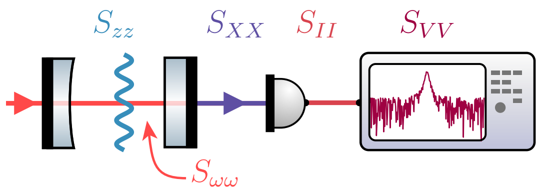

Figure 3.1: An overview of the ideal noise-less detection chain.

Displacement fluctuations of the membrane are imprinted as frequency fluctuations of the intracavity field. These are then transduced by the cavity into amplitude fluctuations of the outgoing light. The amplitude fluctuations are photodetected and give rise to a fluctuating photocurrent going out of the detector. Finally, an acquisition device terminal registers these as voltage fluctuations; the signal we get access to.

The different PSDs are related to one another in the following way:

$$S_{\omega\omega} = G^2 S_{zz}, \tag{3.2}$$

$$S_{XX} = G_C^2 S_{\omega\omega}, \tag{3.3}$$

$$S_{II} = G_D^2 S_{\omega\omega}, \tag{3.4}$$

$$S_{VV} = |Z|^2 S_{II}, \tag{3.5}$$

where G is the optomechanical coupling of equation (2.73) ($G = \partial\omega_{\text{cav}}/\partial z_m$), G_C is the cavity transduction factor, depending on frequency, cavity linewidth and detuning, G_D is the detector gain, in general a frequency dependent quantity, and Z is the input impedance of the acquisition device. This only holds true, of course, in the absence of other noise sources. In this ideal situation, our spectrum analyser will show a scaled version of $S_{zz}(\omega)$ and nothing else.

Painfully evident to any experimental physicist, there is an abundance of unwanted signals creeping into the detection, and we should somehow account for those. Here, we focus on four understood sources of noise and dismiss everything else as "electronic noise". The four noise sources are shown in Figure 3.2.

Three of the four noise sources have to do with the laser. The light going into the cavity might have classical amplitude noise and/or classical phase noise, and will with certainty have quantum noise (shot noise). That is, the input noise PSDs S_{XX}^{in} and S_{YY}^{in} consist of a classical and a quantum part. We may hope to eliminate

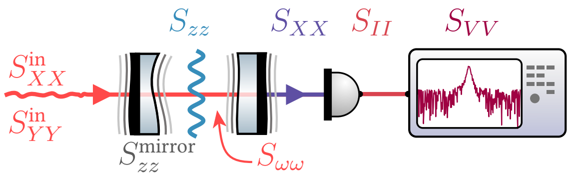

Figure 3.2: An overview of the realistic noisy detection chain.

the classical part, which we discuss more in section 3.3.1. The mirrors of the cavity are responsible for the fourth noise source in terms of their thermal motion, which imparts fluctuating length changes to the cavity. The subject of understanding and classifying all sources of mirror noise (from the coating, from the bulk, etc.) is covered in e.g. [Harry and Bodiya, 2012] (see in particular chapter 3), but will not be pursued here. Instead, we lump all thermomechanical noise from the mirrors as well as all other acoustic sources[1] together as "mirror noise". Given some transduction coefficients, α_i, the noises then show up in the intra-cavity field as

$$S_{\omega\omega} = G^2 S_{zz} + \alpha_1 S^{\text{mirror}}_{zz} + \alpha_2 S^{\text{in}}_{XX} + \alpha_3 S^{\text{in}}_{YY}. \tag{3.6}$$

The transduction coefficients are frequency dependent functions of cavity parameters such as cavity linewidth and detuning, and even contain optomechanical interaction effects. A detailed account can be found in [Wilson, 2012]. To our ends, it will not be necessary to understand the details of noise transduction much deeper than what is encapsulated in the following statement: in the spectral regions of interest, the only significant contributions to $S_{\omega\omega}$ must be from light shot noise and membrane displacements.

Meeting this noise criterion is no easy feat, and a very considerable amount of this work went into achieving that. The verification that the goal has in fact been reached, is, however, rather straightforward, as we shall see in section 3.3.

3.1.1 Calibration of the Spectrum

To calibrate the measured S_{VV} in terms of frequency fluctuations of the cavity, $S_{\omega\omega}$, a calibration tone of known modulation depth is applied to the incoming laser light. This calibration procedure is well-established and described in [Gorodetsky et al., 2010] and [Wilson, 2012, chapter 8]. Here, we give a somewhat more succinct explanation of how to understand the calibration procedure.

[1]Since any shaking of the cavity is only relevant/problematic to the extent that it displaces the two mirrors relative to one another.

The incoming (monochromatic) laser light receives a phase modulation from an EOM, which may be described as

$$|s_{\text{in}}|\,\mathrm{e}^{-\mathrm{i}\omega_L t} \to |s_{\text{in}}|\,\mathrm{e}^{-\mathrm{i}\omega_L t + \mathrm{i}\beta\cos(\omega_{\text{mod}} t)}\,. \tag{3.7}$$

The PSD of incoming phase fluctuations is therefore

$$S^{\text{in}}_{\phi\phi}(\omega) = \delta(\omega - \omega_{\text{mod}})\beta^2. \tag{3.8}$$

In passing through the cavity and being detected, these fluctuations get transduced by a frequency dependent factor $G_{\phi,I}(\omega)$, such that

$$S_{II}(\omega) = |G_{\phi,I}(\omega)|^2 S^{\text{in}}_{\phi\phi}(\omega), \tag{3.9}$$

or, similarly,

$$S_{VV}(\omega) = |G_{\phi,V}(\omega)|^2 S^{\text{in}}_{\phi\phi}(\omega), \tag{3.10}$$

where $|G_{\phi,V}(\omega)|^2 = |G_{\phi,I}(\omega)|^2 R^2$. Usually, we want to calibrate the measured spectrum into frequency fluctuations (Hz^2/Hz) and therefore invoke the relation

$$S_{\phi\phi}(\omega) = \frac{1}{\omega^2} S_{\omega\omega}(\omega) = \frac{1}{f^2} S_{ff}(\omega), \tag{3.11}$$

to obtain the transduction factor $G_{f,V}$ between frequency and voltage fluctuations; $G_{f,V} = f G_{\phi,V}$.

In the limit of negligible extraneous noise, then, it holds that if we integrate over the measured calibration tone peak, then the spectral area, A, will be given by

$$A = \int_{\omega_{\text{mod}}-\epsilon}^{\omega_{\text{mod}}+\epsilon} S_{VV}(\omega)\frac{\mathrm{d}\omega}{2\pi} = f^2_{\text{mod}}\beta^2 |G_{f,V}(\omega_{\text{mod}})|^2, \tag{3.12}$$

where ϵ is some arbitrary range[2] including the calibration peak but excluding any other features (thereby justifying the assumption of no extra noise). Thus, the desired translation is given by

$$S_{ff}(\omega_{\text{mod}}) = \frac{f^2_{\text{mod}}\beta^2}{A} S_{VV}(\omega_{\text{mod}}). \tag{3.13}$$

All that remains now is to calibrate the β-factor in terms of a parameter directly accessible experimentally, such as a voltage sent to an EOM. To this end, it is useful

[2] Usually, $\epsilon = 100\,\text{Hz}$.

to consider the transmitted power in the sidebands created by the phase modulation. It holds for the ratio of the power in the carrier, P_c, and the power in the first-order sidebands, P_s, that [Black, 2000]

$$\frac{P_c}{P_s} = \frac{J_0^2(\beta)}{J_1^2(\beta)}, \tag{3.14}$$

where $J_n(\beta)$ are Bessel functions (of the first kind). By applying a sufficiently strong phase modulation faster than the cavity decay rate and slowly scanning the laser carrier frequency across the cavity resonance frequency whilst recording a time trace of the cavity output, we may measure the carrier and two first-order sidebands. This is shown in Figure 3.3. The power in each peak is extracted from a Lorentzian fit (the power ratio is equal to the integral ratio) and the transcendental equation (3.14) is then solved numerically to obtain β. This procedure is repeated for different RMS voltages sent to the EOM and a calibration curve relating V_{RMS} to β thus emerges. As a sanity check (factors of π matter for calibration purposes!) we may compare the inferred V_π of the EOM to the one specified by the manufacturer. From the fit, we obtain a slope of $2.12\,\mathrm{V}^{-1}$. Then[3]

$$V_\pi = \sqrt{2} \times \frac{1}{2.12\,\mathrm{V}^{-1}} \times \pi = 2.09\,\mathrm{V}, \tag{3.15}$$

in agreement with the specified V_π of "<3 V" for our EOSpace EOM.

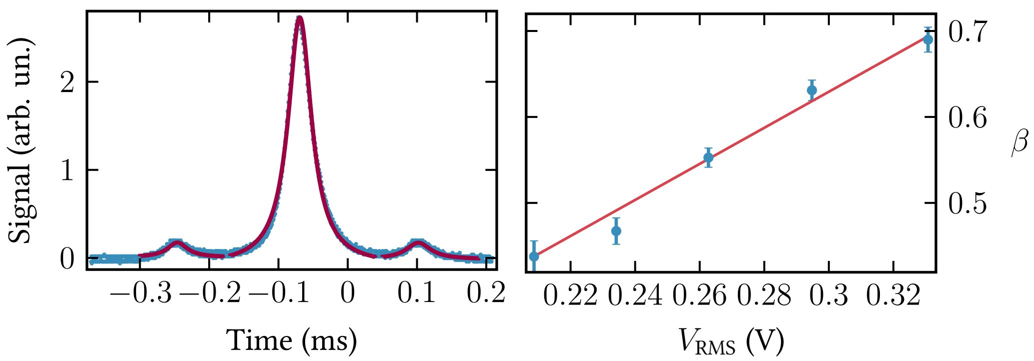

Figure 3.3: Calibration of β. Left: Measurement of sidebands with Lorentzian fits. Modulation frequency: 50 MHz. Right: fitted linear relationship between V_{RMS} and β. Error bars from statistical uncertainties ($N = 13$).

We rely heavily on this method of spectral calibration in the data analysis. It is important to stress the fact that this calibration is only valid *locally* in the spectrum.

[3] The factor of $\sqrt{2}$ translates from RMS voltage to DC voltage.

The cavity transduces frequency fluctuations differently at different Fourier frequencies, and the absolute calibration is only trustworthy when the frequency difference between f_{mod} and the frequencies considered (usually a mechanical peak) is much smaller than any other frequency scale involved (κ, Δ, ω_m). Also, the mechanics strongly modulate the cavity response, as testified by the OMIT calculations of section 2.3.7. Whenever a calibrated spectrum is used to quantitatively calculate a value, as in section 3.8.1.2 for calibrating the effective membrane bath temperature, great care is taken to properly position the calibration peak.

3.2 Overview of the Setup

Over the years, the optical setup grew and shrank organically as new ideas were tested and dismissed or sometimes retained. What we present here is a sort of snapshot of the state of affairs during the months of acquiring the data presented in the next chapter. A grand overview schematic is shown in Figure 3.4.

The current section is divided into two parts. The first, inevitable somewhat *staccato* in form, lists and briefly discusses the central components in the setup. The second part touches upon some heavily used experimental procedures underlying most all of the data acquisition to be presented.

3.2.1 List of Equipment

3.2.1.1 Lasers

The two lasers on the table are MSquared Ti:Sapph lasers, models PSX and SRX, respectively. In section 3.3.1 we characterise their noise properties. As we shall discuss further in section 3.4, the cavity length is not a tunable parameter, meaning that locking of the laser frequency to the cavity resonance must proceed by feedback to the laser. Also, any other manipulation of the relative laser-cavity frequency goes through this channel.

Passive stability of the laser resonance frequency is ensured via an in-system etalon lock. This locking mechanism also allows for tuning the lasers via external inputs. Both lasers have a slow and fast feedback input. The slow feedback input is connected to a long stroke piezo moving a mirror in the laser cavity, providing a maximal tuning range of $25\,\mathrm{GHz}$ with a sensitivity cut-off at $50\,\mathrm{Hz}$. This range is about a quarter of a cavity FSR (roughly $88\,\mathrm{GHz}$), and suffices to make scans for sideband-calibrated cavity linewidth measurements similar to those shown in Figure 3.3. Furthermore, when used in the locking loop, the slow input may be

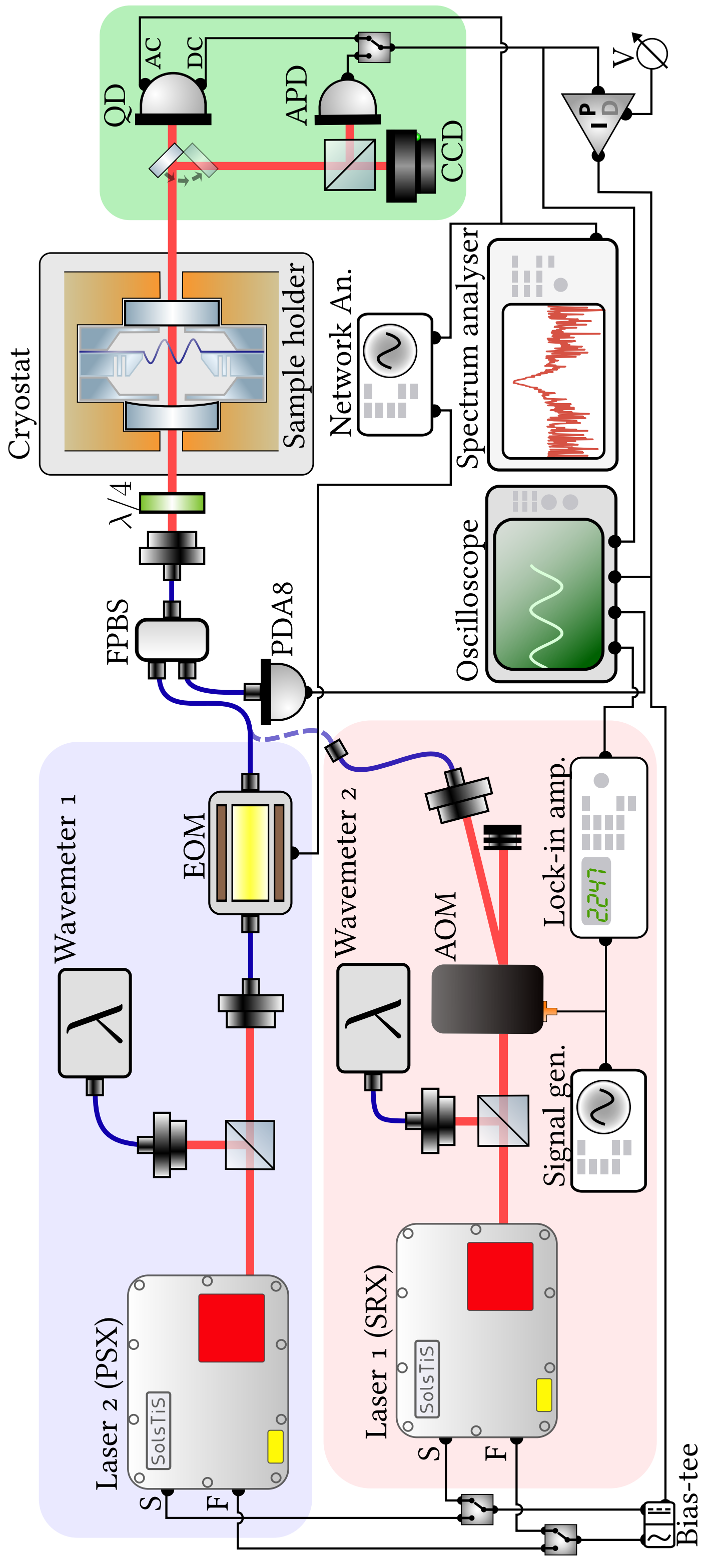

Figure 3.4: Overview of the setup. Several functional "islands" are marked with coloured boxes. Blue: The science/measurement arm. Red: The ring-down arm. Green: The detection and diagnostic island.

used to cancel drift of the cavity resonance frequency. The fast feedback input is connected to a faster piezo moving a different mirror in the laser cavity, providing a tuning range of 80 MHz with a flat response up to 30 kHz and a -5.3 dB sensitivity drop at 100 kHz. This is fast enough to target the most prominent acoustical noise in the experiment and at the same time much too slow to affect the mechanical signals in the MHz range.

The coarse tuning range of both lasers is remarkably large. With etalon lock stability and output power level somewhat compromised at the ends of the interval, the laser wavelength may be varied from 725 nm to 910 nm. This large tuning range via the wavelength-dependent transmissivities of the mirrors provides a much-needed means of tuning the optical parameters of the cavity. In subsequent sections of this chapter we explore this further.

Both laser beams are split and sent to a wavemeter. A precise monitoring of the wavelength is imperative to distinguish the $2kz_m$-value of each cavity resonance. The details of how this is done is described in section 3.5.1, but the procedure hinges on knowing the cavity resonance wavelength better than a few percent of the FSR expressed in metres. A quick conversion formula from frequency change to wavelength change near a base wavelength λ_0 is:

$$\Delta\lambda \approx \frac{\lambda_0^2}{c}\Delta f. \tag{3.16}$$

For our possible wavelength range, the FSR of 88 GHz expressed in metres thus varies from ≈ 180 pm to ≈ 240 pm. The SolsTis SRX light is sent to a Bristol 521 wavemeter with a specified precision of 5 pm. Using a stable laser input and statistical analysis, we have found a precision of 1 pm to be attainable. The SolsTis PSX is sent to a High-Finesse Ångstrom WS/6 wavemeter which has a live display precision of 0.1 pm. Such high precision allows for accurately tracking the cavity wavelength while the laser is locked to the cavity, useful for gauging the e.g. thermalisation times of the cavity. In section 3.8.1.1 we use this precision to justify a *lack* of cavity expansion as the temperature is varied in a certain region.

3.2.1.2 Data Acquisition

The spectral data acquisition proceeds in one of two ways. In Figure 3.4 we only show a spectrum analyser, but in reality we most often use an ADC card in a PC. We use an Adlink PCI-9846H 16-bit 40 MHz ADC card with 512 MB buffer memory. Typically we acquire with 10 MHz with 1 Msamples, allowing for a RBW of 10 Hz. In the schematic of Figure 3.4, the ADC card may be placed in the place of the spectrum analyser with the important addendum that the ADC card is connected to a PC to which also the CCD camera and laser control boxes (not shown in the Figure) are connected. This multitude of connections allows for ground loops, a problem revealing itself as excess noise in the spectral measurements. To check whether observed noise is really "in the light" or an electronic artefact, a spectrum analyser electrically disconnected from the rest of the setup may be used. We thus alternate our acquisition between the ACD card and a Rohde-Schwarz FSW Spectrum Analyzer, the latter being always completely electrically disconnected from the experiment (save for the signal input).

The DC level of the detector is constantly monitored on an oscilloscope (Agilent MSO-X 3054A 8-bit). Along with any spectral measurement the DC level from the detector, the wavelength reading from the wavemeter, and the cryostat set temperature are automatically saved.

3.2.1.3 The Detection Island

In Figure 3.4 the detection island is marked with a green box. This is where the output light is analysed. The island consists of two branches.

The first branch is mainly for diagnostics and alignment. Here a CCD camera images the transverse profile of the beam, a vital tool for choosing the right transverse cavity mode to work with. Working with any other cavity mode than the TEM_{00} significantly impedes the optomechanical coupling due to a worse transverse overlap of the light mode and the mechanical vibration pattern (see also section 3.6.1). At the same time, a Thorlabs APD-110A detects the light signal, which, due to the high sensitivity of this detector, is helpful during the initial cavity alignment phase where the transmitted signal is very weak. An important figure of merit for a photodetector is its quantum efficiency, η_d, the probability that an impinging photon is detected, i.e. converted into a photocarrier pair (for a more detailed discussion, see [Saleh and Teich, 2007, chapter 18]). In terms of the photodiode responsivity, R,

$$\eta_d = R\frac{\hbar\omega}{e} = \frac{R}{\lambda}\frac{hc}{e}, \tag{3.17}$$

where e is the fundamental charge unit and λ is the wavelength of the light. In the region near $800\,\mathrm{nm}$ our APD has $\eta_d \approx 0.81$. The APD saturates at a CW input power of $1.44\,\mu\mathrm{W}$, making it unsuitable for most of our quantum signal detection, where the large g-factors required necessitate large optical powers throughout the system.

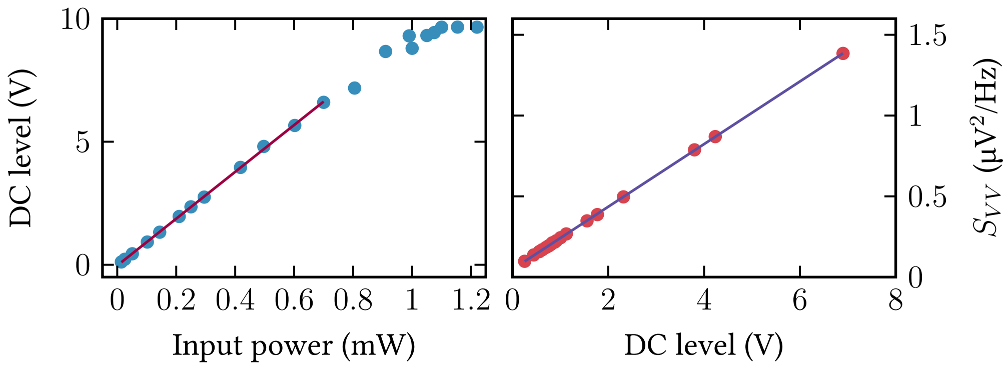

Figure 3.5: QD detector characterisation. Left: Direct DC branch response. Right: AC level. The value for S_{VV} is an average over a $3.3\,\text{kHz}$ region near $4\,\text{MHz}$. The dots are data and the straight lines are linear fits.

The second branch is the quantum measurement branch, consisting only of a home-built photodetector, from now on referred to as the QD detector, directly detecting the output light. The QD detector has a nominal quantum efficiency of 0.87. Also, the detector has separate built-in DC and AC branches with different electronic gains, a design allowing for high input light powers. In Figure 3.5 we show a characterisation of the large power range in which the QD detector responds linearly. From the combined DC and AC data we conclude that the detector has a linear response up to a CW input power of $0.7\,\text{mW}$. From the DC data, a DC gain of $9.52\,\text{V} \cdot \text{mW}^{-1}$ is derived. Using this value, the AC data fit reveals a noise level 3 dB above the electronic level when the DC output is $248\,\text{mV}$, corresponding to an input power of $26.0\,\mu\text{W}$. Comparing this to the APD CW saturation power, we find a "dead" window for output signals of powers ranging from $1.44\,\mu\text{W}$ to $26.0\,\mu\text{W}$. In section 3.5 we explain how our cavity has a tunable linewidth. The full range of achievable linewidths is not at our disposal, since the output signal from the cavity must not fall in the dead range.

3.2.1.4 The Cryostat

The cryostat is an Oxford Instruments 53309 Microstat Hi-Res Helium flow cryostat. Helium is delivered through a transfer tube inserted into an external Dewar flask. The helium is transported through the system either via a vacuum pump creating an under-pressure in the cryostat (pull mode) or by exploiting the overpressure naturally created in the Dewar flask due to evaporation (push mode). The vacuum pump is connected to the cryostat via a flow control station, using which one may reduce the effective helium pump rate. The cold finger of the cryostat can easily reach the ambient helium bath temperature of $4.2\,\mathrm{K}$ when using pull mode. The vibrations thus induced by the helium flow are, however, detrimental to the vibrational stability of the cavity. For normal experimental operation, it is necessary to carefully and gradually reduce the output flow until a feasible steady-state is found. This procedure is both time-consuming[4] and non-reproducible in the sense that hysteresis makes it unclear a priori which temperature can be reached. Typical resulting cold finger temperatures fall between $6\,\mathrm{K}$ and $9\,\mathrm{K}$. The vibrations of the pump can be circumvented by operating the cryostat in push mode. Here we are however faced with different challenges. When closing the safety valve of the Dewar flask, an over-pressure steadily builds up, leading to ever-higher helium flow rates. Eventually, the flow gets so violent that this again compromises the cavity stability. At this point, reached usually[5] around $5\,\mathrm{K}$, one must reduce the pressure, leading to an increase in temperature. In conclusion, it is not possible to maintain a stable temperature during the many hours of data acquisition. Therefore, we accept the sub-ideal cold finger temperatures offered by pull mode in order to achieve a stable temperature. Once an equilibrium has been reached, the temperature deviations are typically as small as a few tens of mK over several hours.

The cryostat is evacuated with a Pfeiffer HiCube 80 Eco pump station to a normal working pressure of $1 \times 10^{-5}\,\mathrm{mbar}$, which under cryogenic conditions drops to $2 \times 10^{-6}\,\mathrm{mbar}$. The pump station consists of a roughing pump and a turbo pump which has a maximal operational speed of $90\,000$ rpm, corresponding to a $1.5\,\mathrm{kHz}$ vibration. These vibrations completely obstruct any locking of the laser to the cavity, and must be greatly dampened for the experiment to proceed. A successful way to dampen these vibrations (and any other tube-transmitted vibrations) is to introduce an impedance mismatch along the transmission line. More concretely, we forged a shoe-box sized plastic container full of cement around a $\approx 30\,\mathrm{cm}$ segment of the vacuum tube connecting the turbo pump to the cryostat. This completely solved the problem.

[4]With some experience, one may move from room temperature to a stable cryogenic working temperature in one and a half hours.

[5]The exact vibration threshold depends on the cavity linewidth, but there seems to be a steep transition, perhaps from laminar to turbulent helium flow.

3.2.2 Operating the Experiment

3.2.2.1 Locking the Laser to the Cavity

The cavity resonates at a certain optical frequency, but this frequency is not completely stable in time. Small cavity length changes perturb the optical resonance frequency. It is instructive to make a small back-of-the-envelope estimate for how large a cavity length change is needed to change the resonance by an optical linewidth. The cavity resonance frequency is given by $\omega_{\text{cav}} = n\omega_0$, where $\omega_0 = \pi c/L$ and L is the cavity length. A small change ΔL in the cavity length will, to first order, change ω_{cav} according to

$$\omega_{\text{cav}} \to \omega_{\text{cav}} + \omega_{\text{cav}}\frac{\Delta L}{L} \quad \text{as} \quad L \to \Delta L + L. \tag{3.18}$$

Thus, for the frequency change to be κ, $\Delta L/L$ must be equal to $\kappa/\omega_{\text{cav}}$, a small number indeed. For $\omega_{\text{cav}} = 372\,\text{THz}$ (corresponding to $806\,\text{nm}$), $\kappa = 6\,\text{MHz}$ (see Figure 3.16) and $L = 1.7\,\text{mm}$, a cavity length change of $\Delta L = 0.21\,\text{nm}$ suffices. Obviously, some active stabilisation of the laser frequency is needed.

Over time, different approaches to solving the problem were tested[6], but eventually the experiment converged to a simple *transmission slope lock*, which is also the one illustrated in Figure 3.4. In such a scheme, the error signal fed back to the laser is basically (appropriately modified by a PI-circuit) the DC level from the photodetector. One selects a certain desired cavity output transmission level and the feedback loop then attempts to reach this by changing the laser frequency. This scheme clearly hinges on having good output power stability of the laser, as input power fluctuations are indiscernible from cavity or laser frequency fluctuations. Luckily, the SolsTis lasers are remarkably stable, both in terms of frequency and power, and the scheme was found to work well. The detuning can then be tuned using an input offset voltage added to the error signal (shown in the bottom right corner of Figure 3.4). The error signal itself is split into a slow part fed to the slow, long-range actuator of the laser and a fast signal fed to the fast, short-range actuator.

Note also that that there is always only a *single* beam going into the cavity. Locking, cooling, and reading is all done with the same laser beam, adding to the simplicity of the experiment. From this way of operation, a certain way of data acquisition also follows. In by far most of the cases when we perform serious measurement series (to be discussed more in chapter 4, but already section 3.2.2.2

[6] Including a PDH lock in reflection and using two different transverse cavity modes for respectively locking and cooling.

is an example hereof), we fix the laser input power to the cavity and vary the detuning knob. In this way, the intra-cavity photon number is varied along with the detuning, as the laser beam climbs closer and closer to resonance.

In chapter 2 we saw two examples of optomechanical instabilities, namely the static bistability and the parametric instability. Both of these may be encountered as the laser climbs towards zero detuning. The former is eventually reached simply because the intracavity power becomes too large. The second becomes a problem as soon at there are excursions of the relative cavity-laser frequency. These might temporarily bring the laser frequency to the blue-detuned (positive Δ) side of the optical resonance, leading to a vanishing Γ_{eff}, which in turn induces violent oscillations that bring the laser out of lock. In the face of the cavity vibrations stemming from thermal motion and in particular the helium flow, there is thus always some critical detuning closer than which it is not possible to tune the laser to the resonance.

3.2.2.2 Determining Δ and κ

A brief glance through section 2.3 will reveal that all optomechanical effects depend on κ, the cavity linewidth, and Δ, the laser detuning. Without knowing these, the experimenter is left in the dark regarding what to expect from the output. In some sense, this universal Δ-κ-dependence allows *any* measurable quantity to be used for determining these two quantities, but it is preferable to decouple the mechanical parameters from the light-cavity parameters, and thus determine Δ and κ independently of any spectral measurement. To this end, we recall from in section 2.3.7 that the weak probing of the cavity with a frequency-swept phase modulation results in a response function (see equation (2.178) and Figure 2.17), the broad features of which are given by

$$C(\omega) = -\frac{1}{2}\sqrt{\eta_c\kappa}\,\delta X \frac{\omega\kappa}{((\omega+\Delta)^2+\kappa^2/4)\sqrt{\Delta^2+\kappa^2/4}}, \tag{3.19}$$

and thus depend only on Δ and κ and an overall scale factor set by the output coupling of the mirror and the modulation magnitude.

By using the Network Analyser (see Figure 3.4) we apply a swept tone to the EOM and demodulate at the same frequency. The resulting trace is then normalised to remove the overall scaling, and the broad response function is fitted. In Figure 3.6 we show an exemplary measurement series, testifying to the credibility of this scheme.

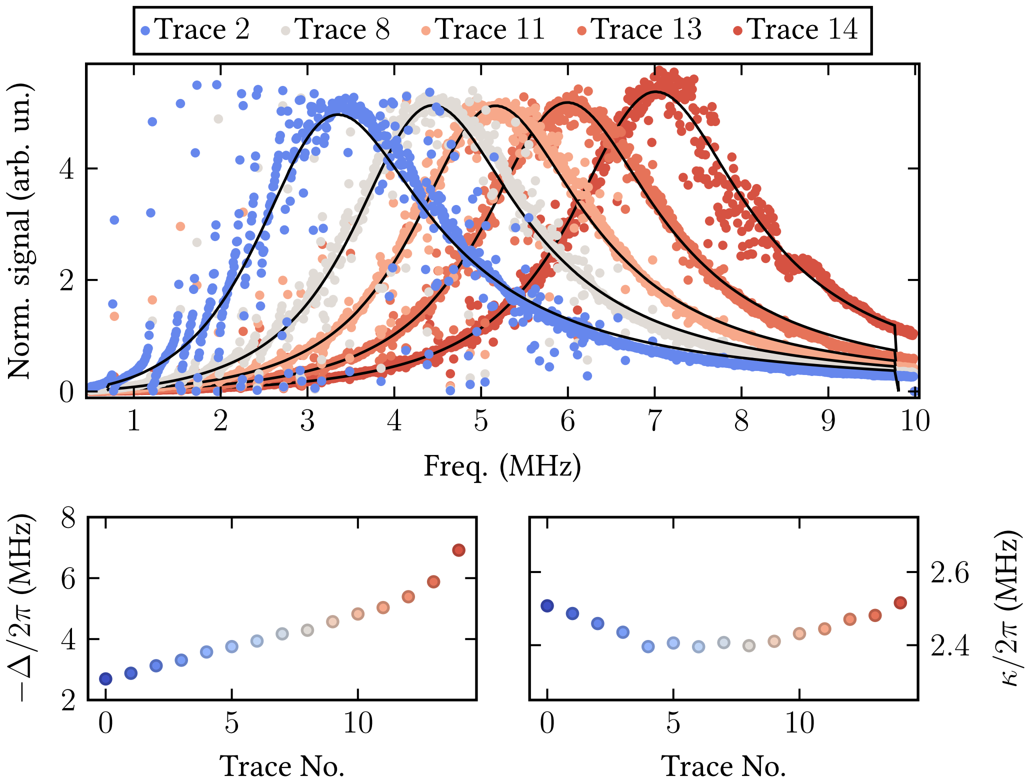

Figure 3.6: Determination of Δ and κ. Top: five selected traces out of a series of 15 traces showing excellent agreement between model and data. Bottom panels: 15 fit-extracted values of Δ and κ.

There are, however, a few caveats. What is measured is not only the cavity response, but also the mechanical contribution. As the intra-cavity power increases, this response can get quite significant. Furthermore, all mechanical modes contribute, which can heavily distort the measured signal from the bare cavity response. In the top panel of Figure 3.6, this is particularly evident in the $1\,\mathrm{MHz}$-$3\,\mathrm{MHz}$ region of trace 2, where some seven crossings of the fit line by the data is seen. These crossings are OMIT responses of different mechanical modes (see also section 2.3.7.1).

Looking at the measured linewidths, we see a small, but systematic error in the linewidth measurement. The cavity linewidth should not vary throughout the measurement series, and we conclude that the mechanical mode distortion leads to some apparent broadening of the cavity response. The effect in these data is, nonetheless, rather small; the mean linewidth is $2.44\,\mathrm{MHz}$ and the standard deviation of the measured values is $0.04\,\mathrm{MHz}$.

3.3 The Quantum Light Source

Essential to any experiment pursuing *quantum* optomechanical interactions is a light source limited by quantum noise only. From the theoretical considerations of ground state cooling and ponderomotive squeezing in sections 2.3.4.2 and 2.3.6, respectively, it is clear that any excess noise in the laser will rapidly and thoroughly deteriorate the wanted quantum signal. In the next subsection, we present measurements characterising the noise performance of our laser. The actual measurement were performed with the SolsTis PSX model, but very similar results hold for the SolsTis SRX.

Before turning to the measurements, we briefly present the schematics of the laser setup. They are shown in Figure 3.7 . The main thing to note is the presence of a pump laser pumping the Ti:Sapph laser. The noise properties of the laser system depend on the pumping power, as will be shown in the next section.

3.3.1 Noise Properties of the Laser

To determine whether a given light source is shot noise limited, the simplest approach is to take another light source, known to be shot noise limited, and compare the two. To this end, we use a household torch which, being a thermal (chaotic) light source with a very short coherence time, will, in the frequency range of interest, have intensity fluctuations dominated by shot noise (see [Loudon, 1973, chap-

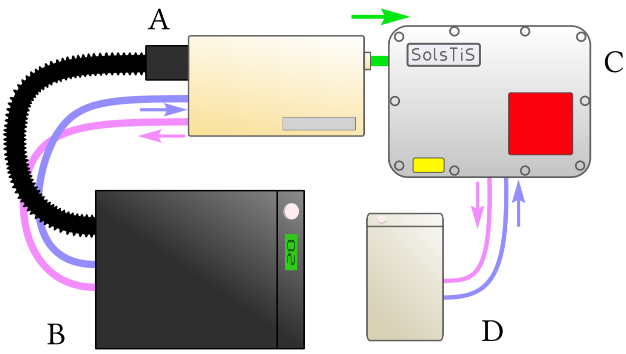

Figure 3.7: The laser setup. A: The Sprout pump laser delivering 1 W-10 W of 532 nm light to The SolsTis. B: The power supply-cooler unit delivering cooling water and pump light to the Sprout. C: The SolsTis laser. D. Cooling unit (Thermotek NanoTherm) for water cooling the Ti:Sapph crystal.

ter 5]). Furthermore, as the torch is battery-driven, we expect very little excess noise from voltage and current fluctuations.

The measurements fall in two stages. As also mentioned in section 3.1, we worry about classical amplitude and phase fluctuations. We attack the former first, in the form of intensity fluctuations.

3.3.1.1 Relative Intensity Noise

To gauge the amplitude fluctuations of the laser source, we perform a *relative intensity noise* (RIN) measurement. The optical setup is straightforward; the laser is shone directly onto a photodiode (in this case the QD detector). For different pump powers delivered to the laser, we dump different amounts of light (using a PBS and a $\lambda/2$-plate) such that a constant DC light level is maintained on the detector. We maintain a DC output of 1 V corresponding to $\sim$ 100 µW to within 5 % throughout the measurements. The resulting spectra are shown in Figure 3.8.

The large relaxation oscillations of the laser are seen at the lower frequencies, growing in height and retracting downwards in frequency as the pump power is reduced. One of the features persistently haunting the experiment is also seen: many very sharp spectral peaks, not attributable to any expected laser feature. These we classify as electronic noise, partly caused by ground loops not possible to eliminate, partly caused by unknown sources. Note, however, that most of the peaks are only a single bin wide, and that the RBW of this measurement was 100 Hz. The spectral “hair” is thus not as dense as it appears when the spectrum is

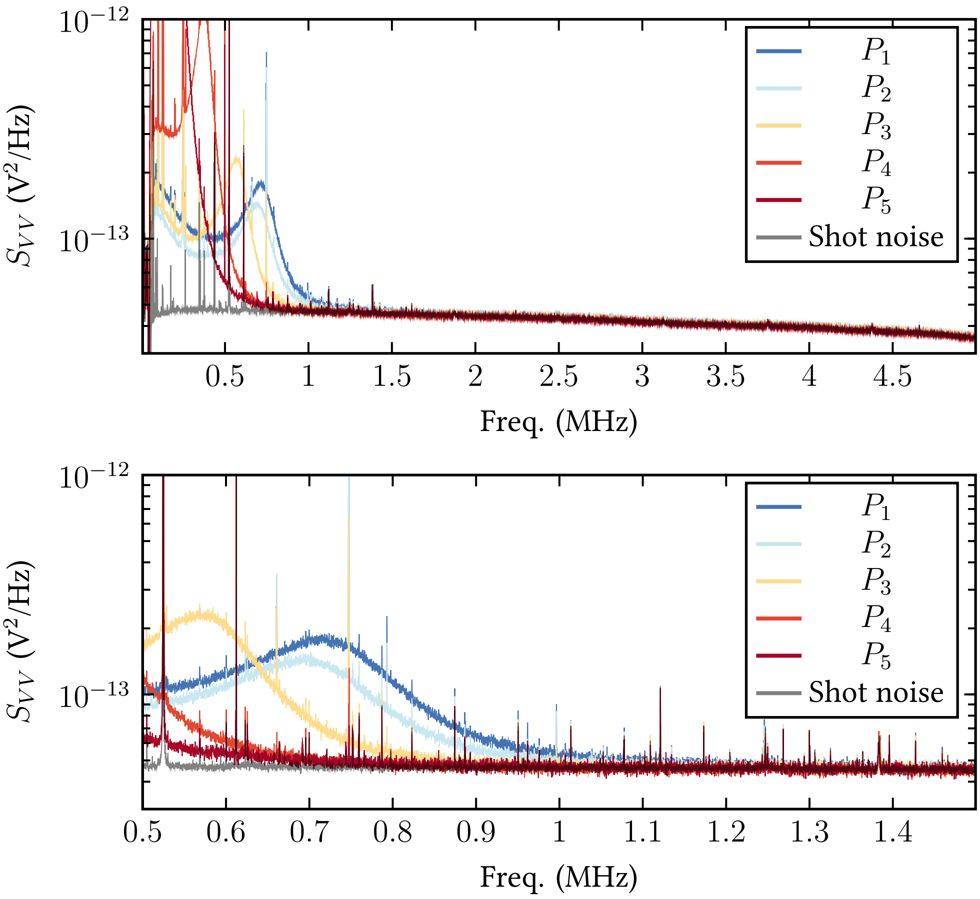

Figure 3.8: Relative intensity noise measurement. Bottom panel is a zoom of top panel. The spectra show that the laser has no excess amplitude noise for frequencies above 1 MHz when properly pumped. The pump powers are: $P_1 = 5.3\,\mathrm{W}$, $P_2 = 4.9\,\mathrm{W}$, $P_3 = 3.8\,\mathrm{W}$, $P_4 = 2.3\,\mathrm{W}$, and $P_5 = 1.6\,\mathrm{W}$.

viewed over a range so large that the pixel resolution[7] is much larger than the actual RBW. Apart from the electronic noise, the measurements show a very clearly shot noise limited spectrum. Using a pump power of 2 W, We conclude that our light source has little to no classical amplitude noise above 1 MHz.

3.3.1.2 Phase Noise

Phase noise is somewhat more difficult to extract as one must first transduce phase fluctuations into photo-detectable amplitude fluctuations, whereby noise is potentially added by the transductive element. Thus, it can in principle be difficult to distinguish a noisy transducer from a noisy laser. The cleanest way to perform a phase noise measurement would plausibly be by beating two laser beams of similar frequencies against each other. Save for a large slow beat note at the frequency difference, classical phase noise would show directly, except for the very unlikely event of the two lasers having common classical phase noise of equal magnitude. With two lasers on the optical table, this measurement begs to be performed, but has not been realised yet.

Instead, we let our optical cavity transduce both amplitude and phase fluctuations of the laser. By referencing measured data traces to independent shot noise measurements, it will always be possible to ascertain the background noise level relative to shot noise. If this coincides with the shot noise level, it is a valid conclusion that no additional noise, be it in phase or amplitude, is present. In section 3.4.4 we also give a quantitative bound for the PSD of frequency fluctuations of the laser derived from measurements of the thermal mirror motion.

3.4 The Sample Holder

Rivalled only by the phononic bandgap chip (to be discussed in section 3.7.1), the sample holder is the most vital part of the experiment. Once the experiment has settled on a certain sample holder design approach, one is stuck with it and must try to push through and overcome any setbacks introduced by following that particular path. In this work, we chose the minimalist *monolithic cavity* design approach[8], born out of the experimental philosophy that *passive* stability is preferable to *active* stabilisation, and that any positional degree of freedom in the cavity is a backdoor for unwanted noise to enter the system.

[7]Or, when viewed on printed paper, the ink dot resolution.

[8]We gratefully acknowledge Dr. D. Wilson as the originator of this idea.

In addition to this, a shorter cavity implies a large optomechanical cooperativity. For a given set of mirror transmissivities, the cavity finesse, $\mathcal{F}$, is fixed. Then, assuming also a fixed (to within one cavity FSR) working wavelength of the laser, the optomechanical coupling scales according to

$$g = x_{\mathrm{ZPF}}|\alpha|^2 \frac{\omega_{\mathrm{cav}}}{L} \propto \frac{1}{L}. \tag{3.20}$$

The cavity linewidth fulfils that

$$\kappa = 2\pi \frac{c}{2L\mathcal{F}} \propto \frac{1}{L}, \tag{3.21}$$

meaning that the cooperativity goes as $1/L$, indeed implying that the cavity should be as short as possible. For sideband cooling the membrane, it is also preferable to be able to work in the resolved sideband regime. The minimal tolerable cavity length is therefore set by the mechanical frequency of the membrane modes and the transmissivities of the mirrors. Using state-of-the-art mirrors with transmissivities of, say, $T = 25$ ppm (the actual values of our mirrors are discussed in section 3.5), and taking the membrane mode frequency to be $2\,\mathrm{MHz}$, we get $\kappa = 2\omega_m$ for a cavity length of roughly $1.25\,\mathrm{mm}$. This therefore sets the length scale we aim for with our design; a few-mm long cavity.

In keeping with the minimalist philosophy and the short cavity length desire, the cavity is made as compact and stable as possible by pressing the cavity mirrors directly against the membrane chip. Or rather, as doing so would compromise the bandgap and not allow the membrane to freely oscillate out of plane (see section 3.7.1 for details on the membrane chip geometry), against a small stack of silicon chips. Such a design leaves *no* tunable degrees of freedom other than the laser wavelength once the cavity has been assembled.

In Figure 3.9 we show a sketch, not too far from the actual realisation, of our monolithic membrane-in-the-middle cavity. The main idea is to ensure thermalisation and stability by embedding the cavity in a bulky slap of copper which is firmly bolted to the cold finger of the cryostat.

The rest of this section is structured as follows: in section 3.4.1 we go over some of the many considerations regarding the sample holder design, both justifying the concept of a short, compact cavity and illustrating some of the design challenges imposed by different experimental demands. In section 3.4.2 a detailed overview of actual sample holders is given, and sections 3.4.3 and 3.4.4 deal with two aspects of the critical *alignment* procedure of the cavity.

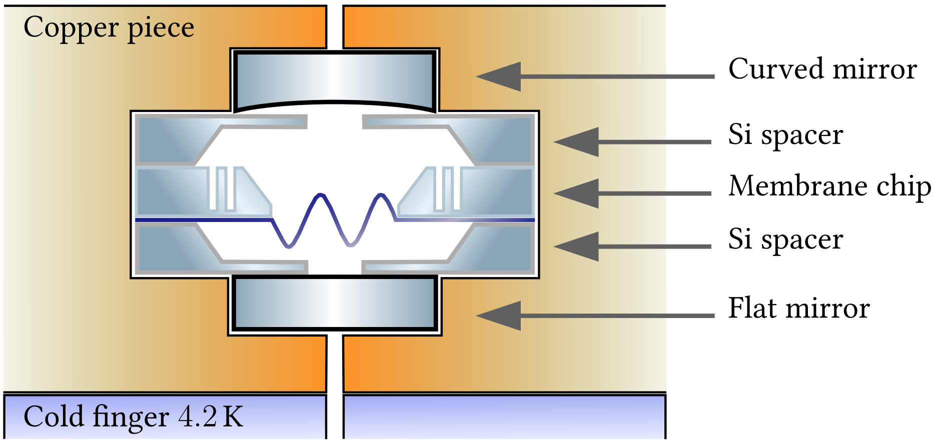

Figure 3.9: The monolithic cavity approach: the minimal set of necessary components for building a cryogenic MIM system. The vertical grooves in the membrane chip represent the phononic structure. Lengths not to scale.

3.4.1 Sample Holder Design Criteria

Although simply described as a minimalist idea, the actual cavity physically present on our optical table was the result of a long iterative design process. Here we illuminate the design process and some of the choices made.

As already explained, two main elements were required for the experiment to be succesful; a high mechanical quality factor and a low temperature. In principle, this is trivially accomplished: one simply leaves the membrane floating in a zero-kelvin vacuum. In practice, these two demands rather contradict one another. A high mechanical quality factor is severely compromised by the clamping losses introduced by nearly any fixation of the membrane. A low temperature, on the other hand, is impossible to achieve unless the membrane frame is very tightly pressed against a massive cold object. Furthermore, as alignment of the membrane to the flat bottom mirror is crucial if there is to be a cavity at all, the membrane frame should ideally be pressed against this mirror as well. These three mechanical requisites, all equally important, seem to impose different constraints on the setup. The former constraint is resolved by the aid of the phononic bandgap shielded membranes, to be discussed in section 3.7.1. The latter two are in more direct conflict; how can the membrane chip (or rather: the spacer-chip-spacer sandwich) be pressed simultaneously against the cold copper and the flat mirror? The solution pursued in this experiment was to press the silicon chips hard down against the copper by sample holder construction (see next section) and then, using a spring, press the flat mirror up against the silicon. We can not resist remarking that this way, our system *genuinely* realises the canonical mirror-on-a-spring setup, albeit for different reasons.

3.4.2 Sample Holder Implementations

Yet another design criterion is the ease with which the sample holder may be assembled and in particular aligned. Although thermalisation is best ensured with a single-piece sample holder, such a design is not geometrically possible; there must be at least two pieces. Furthermore, an intermediate assembly step is needed, both to ensure parallelity between membrane and flat mirror (the subject of the next section) and to allow for an independent positioning of the curved mirror in the plane transverse to beam propagation (the subject of section 3.6.2). Therefore, the minimal number of sample holder pieces is three. As the membranes' phononic chips evolved from 1D phononic crystals to 2D phononic crystals, the sample holder also evolved. The overall design nonetheless remained the same. The two-step evolution is shown in Figures 3.10 and 3.11. The main differences between the two designs consist in a downwards extension of the bottom part ensuring a large contact surface to the cold finger, a widening of the sample-accommodating groove (B), and the addition of steering rod holes (5).

In the next two subsections, we discuss two main experimental challenges relating mainly to the assembly of the bottom part and middle part of the sample holder, namely the tilt of the sample and the clamping conditions for the mirrors. The top part is covered in more detail in section 3.6.2.

3.4.3 Membrane Tilt

The screws labelled 2a-2d in Figures 3.10 and 3.11 are providing the downwards force clamping the spacer-membrane-spacer stack against the bottom part and balancing the upwards force from the spring on which the bottom mirror rests. There is no way of ensuring that all four screws are screwed in exactly equally far, and the middle part of the sample holder may therefore be tilted with respect to the plane defined by the bottom part of the sample holder, the plane to which the propagating beam is a normal. This tilt is inherited by the membrane, causing different parts of the membrane to be at different distances to the bottom mirror. Such misalignment might lead to optical losses[9] via scattering of light off of the membrane

[9]To the best of our knowledge, a solid modelling of the effects of tilt in a MIM system has not been published. Results on the effect of tilt on polarization degeneracy of the cavity modes may be found in [Kalinkevich, 1978].

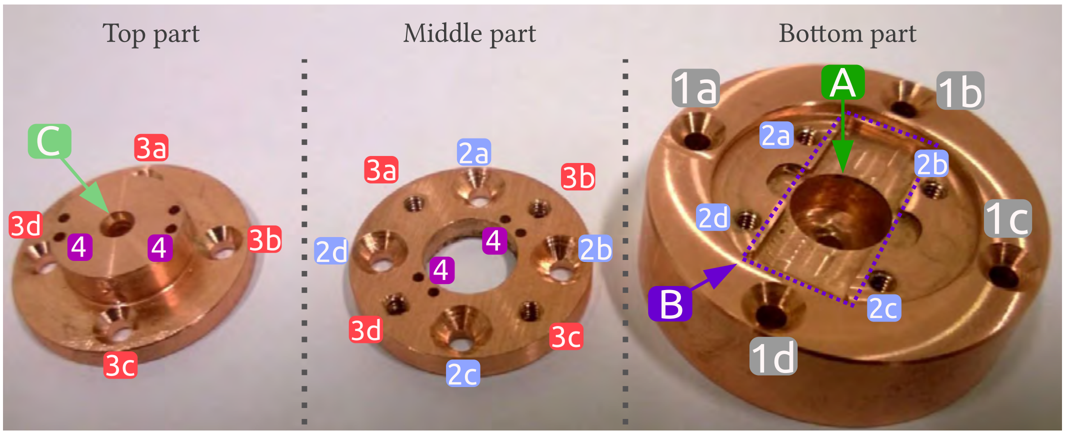

Figure 3.10: The 1D Phononic Crystal Chip Sample Holder. Legend: **A**: The central hole into which a spring and the flat mirror is inserted. **B**: The groove accommodating the phononic crystal chips. **C**: the optical access hole. **1a-1d**: Screw holes connecting the bottom part to the cryostat cold finger. **2a-2d**: Screw holes connecting the middle part to the bottom part. **3a-3d**: Screw holes connecting the top part to the middle part. **4**: Holes allowing for evacuation.

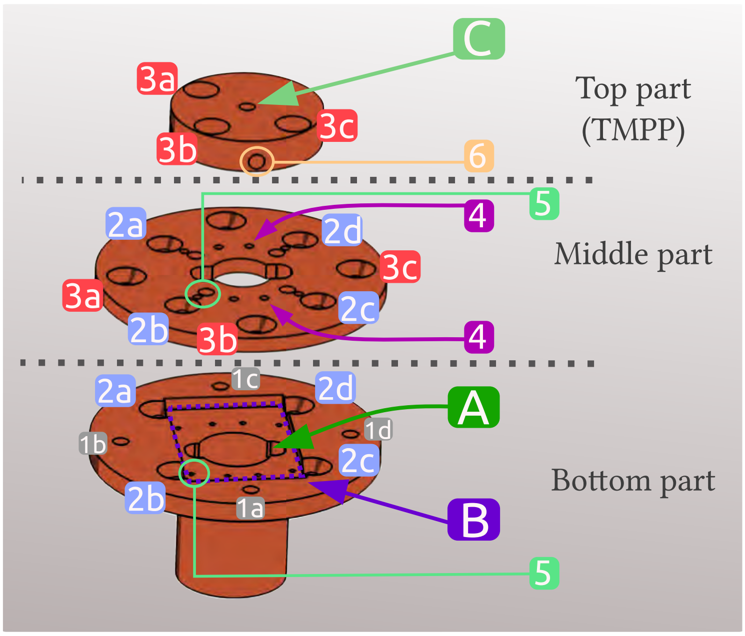

Figure 3.11: The 2D Phononic Crystal Chip Sample Holder. The legend is identical to that of the 1D holder. Additionally: **5**: Holes for steering rods. **6**: Micro screw hole.

into other longitudinal cavity modes than the TEM_{00} normally used. During the assembly phase, the tilt may be observed by illuminating the membrane with a wide light source (e.g. the laser widened through a lens) and looking at the image in the CCD camera. There, the membrane tilt shows as interference fringes, which may then be aligned away by systematically tightening and loosening the four screws in question. In Figure 3.12 such an alignment operation is illustrated.

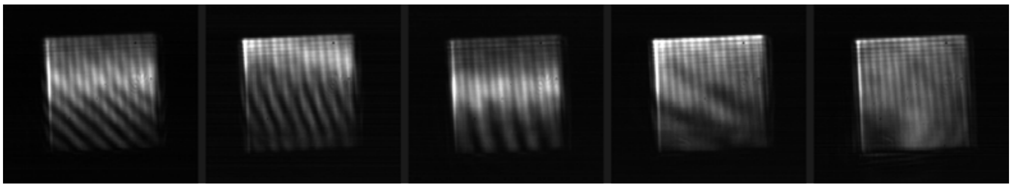

Figure 3.12: Carefully aligning the tilt away. Time progresses from left to right.

What persists in the images as a checker-patterned grid of non-uniform illumination is believed to be due to diffraction off the membrane edges and therefore irrelevant to the narrow illumination normally used. The best alignment we have been able to achieve left approximately one fringe in each direction across the membrane. This is unlikely to lead to relevant optical losses, but, as we shall see in section 3.6.2 it somewhat complicates positioning the laser spot on the membrane.

Although the initial alignment of the cavity is thus possible to accurately make tilt-free, there is no guarantee that the cryogenic cooling of the sample holder will not change that original alignment. The membrane tilt remains somewhat of an unknown variable, and might be responsible for the extra optical losses sometimes observed in the experiment.

3.4.4 Springs and Mirror Noise

For an experiment as obsessed with vibrational stability as ours, it might at first seem rather suicidal to introduce trembling elements such as springs into the sample holder. Clearly, a loose spring will leave the entire cavity length oscillating at the loaded spring's resonance frequency, a highly unwanted behaviour. A large effort was put into investigating different springs and their resulting stability. The general trend indicates that short springs with as large contact surfaces as possible are preferable. This rules out disk springs and springs with more than a single coil and leaves ring springs as our best candidates.

The mirrors themselves are not directly touching the springs, but are held in small copper cups (see Figure 3.18. The bottom mirror has a similar cup). The effect of the spring on the cavity stability aside, the effect on the quality factor of the mirror modes is remarkable. In the large overview plot of Figure 3.13 we show the calibrated output spectrum of an empty cavity for four different assemblies. Assembly 1 is the 1D sample holder using disk springs. Assembly 2 and 3 are for the 2D sample holder using disk springs but an additional spacer is inserted in assembly 3 to further compress the springs. Finally, in assembly 4 ring springs are being used along with improved, slightly thicker spacers. The difference is striking. Whereas the first three assemblies yield similar "mountainous" landscapes of broad noise, assembly 4 shows clearly defined high-Q mirror modes.

When considering the effect of thermal mirror noise, it is important to first note that the noise levels of the mirrors used in our setup are indeed of relevance to the experiment. Secondly, as the spectral area of each peak is determined by the temperature, and the area is (roughly) the width times the height of each peak, the ideal situation is to have high-Q mirror modes, concentrating the noise in a few very well-defined spectral regions with wide deep valleys between them, rather than having a smeared-out spectrum with a high baseline.

In Figure 3.14 we show the mirror noise of assembly 4 at cryogenic temperature. As expected from basic thermo-mechanical considerations, the noise level experiences a suppression of order ~ 50, the ratio between room temperature and our cryogenic working temperature. The quality factors of the mirror modes are somewhat compromised, which is expected for glass [Arcizet et al., 2009], but well-defined peaks are still observed in the spectrum. Between the peaks are quiet regions of shot noise. Ascribing all peaks to mirror modes, this measurement also sets an upper bound for the intrinsic phase noise of our laser. As discussed in section 2.3.4.2, technical laser noise acts as a thermal reservoir for the mechanics and thus sets a lower bound for the occupation reachable by sideband cooling. In the resolved sideband limit, it holds that [Kippenberg et al., 2013]

$$\bar{n}_f = 2\pi\sqrt{\frac{\bar{n}_{\mathrm{th}}\Gamma_m}{g_0^2}\bar{S}_{ff}(\omega_m)}. \tag{3.22}$$

For $\bar{n}_f = 1$ to be barely reachable, this entails for a mechanical mode with realistic parameters $\omega_m = 2\pi \times 2.5\,\mathrm{MHz}$, $g_0 = 2\pi \times 120\,\mathrm{Hz}$ and $Q = 12 \times 10^6$, that $\bar{S}_{ff}(\omega_m)$ should fall below $0.132\,\mathrm{Hz}^2/\mathrm{Hz}$, a boundary only just grazed in Figure 3.14. If we however believe that the excess noise is ascribable to the mirrors, we can extrapolate from Figure 3.13 that deeper valleys exist between the peaks, where ground state cooling is possible (e.g. around $2.15\,\mathrm{MHz}$). At the same time, the mirror noise excludes certain spectral regions and thereby certain mechanical modes (for a given sample) from being targeted for serious cooling experiments.

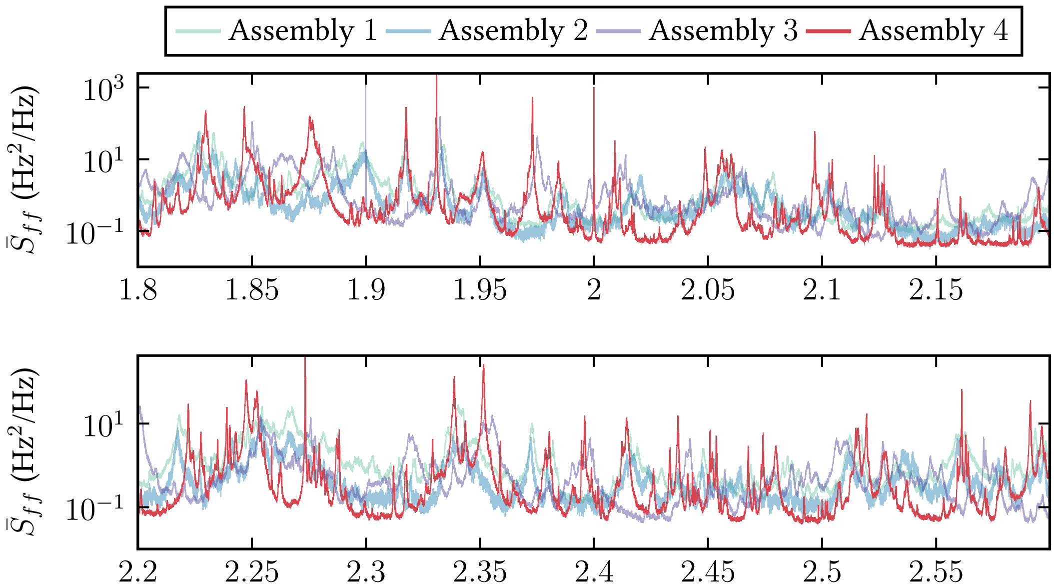

Figure 3.13: Room temperature mirror noise for different cavity assemblies. The final assembly 4 yielded significantly higher mirror mode Q factors than the previous assemblies. Calibration tone at 2 MHz for Assembly 4.

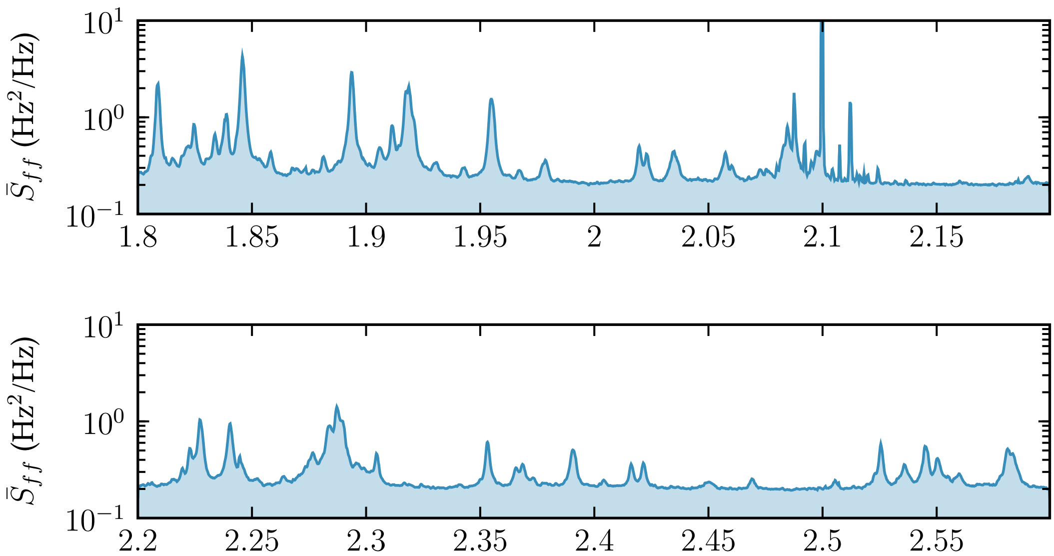

Figure 3.14: Cryogenic mirror noise for assembly 4. The cryostat set temperature was 6.5 K. Calibration tone at 2.1 MHz.

3.5 The Cavity Linewidth

The optical losses and thereby the linewidth of the cavity are determined by the transmittivities of the mirrors. As the membrane reflectivity is more or less unchanged over a remarkably large range of 100 nm (see Figure 2.20), there is nothing in the experiment determining a priori which wavelength to work with. Furthermore, as the Ti:Sapph laser is also agnostic regarding working wavelengths over a similar span, the wavelength dependence of the mirror coatings offer a convenient knob for *in situ* tuning of the cavity linewidth. The mirrors used in the cavity are highly reflective custom-made super-polished mirrors from Advanced Thin Films, supposedly[10] optimised for high reflectivity at the D2 line of Caesium. The mirror transmittivities were measured using the setup shown in Figure 3.15, where a laser beam is detected with and without the mirror and the ratio is taken to be (an upper bound for) the mirror transmittivities. To achieve the needed dynamic range of 5-6 orders of magnitude, a full amplitude modulation was applied to the laser via an AOM, and the measured signal was demodulated with a lock-in amplifier at the modulation frequency, thereby greatly improving the signal-to-noise ratio for the low-power signal.

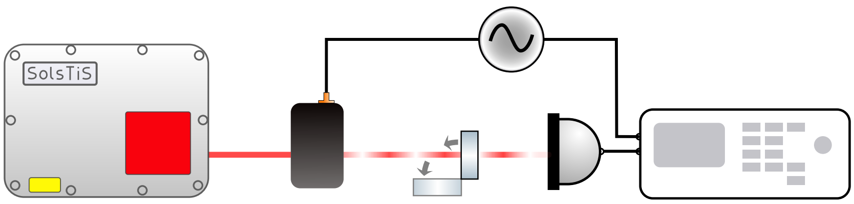

Figure 3.15: Setup for measuring highly reflective mirror transmittivities. The angles in this simplified picture are slightly wrong; in reality the first order deflected beam reaches the detector.

In Figure 3.16 we show the results of the measurement series for our (curved) incoupler mirror and (flat) outcoupler mirror. In order to extrapolate between the measured wavelengths, we fit two polynomials of order respectively 3 (incoupler) and 5 (outcoupler) to the logarithmic losses. Although one could in principle fit a more theoretically well-founded transmission curve for a Bragg mirror, not much extra information would be gained that way. From the extrapolated curves, we may then compare the expected cavity linewidth to a measurement for an empty

[10] The mirrors were purchased prior to the author joining the experiment, and all documentation was lost (or anecdotal).

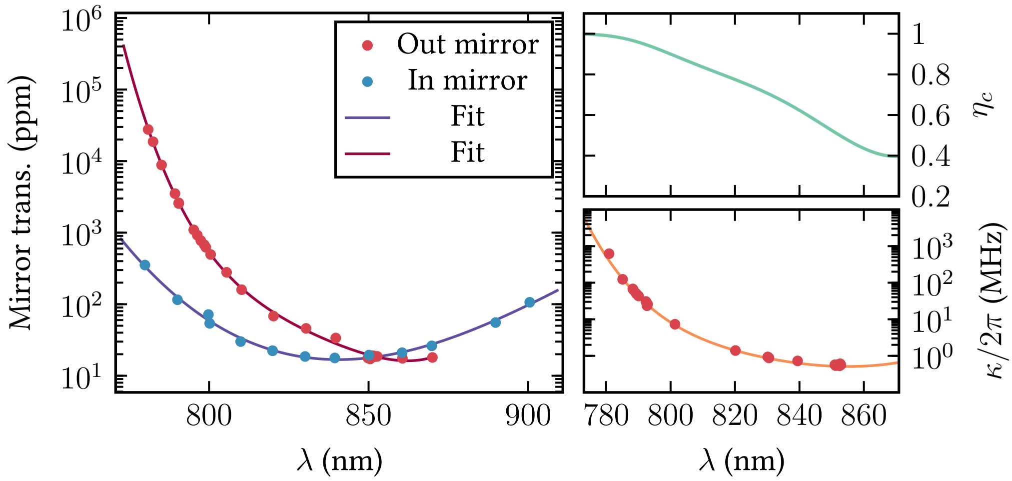

Figure 3.16: Tunable cavity properties. Left: measured mirror power transmittivities and extrapolating fits (fits explained in main text). Right: corresponding cavity coupling parameter and linewidth, the latter together with empty cavity linewidth measurements.

cavity. This is also shown in Figure 3.16. We observe no measurable added round-trip losses for the cavity, and conclude that the reflectivities of the mirrors are, to a very good approximation, indeed equal to one minus the measured transmittivities.

In conclusion, we have an optical cavity with a widely tunable degree of over-coupling and a very widely tunable cavity linewidth. The latter is very practical for quickly switching between markedly different cavity regimes, and is also necessary requirement for *in situ* measurements of the mechanical quality factor, discussed in section 3.7, where one must rule out any dynamical back-action in order to extract Γ_m.

3.5.1 Finding the Right Place in $2kz_m$

Finally, we note that the values presented in Figure 3.16 are the *bare* cavity values. Upon insertion of the membrane, both the effective cavity linewidth and over-coupling will be modulated around these values, with a modulation periodic in the input laser wavenumber as discussed in section 2.4. One important difference between the theoretical discussion and actual realisation is worth mentioning. Whereas we presented continuous curves in Figure 2.23, in the actual experiment, the full tuning range is not available, since the relative membrane position, z_m/L

is fixed once the cavity is assembled. Then only k is variable, but this is obviously not a continuous parameter, since the cavity resonance condition most be fulfilled. Upon changing the laser frequency one FSR, we move a fixed amount in $2kz_m$ given by the ratio[11] z_m/L, and for our particular parameters ($L \approx 1.7\,\text{mm}$, $z_m \approx 0.5\,\text{mm}$), $z_m/L \approx 2/7$, meaning that we keep sampling the same seven positions in $2kz_m$, unless the wavelength is changed rather drastically. Luckily, seven is in this respect a large number, and there will always be points reasonably close to the theoretical optimum. In Figure 3.17 we display an exemplary measurement series of nine consecutive TEM_{00} resonances and how they "fold back" into the relevant $2kz_m$ range. Indeed, seven distinct locations are found.

The excellent agreement with the model (discussed in section 2.4) is noteworthy. The model has no tunable degrees of freedom, but is only fed with the resonance data. First, the function of equation (2.195) is fitted to the recorded resonance wave numbers, yielding both the cavity length L, the membrane position z_m, and the membrane reflectivity r_{mem}. Next, from the average wavelength of the series, the mirror reflectivities can be looked up (see Figure 3.16). This exhausts the list of model input parameters (see Figure 2.19). Rather than just being a successful validation of a particular model, this is an invaluable experimental technique; there is no other way to ensure that we choose the right working wavelength than by making a fit like the one in Figure 3.17.

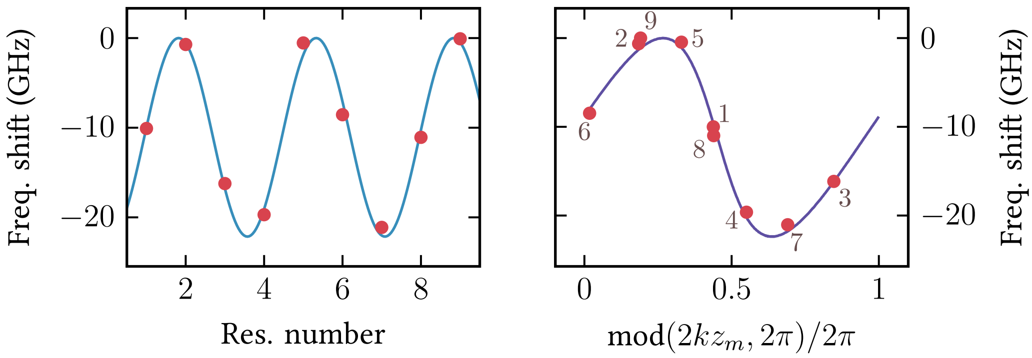

Figure 3.17: Folding of resonances. Left: consecutive resonances fitted to a function à la equation (2.195) with the linear part subtracted. Right: The same resonances, but folded back and with the model prediction for the shifts superimposed (not fitted). The resonance numbers are added as annotations.

[11]For $z_m/L = 1/2$, this amount is exactly π.

3.6 The Optomechanical Coupling

As described in chapter 2 and quantified through the cooperativities, it is of prime importance for the experiment to get "as much interaction" per photon as possible, i.e. to maximise g_0. To achieve this, we have two knobs to turn. First, we may ensure that the membrane is situated close to the optimal position in the standing wave (see section 3.5.1). This gives a general increase (or decrease) to the coupling to all mechanical modes. Second, once a mode of interest has been selected, we may optimise the *transverse* overlap of the laser beam and the mechanical mode shape.

3.6.1 The Transverse Overlap

As our laser beam does not only illuminate a single point on the membrane, the one-dimensional description of membrane motion used throughout chapter 2 is not exactly what is measured in the experiment. The correction is, however, rather straightforward. As the membrane oscillates inside the intracavity standing wave, it imparts a phase shift to the light, a phase shift proportional to the membrane displacement. Different points on the membrane displace with different amplitudes and phases (see Figure 2.2), and the light averages over all these points with a weighting given by the local intensity profile of the light. Similarly to the correction from the transfer matrix model in section 2.4, this can be accounted for by applying a correction factor to G. Each optomechanical mode now has its own coupling, G_{nm}, given by[12]

$$G_{nm} = \eta_{nm} G, \tag{3.23}$$

where

$$\eta_{nm} = \int_{\mathcal{D}} \mathrm{d}x\mathrm{d}y\ \sin(nk_x x)\sin(mk_y y) I(x,y), \tag{3.24}$$

where $\mathcal{D}$ is the domain of the membrane and $I(x,y)$ is the normalised intensity profile of the laser beam. Hidden in equation (3.24) is the fact that η_{nm} is a function of x' and y', the laser spot centre position. To our ends, we exclusively work with the TEM_{00} cavity mode, in which case the integral can be computed analytically (see Appendix A) to yield (we have allowed x' and y' to lose the primes)

$$\eta_{nm}(x,y) = \exp\left[-\frac{w^2(z_m)}{8}\left(n^2k_x^2 + m^2k_y^2\right)\right]\sin(nk_x x)\sin(mk_y y), \tag{3.25}$$

[12] Similarly, we may define $g_{nm} = g\eta_{nm}$.

where w is the beam width[13] function of the cavity mode, given, as in chapter 1, by

$$w(z) = w_0\sqrt{\frac{z^2}{z_R^2} + 1}, \tag{3.26}$$

with the standard definition

$$z_R = \frac{\pi w_0^2}{\lambda}, \tag{3.27}$$

and w_0 being the beam width at the waist ($z = 0$), which for our cavity is at the flat mirror. In section 3.6.2 we discuss how to actually position the laser beam, but let us for the time being assume perfect position, i.e. directly at a mechanical mode anti-node. Even then, the overlap factor puts a rapidly decaying limit to the achievable optomechanical coupling as the mode number grows, much more severe for high-order modes than the semi-linear scaling of g_0. We recall that[14]

$$g_0 = x_{\text{ZPF}} G \propto \frac{1}{\sqrt{n^2 + m^2}}, \tag{3.28}$$

whereas η_{nm} is exponentially decaying in n and m. Of course, the mode numbers for which this second penalty begins to play a role hinges on the membrane dimensions and the tightness of optical focusing. In Table 3.1, a range of optimal overlaps are presented, assuming reasonable experimental parameters. Note that these are generally *not* simultaneously achievable, e.g. optimally coupling to the (1, 1)-mode entails zero coupling to the (2, 2)-mode et cetera.

The upshot is an important lesson for designing the experiment: the higher the mode numbers, the lower the cooperativity.

3.6.2 Achieving a Good Transverse Overlap

As the monolithic cavity design pursued in this work does not encompass any positional degrees of freedom, the good transverse overlap must be achieved upon assembly. In other words, it is necessary to assemble the cavity such that the optical mode has its focus at the desired (x, y)-point, meaning that the top (curved) mirror must be reproducibly positionable with good accuracy. We achieve this by the custom-made sample holder top part shown in Figure 3.18. Three micro-metre screws and a leaf spring allow for accurate and reversible positioning of the central

[13]We follow the convention of [Milonni and Eberly, 1988, chapter 14] where the intensity of the beam falls of according to $I(x, y) \propto \exp(2(x^2 + y^2)/w^2(z))$.

[14]For simplicity here we take $L_x = L_y$.

	η_{nm}						
$m\backslash n$	1	2	3	4	5	6	7
1	0.99	0.97	0.94	0.90	0.85	0.79	0.73
2	-	0.95	0.92	0.88	0.83	0.77	0.71
3	-	-	0.89	0.85	0.80	0.75	0.69
4	-	-	-	0.81	0.77	0.72	0.66
5	-	-	-	-	0.73	0.68	0.62
6	-	-	-	-	-	0.63	0.58
7	-	-	-	-	-	-	0.53

Table 3.1: The *optimal position* value of η_{nm} for different mechanical mode numbers. Parameters used: $L_x = L_y = 500\,\mu\text{m}$, $w_0 = 36\,\mu\text{m}$.

cup into which the top mirror is placed. The screw behind the leaf spring is for locking the position. Not shown is a disc spring between the cup and the bulk top part, ensuring tight clamping along the beam propagation axis.

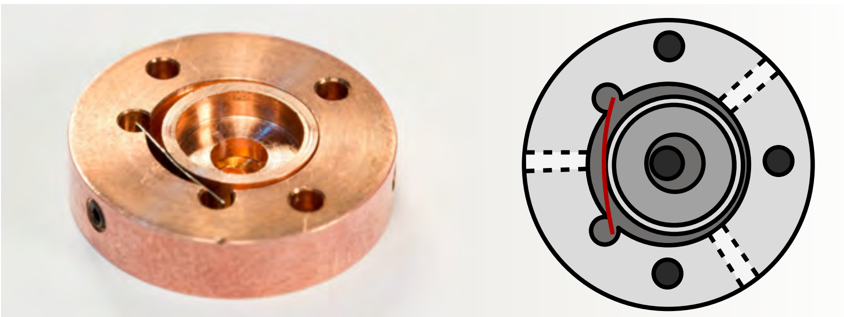

Figure 3.18: Top Mirror Precision Positioner (TMPP). Left: Photograph. Right: sketch displaying the three micro-metre screw holes (dashed white channels). The laser beam propagates up (left) or out of the page (right).

The mirror positioning protocol then proceeds as follows. First, the cavity is assembled with no top mirror.

Second, by maximising the reflection of the incoming beam off of the flat mirror and back into the incoupler fibre, using a high-reflectivity wavelength (see Figure 3.16), parallelity of the plane of translation of the incoupler head and the membrane plane can be established. The micro-metre screws of the incoupler head then allows for fine-grained[15] positioning.

[15]The smallest division of the screws (Line Tool Inc.) is $10\,\mu\text{m}$.

Third, the cryostat is evacuated to an intermediate vacuum level (typically 1×10^{-3} mbar) ensuring that all mechanical modes have low Q-factors (see equation (3.44)) and therefore short coherence times, allowing for a rapid measurement of the mechanical peak height. The cavity formed between the membrane and the flat mirror offers, although having a linewidth of hundreds of MHz, sufficient interferometric precision when illuminated at ≈ 745 nm to resolve the membrane motion and can therefore be used to map out the spatial dependence of the η_{nm} factors by comparison of different mechanical peak sizes in the corresponding spectrum. It holds for a general mechanical mode, (n, m), that it has nodal lines in the set S_{nl} given by

$$\begin{aligned} S_{\text{nl}} = \{&(x, m_y L_y/m) \cup (n_x L_x/n, y) | \\ &n_x \in \{1, \ldots, n\}, m_y \in \{1, \ldots, m\}, x \in [0, L_x], y \in [0, L_y]\} \,, \end{aligned} \tag{3.29}$$

whereas its antinodal points reside in the set S_{ap} given by

$$S_{\text{ap}} = \left\{ \left(L_x \frac{2n_x - 1}{2n}, L_y \frac{2n_y - 1}{2m} \right) \middle| n_x \in \{1, \ldots, n\}, m_y \in \{1, \ldots, m\} \right\} . \tag{3.30}$$

In Figure 3.19 these two sets are shown for the mechanical modes $(2, 1)$ and $(1, 3)$.

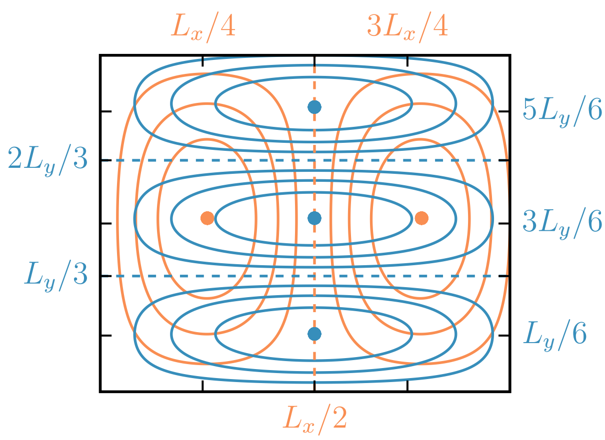

Figure 3.19: The positions of nodes (dashed lines) and anti-nodes (dots) as described by equations (3.29) and (3.30) for the modes $(2, 1)$ (orange) and $(1, 3)$ (blue). Also shown are the contours of (the absolute value of) the corresponding mode shapes.

Evidently, another mode, (n', m'), where either n' is an even multiple of n or m' is an even multiple of m (or both) will have a nodal line at every antinodal point of (n, m). As it generally holds for experimental optimisation that *minimising a* *signal is always better than maximising a signal*, this serves as a convenient guide for positioning the beam. By making an "enemy" mode disappear in the measured spectrum, we may infer that we are at the desired point (from equation (3.25) it follows that η_{nm} is zero at a mode node). In Figure 3.20 we show the simultaneously recorded spectral response of six mechanical modes from the membrane-mirror cavity. In this situation, we were aiming for the (2, 2)-mode, and thus expected a low response from the (4, 1)-mode near the optimal position.

Fourth, once the optimal (x, y) point has been established, the curved mirror is positioned using the TMPP piece (Figure 3.18) and the light reflected off of the curved mirror as a guide; once the reflected light coincides with the incoming light, the curved mirror is positioned correctly.

Finally, all screws are tightened and the cavity is then assembled. To verify that the cavity thus formed does indeed have a beam path intersecting the membrane at the coveted point, a series of OMIT measurements is performed, whereby we obtain the different g_{nm}-factors. Such a measurement series is shown in Figure 3.21. The inferred couplings are displayed in Table 3.2. Qualitatively, this looks acceptable; g_{22} is three times larger than g_{14}.

Mode (n, m)	(1, 1)	(1, 2)	(2, 2)	(1, 4)	(3, 2)	(3, 3)
g_{nm} (kHz)	102	141	116	36	67	24

Table 3.2: Couplings extracted from the OMIT fits of Figure 3.21. Measured with a cavity detuning $\Delta = 2\pi \times -2.46\,\text{MHz}$ and a linewidth $\kappa = 2\pi \times 5.38\,\text{MHz}$.

We do, however, need to form a somewhat more quantitative statement about the beam position and therefore perform a χ^2 minimisation to infer the beam position from the data. The idea is to form a vector of η_{nm} for different modes and then compare that to a vector of theoretical η_{nm}. To this end, we use either integrated peak values from the spectrum or g_{nm} values from the OMIT fits.

The integrated peak value is proportional to G_{nm}^2 with a proportionality factor, F_p, that is in general position dependent (see section 3.4.3), but not, however, dependent on mechanical mode number. In the limit of very good signal-to-noise, the transduction equations (3.2)-(3.5) can be used directly, and we may thereby obtain the following expression for the integral of a mechanical peak in the spectrum, I_{nm}:

$$I_{nm} = R^2 G_D^2 F_p G_{nm}^2 \int_{\mathcal{R}} \frac{\mathrm{d}\omega}{2\pi} S_{zz}(\omega) \approx R^2 G_D^2 F_p G_{nm}^2 \int_{-\infty}^{\infty} \frac{\mathrm{d}\omega}{2\pi} S_{zz}^{(nm)}(\omega), \tag{3.31}$$

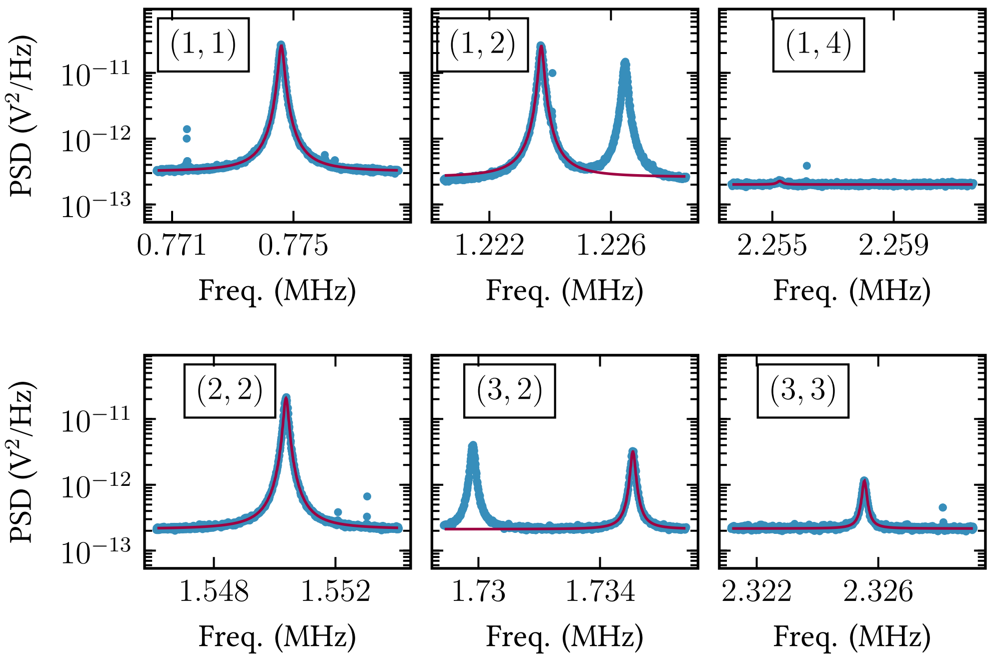

Figure 3.20: Spectral response of the membrane-mirror cavity from six mechanical modes together with Lorentzian fits for the optimal beam position when aiming for the (2, 2) mode.

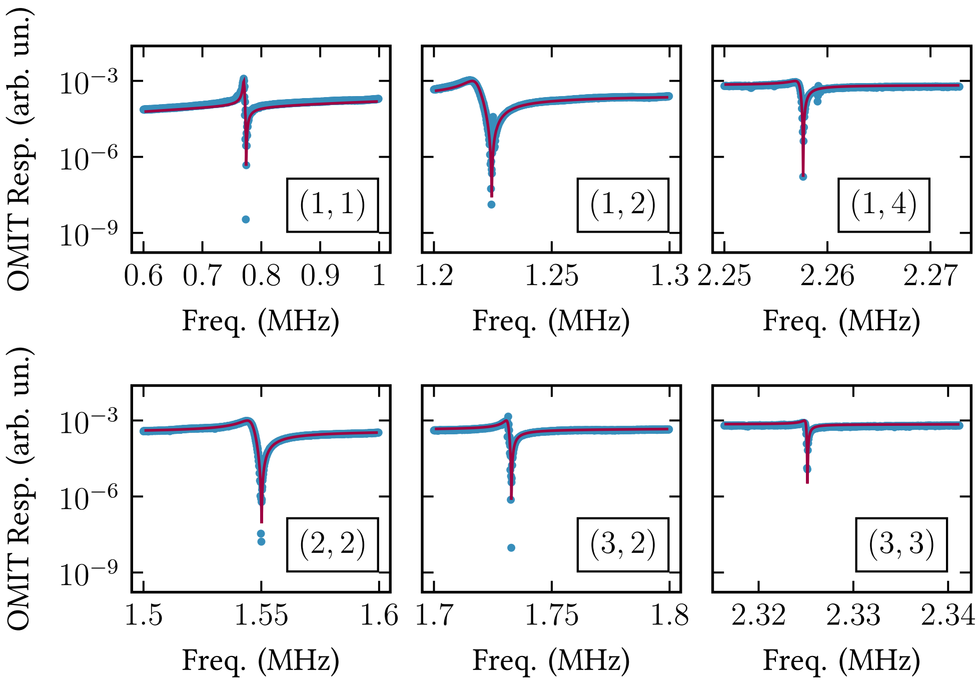

Figure 3.21: OMIT response of the fully assembled cavity attempting to reproduce the position of Figure 3.20. Extracted couplings shown in Table 3.2.

where $\mathcal{R}$ is an appropriate spectral region, $S_{zz}^{(nm)}(\omega)$ is the Lorentzian approximation of equation (2.45) to the thermally driven PSD of membrane displacement fluctuations;

$$S_{zz}^{(nm)}(\omega) = \frac{\Gamma_m k_B T}{\omega_{nm}^2 m_{\text{eff}}} \frac{1}{(\omega_{nm} - \omega)^2 + (\Gamma_m/2)^2}. \tag{3.32}$$

Here we have used the fact that we are in a poor-cavity limit with large viscous damping (high pressure, see above) to neglect effects of dynamical back-action and assume a common T and common Γ_m for all modes. This, together with equations (2.47) and (2.48), then yields the following value for the integrated spectral peak:

$$I_{nm} = G_{nm}^2 \int_{-\infty}^{\infty} S^{nm}(\omega) \frac{\mathrm{d}\omega}{2\pi} = A \frac{\eta_{nm}^2}{\omega_{nm}^2}, \tag{3.33}$$

where the constant factor A is given by

$$A = \frac{\Gamma_m k_B T}{m_{\text{eff}}} R^2 G_D^2 F_p G^2, \tag{3.34}$$

which is the same for all modes. Similarly, for the OMIT-fitted g_{nm}, we have

$$g_{nm} = B \frac{\eta_{nm}}{\sqrt{\omega_{nm}}}, \tag{3.35}$$

where the factor B is given by

$$B = \sqrt{\frac{\hbar \bar{n}_{\text{cav}}}{2 m_{\text{eff}}}}, \tag{3.36}$$

also a constant throughout the set of mechanical modes.

Following a standard recipe [Press et al., 2007, chapter 15], we perform a χ^2 minimisation to find the *most likely* beam position on the membrane, given the data. We do not specify any uncertainties in the input data, only take them to be uniform. The uncertainty is then estimated from the discrepancy between model and data alone, which turns out to give a reasonably localised estimate. The procedure is useful for finding the most likely point of laser illumination, and can in particular answer the urgent experimental question: is the curved mirror placed correctly or should it be unmounted and repositioned?

For a fixed number, N, of measured modes, we construct a unit vector $\mathbf{v}_{\text{data}}$ as

$$\mathbf{v}_{\text{data}} = \mathcal{N}[\eta_{n_1 m_1}, \eta_{n_2 m_2}, \ldots]^T, \tag{3.37}$$

by multiplying out the mode frequency dependence using either equation (3.33) or (3.35). For a given set of (x, y)-points (a grid spanning the membrane), we may then, for each point, form a unit vector with the model prediction from equation (3.25),

$$\mathbf{v}_{\text{model}}(y,x) = \mathcal{N}(x,y)[\eta_{n_1m_1}(x,y), \eta_{n_2m_2}(x,y), \ldots]^T, \tag{3.38}$$

where $\mathcal{N}(x,y)$ is the position-dependent normalisation factor. If we define an error vector, $\mathbf{e}$, as

$$\mathbf{e}(x,y) = \mathbf{v}_{\text{data}} - \mathbf{v}_{\text{model}}(x,y), \tag{3.39}$$

then the most likely position, (x_0, y_0), is the position minimising $\chi^2(x,y)$, where

$$\chi^2(x,y) = \sum_{i=1}^{N} e_i^2(x,y). \tag{3.40}$$

The estimated uncertainty is then (the number 2 is the number of model parameters, i.e. x and y)

$$\sigma^2 = \chi^2(x_0,y_0)/(N-2) \tag{3.41}$$

and finally the likelihood function of where the beam is positioned is given by

$$L(x,y) = \frac{1}{2\pi\sigma^2}\prod_{i=1}^{N}\exp\left(-\frac{e_i^2(x,y)}{2\sigma^2}\right). \tag{3.42}$$

In Figure 3.22 the two resulting position estimates using the data of Figures 3.20 and 3.21 are shown together with the aimed-for (2, 2)-mode contours. To make the localisation more precise, we also include the (4, 1)-mode as a zero value in both estimates. In the spectral data, the peak drowns in the noise and in the OMIT measurement, it is unfittably small. There is no difference in the end result between using zero and a value, say, three times smaller than that for the (1, 4)-mode. Good agreement is seen between "before" and "after", and we conclude that the TMPP piece does indeed allow us to optimise the necessary optomechanical coupling.

3.7 The Mechanical Quality Factor

As testified by the considerations in chapter 2, having a large quality factor is imperative to the experiment. Although commercially available Norcada membranes were recognised early on for their low internal mechanical dissipation [Zwickl et al., 2008], the losses they suffer in connection with being clamped, a necessity in the monolithic cavity design, render them unattractive candidates for reaching the quantum regime. The quality factor of a given mechanical mode may be written as the inverse sum of different dissipative contributions;

$$Q^{-1} = Q^{-1}_{\text{internal}} + Q^{-1}_{\text{gas}} + Q^{-1}_{\text{clamp}}, \tag{3.43}$$

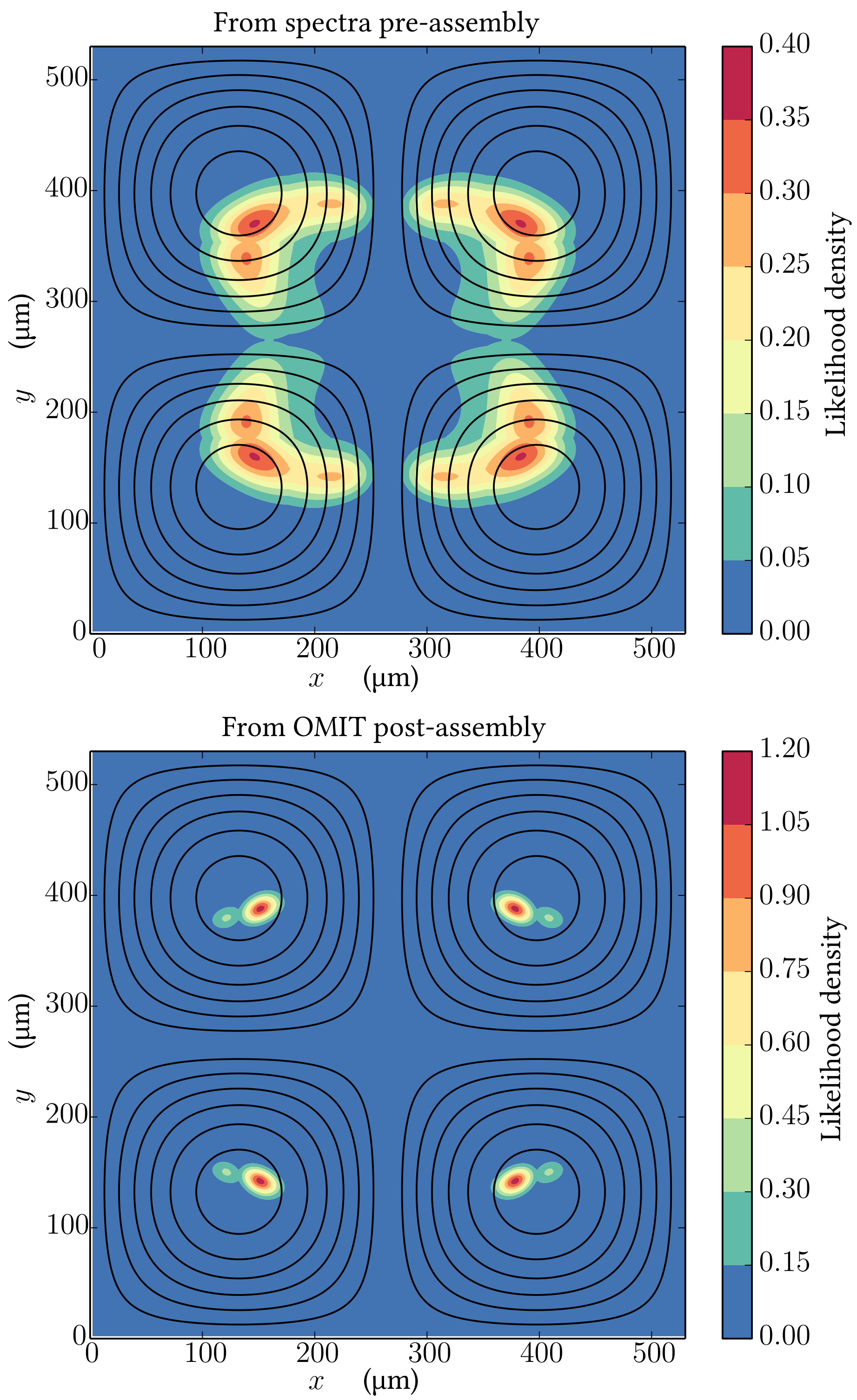

Figure 3.22: Position estimates from χ^2 minimisation. The assembled cavity localises the estimate a lot and the most likely point is conserved.

representing losses due to internal loss mechanisms, collision with surrounding air molecules, and losses due to elastic coupling to the environment.

The first term is inherently small and will be of no further concern to us. We do however mention that, owing to the mighty importance of the quality factor in optomechanics, the internal dissipation mechanisms are subject to dedicated and serious study. Recognised loss mechanism include thermo-elastic damping [Chakram et al., 2014], activation of embedded two-level defects [Faust et al., 2014], and phonon-phonon-scattering [Lifshitz, 2002]. Of less understood microscopic origin, surface losses also play an important role [Villanueva and Schmid, 2014].

The next term, given for the (n, m)-mode by [Bao et al., 2002]

$$Q_{\text{gas}} = \rho d \omega_{nm} \sqrt{\frac{\pi R T}{32 m_{\text{molar}}}} \frac{1}{p}, \tag{3.44}$$

where ρ, d, T, and ω_{nm} are defined as in chapter 2, m_{molar} is the molar mass of the surrounding gas, R is the gas constant, and p is the gas pressure, may be alleviated with proper vacuum equipment. Using the parameters of Table 2.1, a temperature of $10\,\text{K}$, and a molar mass of $29 \times 10^{-3}\,\text{kg} \cdot \text{mol}^{-1}$, even a modest vacuum level of 5×10^{-5} mbar yields a Q_{gas}-factor (for the fundamental mode) of 26 M, more than what has been experimentally realised in our group.

At last, the third term is the one that matters for samples and setups similar to ours. The clamping losses will seriously impede the experiment if one simply clamps a Norcada chip tightly as required by our sample holder design.

Therefore, it was decided to abandon the commercial samples and follow a different route, namely that of embedding a phononic structure into the chip of the membrane. This development, which has lasted several years and is still ongoing at the time of writing, was almost solely driven by Y. Tsaturyan, now a PhD-student in our group. The author of this work has not taken part in the design nor the fabrication of the samples. Here we shortly cover the theoretical aspects of the phononic bandgap, but mainly focus on the usage of these chips in the cryogenic experiment. A more elaborate discussion, including the non-trivial fabrication procedure, can be found in [Tsaturyan et al., 2014].

In Figure 3.23 we show the evolution of the membrane chips used in the optomechanical setup. Complexity develops with time if it must, and in this case it had to. The initial one-dimensional structure was found to be incompatible with our setup. The two-dimensional structure was the first chip type with which good results could be achieved. We elaborate on the difference between the two generations in the next section.

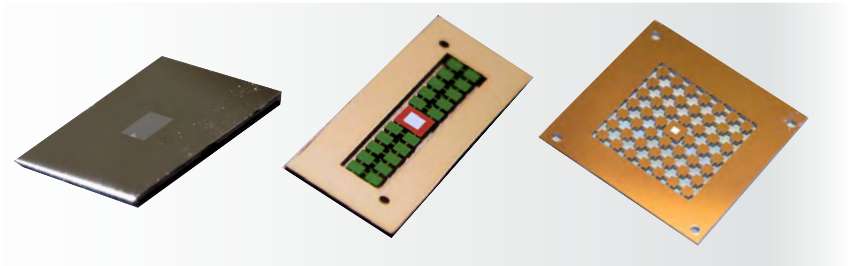

Figure 3.23: Three generations of samples. From left to right: a commercial Norcada membrane, a one-dimensional phononic structure chip, a two-dimensional phononic structure chip. The one-dimensional chip is artificially coloured to highlight the phononic structure (green) and the central defect (red) where the membrane resides. All three samples share the basic structure of a thin layer of Si_3N_4 of a Si bulk.

3.7.1 The Phononic Bandgap Chips

All foreign noise is unwanted, but some noise frequencies are more inadmissible than others. Noise at frequencies well outside the mechanical response, as given by χ_{eff}, is non-essential to the outcome of the experiment, whereas noise near the mechanics is detrimental. Rather than attempting a full-scale isolation of the mechanics from the environment, it therefore makes sense to focus the effort on a particular frequency range. The phononic bandgap offers just that. By periodically modulating a crystal structure, elastic waves with wavelengths of the same order of magnitude as the crystal structure periodicity can be suppressed from propagating [Maldovan, 2013]. For mm-structures in Si, this corresponds to the MHz range. By embedding the membrane in such a periodically patterned structure, it is thus possible to shield the mechanics from external disturbances near the mechanical frequencies. It is important to note that a continuum of "forbidden" frequencies can be realised, thus justifying the use of the term *band*gap.

To achieve a *complete* suppression of the offending modes, one strictly speaking needs an *infinite* crystal. Although we can settle for less, it holds that more unit cells of the crystal yield a better suppression. Given the circular constraint of the sample holder (cf. Figures 3.10 and 3.11) ultimately imposed by the cryostat geometry, the narrow 1D structure therefore seems like the better candidate, as this accommodates more unit cells. In Figure 3.23, the green 1D phononic structure is only attached to the surrounding frame at the short edges, thereby sporting 5 unit cells between the central "defect" hosting the membrane and the frame. Unfortunately, this long bridge-like structure has its *own* eigenmodes, the lowest of which is in the $10\,\mathrm{kHz}$-range. The vibrations of this mode induce large sidebands contaminating the cavity output spectrum. Many attempts were made to dampen these vibrations, but they all invariably compromised the bandgap. Eventually, the experiment progressed to the 2D structures, whose phononic structures have higher frequencies and much smaller vibrational amplitudes[16].

Fortunately, having three unit cells in each direction is sufficient to produce a significant bandgap. In Figure 3.24 we show a convincing measurement of the noise annihilation. The measurement was not performed in our setup, but in a separate Michelson interferometer used for sample characterisation. The lower panel shows the relative driven (a piezo was used to provide acoustic excitation) response of two different places on the membrane chip; the frame outside the phononic bandgap and the defect inside it. Over a range of almost $2\,\mathrm{MHz}$, a suppression of ~ 20 dB is seen. By proper design of the chip, the majority of the mechanical modes lies in this region. A very consistent display of high quality factors is seen throughout the bandgap, whereas most modes outside it show significantly weakened Q-factors. Furthermore, the central defect, against the modes of which the membrane is not shielded, has a very sparse spectrum of eigenmodes. In the lower panel of Figure 3.24, only 7 modes occupy the region from $1.75\,\mathrm{MHz}$ to $2.9\,\mathrm{MHz}$. As mode hybridisation between defect and membrane modes is known to also hinder high membrane Q-factors [Jöckel et al., 2011], this sparsity is another important quality of the phononic crystal chip.

In the next section, we carefully describe how the quality factor may be measured with the phononic crystal chip mounted inside the real experimental setup. Consistent agreement between the quality factors measured in that way and those measured in the diagnostic setup has been observed.

3.7.2 Measurements of Q in Our Setup

Even in the presence of a working in-chip phononic bandgap, there are still many unwanted sources of dissipation that might deteriorate the mechanical quality factors. Upon assembling the cavity, small residues of silicon may break off from the spacers or membrane chip, or copper residues from the screw holes in the sample holder may fall out. There is even a non-negligible risk that dust particles from the surrounding atmosphere may land on the membrane during cavity assembly.

[16]From finite-element simulations of the different structures, the 1D bridge has a fundamental frequency of $12.9\,\mathrm{kHz}$ and an effective mass of $5.4\,\mathrm{mg}$, whereas the 2D grid has a fundamental frequency of $36.2\,\mathrm{kHz}$ and an effective mass of $7.3\,\mathrm{mg}$. From equation (2.47), the expected displacement due to thermal excitations is then ~ 10 times lower for the 2D structure.

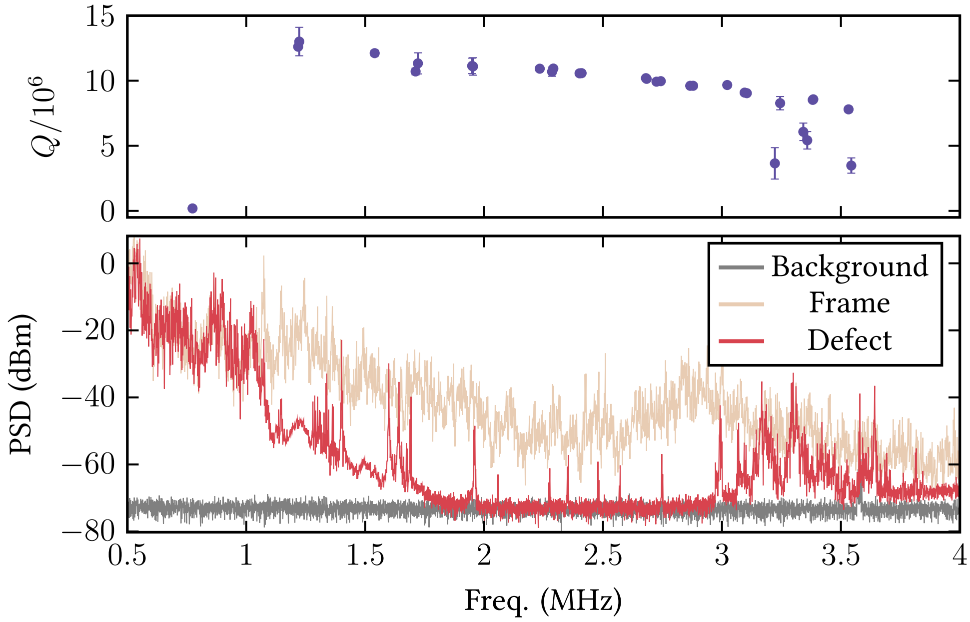

Figure 3.24: The effect of the phononic bandgap for a 2D chip. Top: Cryogenic quality factors for the first 30 mechanical modes of the membrane. Bottom: relative responses to the frame and the defect to external perturbations. The colour coding matches the 1D sample of Figure 3.23.

An example of such membrane pollution is shown in Figure 3.25. In that particular case, the identification of the problem was straightforward, but in general it can be more difficult to ascertain the condition of the membrane. Therefore, a method to measure the Q-factor *in situ* of the assembled cavity is required. Although the mechanical dissipation rate shows up in the spectrum as the FWHM of the mechanical response Lorentzian, a spectral measurement of Γ_m is necessarily imprecise due to the very low damping rates involved. For a mechanical mode with $Q = 10^7$ and $\omega_m = 2\pi \times 2\,\mathrm{MHz}$, $\Gamma_m/2\pi = 200\,\mathrm{mHz}$. To resolve this, a measurement time of at least 5-10 seconds is needed. During this time, the mechanical resonance frequency must be unchanged with a relative precision of $1/Q$, i.e. 0.1 ppm. Therefore, we rely on ring-down measurements to measure the mechanical dissipation.

To this end, we use the AOM in our setup to amplitude-modulate the light at the mechanical frequency, so as to optically excite it and measure the ring-down time. As the optical excitation beam might lead to optical (anti) broadening of the mechanics, we must somehow be able to rule out any such effect for the

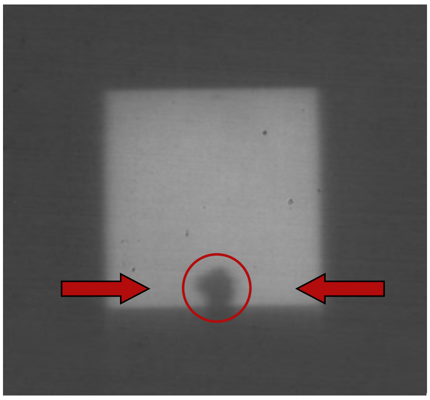

Figure 3.25: A horror picture. Photograph through an assembled cavity showing a large (diameter $\approx 70\,\mu\mathrm{m}$) dirt particle on the membrane.

measurement to be trustworthy. We address this issue now, before describing the actual excitation and read-out procedure.

3.7.2.1 Ruling Out Dynamical Back-action

In the very bad cavity limit, achieved when $\lambda \approx 740\,\mathrm{nm}$, the membrane will respond instantaneously to an applied radiation-pressure force, with no delay from the cavity. In other words, dynamical back-action effects are expected to be very small. This statement of course needs some qualification. In any setting where a laser beam continuously illuminates the cavity, the mechanical frequency shift and broadening of equations (2.109) and (2.110) apply, and we therefore measure not Γ_m but $\Gamma_m + \Gamma_{\mathrm{opt}}$. By working with a large cavity linewidth we can, however, make Γ_{opt} much smaller than Γ_m. For Q-factors in the range of ten millions for MHz mechanical frequencies, $\Gamma_m/2\pi$ is of the order of a hundred mHz. Therefore, once $\Gamma_{\mathrm{opt}}/2\pi$ is below $1\,\mathrm{mHz}$, we may safely conclude that dynamical back-action is irrelevant. To ensure that this condition is met, we may use the maximally broadening detuning, Δ_{ex}, of equation (2.117) to estimate a "worst case" Γ_{opt} for a given input power. For a given input power, P_{in}, and a given g_0, we calculate the resulting $g = \sqrt{\bar{n}_{\mathrm{cav}}}g_0$ using the following relation (we for now disregard the membrane modulation of cavity parameters):

$$\bar{n}_{\mathrm{cav}} = \frac{\eta\kappa}{\Delta_{ex}^2 + \kappa^2/4}\frac{P_{\mathrm{in}}}{\hbar\omega_{\mathrm{cav}}}, \tag{3.45}$$

where P_{in} is the input laser power. In the spirit of a worst-case scenario, we set $\eta = 1$. A Taylor expansion of Γ_{opt} to first order in the small parameter ω_m/κ

evaluated at Δ_{ex} yields

$$\Gamma_{\text{opt}} \approx 6\sqrt{3}\frac{g^2\omega_m}{\kappa^2} \quad (\omega_m \ll \kappa). \tag{3.46}$$

Combining equations (3.45) and (3.46) and using the following input parameters: $P_{\text{in}} = 3\,\text{mW}$, $g0 = 2\pi \times 150\,\text{Hz}$, $\omega_m = 2\pi \times 2\,\text{MHz}$, and $\omega_{\text{cav}} = 2\pi \times 400\,\text{THz}$, we find that $\Gamma_{\text{opt}} < 1\,\text{mHz}$ for $\kappa/2\pi > 5.3\,\text{GHz}$. We also display the rapid decay of Γ_{opt} with κ in Figure 3.26. At this large linewidth, the optical spring effect is already completely negligible; $1 - \delta\omega_{\text{opt}}/\omega_m$ is $\approx 2.5 \times 10^{-6}$ for $\kappa/2\pi \approx 5.3\,\text{GHz}$.

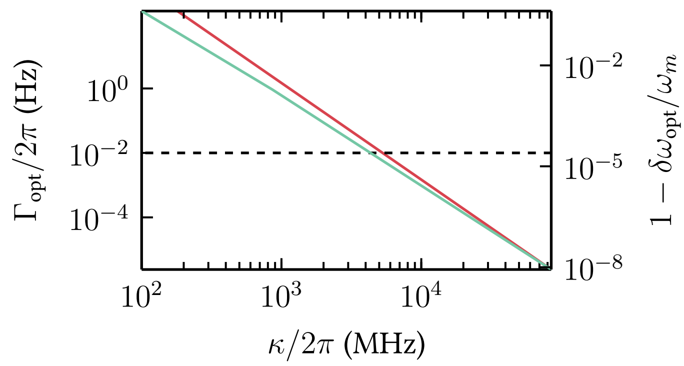

Figure 3.26: For reachable values of κ, dynamical back-action can be ruled out. Red: $\Gamma_{\text{opt}}/2\pi$, green: $1 - \delta\omega_{\text{opt}}/\omega_m$.

The question now is whether such a large κ is feasible. The ultimate upper limit on the cavity linewidth is the free spectral range of the cavity, which, for a cavity length of $1.7\,\text{mm}$ is roughly $88\,\text{GHz}$, leaving a good margin for κ to be large enough. If only we can tune the laser wavelength far enough away from the mirror coatings' maximal reflectivity, we should thus be fine. In Figure 3.27 we display a measurement series justifying that $\lambda \approx 740\,\text{nm}$ is indeed in the relevant range. It is difficult to precisely measure such large cavity linewidths, but using the slow piezo in the laser, the laser frequency can be scanned over several GHz whereby we may scan over the cavity resonance. By monitoring the wavelength during the scan, the scan can be calibrated in a rough way (assuming a linear response throughout the scan) and a linewidth may be extracted. In Figure 3.27 such a measurement series is shown. Although the laser piezo is specified to have a scan range of $25\,\text{GHz}$ this range is in practice compromised at lower wavelengths, where the laser frequency lock is weaker, and in practice we rather have $\approx 10\,\text{GHz}$ at $760\,\text{nm}$, making it hard to continue the measurement series below $758\,\text{nm}$, as the scan can no longer resolve the cavity resonance. This does, however, imply that κ

is sufficiently large. We conclude that an *in situ* measurement of the unperturbed mechanical dissipation is possible.

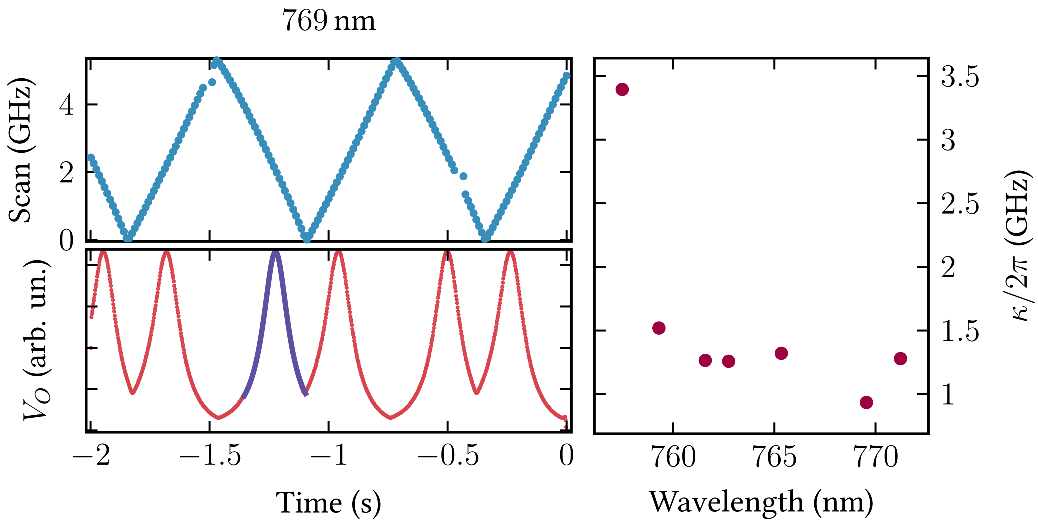

Figure 3.27: Cavity linewidth measurement. Left: exemplary fit of a Lorentzian to the cavity resonance. Right: A summary of the measured cavity linewidths.

3.7.2.2 The Ring-down Procedure

When optically exciting a membrane already inside the cavity, the excitation beam has to overlap with the beam path defined by the experiment. In other words, a second beam for reading out the membrane displacements (as used e.g. in an earlier work from our group [Usami et al., 2012]) will not be feasible, since it by necessity will overlap with the excitation beam. Although the beams could be separated using polarisation optics, the large amplitude of the excitation beam will make it difficult to suppress altogether. Instead, we use a single beam for both exciting and reading. In Figure 3.28 (left) we show the pulse sequence sent to the AOM. A voltage-controlled oscillator (VCO) supplies a constant tone at ω_{AOM} to deflect the laser beam at a certain angle (see also Figure 3.4). The VCO is controlled via a home-made switchboard, where a *positive* pulse turns *off* the VCO tone. In this way one can easily switch on and off the beam so as to generate a periodic radiation-pressure force and then leave the beam on for reading out the ring-down. This beam is then directed to a photodetector whose output current is demodulated by a lock-in amplifier demodulating at ω_m.

From equation (2.41) the output, $z_R(t)$, of the lock-in amplifier is equal to

$$z_R(t) = A\,\mathrm{e}^{-\Gamma_m t/2}, \tag{3.47}$$

where A is an experimental constant we need not worry about[17]. Fitting an exponential decay function of the form $f(t) = a\,\mathrm{e}^{-bt}$ then gives a ring down time, b, which is the *amplitude* ring-down time, and a quality factor, Q, then equal to

$$Q = \frac{\pi f_m}{b} = \frac{\omega_m}{2b}. \tag{3.48}$$

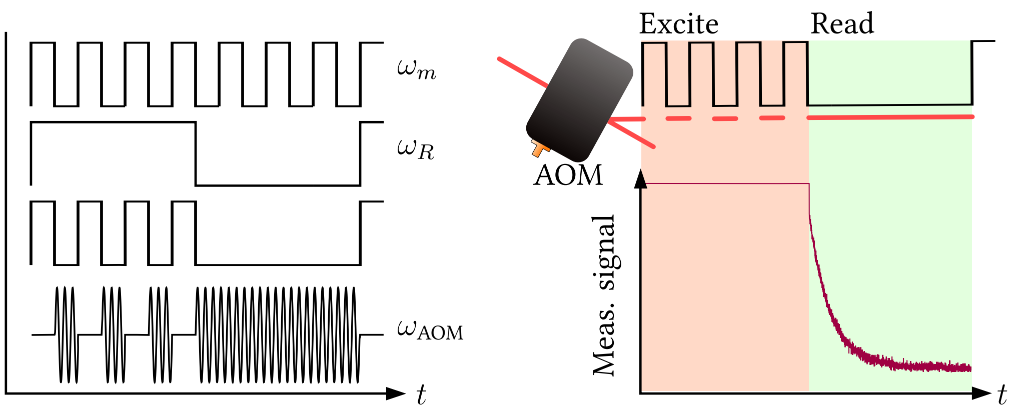

Figure 3.28: Ring-down measurements. Left: an overview of the four signals involved and their characteristic frequencies. Right: The resulting AOM signal and measurement.

3.8 The Temperature

Obtaining and measuring a low thermalisation temperature has been one of the more time and energy consuming endeavours of the work at hand.

3.8.1 Measuring the Membrane Temperature

We now turn to the task of measuring which bath temperature, T, is actually experienced by the membrane. The idea is to measure the effective bath temperature as well as the mechanical and optical dissipation rates to work out what the effective bath temperature is. The calibration measurements are performed with low

[17]In terms of the language of section 3.1.1, A is the $|G_{m,V}|$ translating metres to Volts.

input powers, meaning that quantum back-action is absent (we make this statement more quantitative below). The measurement procedure is slightly convoluted, so we first describe the general procedure, then explain in more detail how the measurements are performed, and finally evaluate the result. The temperature extraction procedure is based on the results of [Gorodetsky et al., 2010].

3.8.1.1 Temperature Extraction Procedure

We recall from section 2.3.4.1 (equation (2.113)) that the integrated displacement spectrum, $S_{zz}(\omega)$, considering only a single mechanical mode, has the value

$$\int_{-\infty}^{\infty} S_{zz}(\omega)\frac{\mathrm{d}\omega}{2\pi} = \frac{\Gamma_m}{\Gamma_{\text{eff}}}\frac{k_B T}{m_{\text{eff}}\omega_{\text{eff}}}. \tag{3.49}$$

Being satisfied with a precision of a few percent, we make the following approximation:

$$\frac{\Gamma_m}{\Gamma_{\text{eff}}}\frac{k_B T}{m_{\text{eff}}\omega_{\text{eff}}} \approx \frac{\Gamma_m}{\Gamma_{\text{opt}}}\frac{k_B T}{m_{\text{eff}}\omega_m}. \tag{3.50}$$

For phonon occupations, $\bar{n}_{\text{th}}$, reasonably far above the ground state, classical equilibrium dynamics hold and

$$\hbar\omega_m\bar{n}_{\text{th}} = k_B T. \tag{3.51}$$

This equation, combined with the relation (3.2) between the displacement PSD and frequency PSD, then reveals that

$$\int_{-\infty}^{\infty} S_{\omega\omega}(\omega)\frac{\mathrm{d}\omega}{2\pi} = 2G^2x_{\text{ZPF}}^2\frac{\Gamma_m}{\Gamma_{\text{opt}}}\bar{n}_{\text{th}} = 2g_0^2\bar{n}_{\text{eff}}. \tag{3.52}$$

As the spectral integral and the two decay rates Γ_m and Γ_{opt} can be measured independently, we can thus obtain values of $g_0^2\bar{n}_{\text{eff}}$ for different ambient temperatures. We describe how to extract T from this in a moment, but first briefly address the question of ruling out quantum back-action.

By comparing the last equality sign in equation (3.52) to the full quantum mechanical expression in equation (2.129) for the effective (final) phonon number, it is seen that two approximations have been made. Specifically,

$$\frac{\Gamma_{\text{opt}}\bar{n}_{\text{min}} + \bar{n}_{\text{th}}\Gamma_m}{\Gamma_{\text{opt}} + \Gamma_m} \approx \frac{\Gamma_m}{\Gamma_{\text{opt}}}\bar{n}_{\text{th}} \tag{3.53}$$

when

$$\Gamma_m \ll \Gamma_{\text{opt}}, \quad \Gamma_{\text{opt}}\bar{n}_{\text{min}} \ll \bar{n}_{\text{th}}\Gamma_m. \tag{3.54}$$

There is therefore an intermediate regime in which these measurements should be carried out, with neither too high nor too low (cavity-enhanced) coupling. In practice, as discussed in section 3.7.2.1, it actually takes some effort to enter the regime where Γ_{opt} is no longer much larger than Γ_m. Similarly, $\bar{n}_{\text{min}}\Gamma_{\text{opt}}$ is only comparable to $\Gamma_m\bar{n}_{\text{th}}$ close to the quantum ground state, and the intermediate regime actually covers most of the experimentally accessible parameter space.

Returning now to the problem at hand, determining T from a measurement of $g_0^2\bar{n}_{\text{th}}$ without knowing g_0, we make a crucial assumption: g_0 is constant over a certain range of temperatures. This allows us to measure *several* pairs of set temperatures and effective temperatures (times $g_0^2k_B/\hbar\omega_m$) and fit the proper relationship between them, thereby extracting T. Let us elaborate on this.

From section 2.2.3 we have a good classical model for the final temperature of a resonator exposed to two baths. In the present case we identify one bath as the surrounding laboratory environment at room temperature, T_{room}, and the other bath as the cryostat at the set temperature, T_s, to obtain

$$T = \frac{\gamma_1 T_s + \gamma_2 T_{\text{room}}}{\gamma_1 + \gamma_2}. \tag{3.55}$$

This function really only depends on one parameter, α, namely the ratio between γ_1 and γ_2. To our ends, we must also introduce another parameter, β, which translates from $g_0^2\bar{n}_{\text{th}}$ to T. That is, for a particular mechanical mode, $\beta = g_0^2\frac{k_B}{\hbar\omega_m}$. The function to fit to the data is then

$$f(T_s, \alpha, \beta) = \beta\frac{\alpha T_s + T_{\text{room}}}{\alpha + 1}. \tag{3.56}$$

In the next subsubsection we describe how to acquire simultaneous points of (T_s, $g_0^2\bar{n}_{\text{th}}$) but first we justify the essential assumption of a constant g_0.

Let us attack the question negatively. Why *wouldn't* g_0 be a constant over all temperatures? –Because the length of the cavity will in general change with temperature, whereby the optical resonance wavelengths change, which might in turn change the membrane position in $2kz_m$ (see sections 2.4 and 3.5.1). Since the length of the cavity is mainly defined by the length of the combined spacer-membrane-spacer stack, we might expect it to be given only by the coefficient of thermal expansion (CTE) of silicon. If this were the case, a cavity length change would actually *not* cause any change in the standing wave position of the membrane, as the thermal expansion/shrinking would amount to an overall scaling factor, which does not change *relative* positions. But there is also a non-negligible contribution to the cavity length from the curvature of the top mirror. With a radius of curvature of $2.5\,\mathrm{cm}$ and a diameter of $7.6\,\mathrm{mm}$, an extra contribution[18] of $0.27\,\mathrm{mm}$, or roughly $20\,\%$ of the cavity length, comes from this source, the length of which is given by the CTE of borosilicate. In Figure 3.29 we show the CTEs of Si and borosilicate. In the region from $0\,\mathrm{K}$ to $50\,\mathrm{K}$, they are both rather small. One would therefore expect only a very small shift in the cavity length as the temperature is varied throughout this region[19]

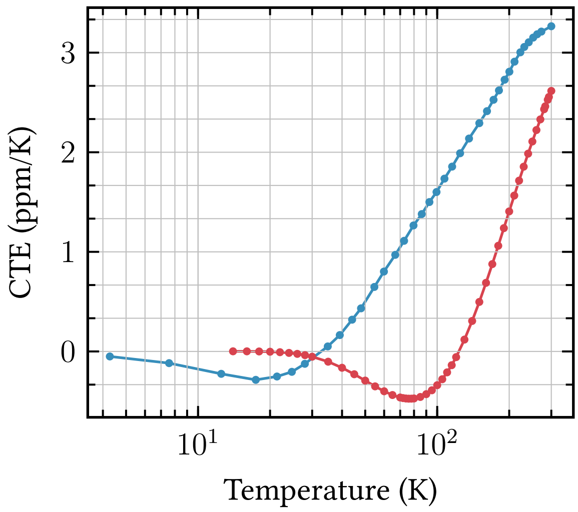

Figure 3.29: The thermal expansion coefficient of Si (red) and borosilicate (blue). Values adopted from [Lyon et al., 1977] (Si) and [Jacobs et al., 1984] (borosilicate[20]).

At the end of the day, the question must be decided by direct experiment. We track the wavelength of a particular cavity resonance ($\lambda \approx 800\,\mathrm{nm}$) as the temperature is increased from $4.2\,\mathrm{K}$ and upwards. As our tolerance we take $1\,\mathrm{pm}$ and cease the measurement when the cavity wavelength has changed by this amount. That leaves the range from $0\,\mathrm{K}$ to $25\,\mathrm{K}$ as a range of unchanged cavity length and thereby a constant g_0.

The choice of $1\,\mathrm{pm}$ was made somewhat arbitrarily. In hindsight, it proves

[18]Calculated as $d = R(1 - \cos(\arcsin(D/2R)))$, where R is radius of curvature of the mirror and D is the mirror diameter.

[19]Also, considering the shape of the CTE-curve, we note the possibility of recovering the $4.2\,\mathrm{K}$ length at a much higher temperature. From Figure 3.29, this would appear to be around $150\,\mathrm{K}$. This has not been tested experimentally, but would provide some very useful extra thermalisation points.

[20]For extraction of the borosilicate data, the online tool *Web Plot Digitizer* was used (`http://arohatgi.info/WebPlotDigitizer/app/`).

to be a little too conservative. We may estimate the worst case scenario were z_m remains unchanged as the cavity length changes on account of temperature. Given an initial cavity resonance wavelength, λ_0, the change in $2kz_m$ emanating from a change in wavelength, $\Delta\lambda$, is given by

$$\Delta(2kz_m) = 2z_m\Delta k = 4\pi z_m\left(\frac{1}{\lambda_0} - \frac{1}{\lambda_0 - \Delta\lambda}\right) \approx \frac{4\pi z_m}{\lambda_0^2}\Delta\lambda. \tag{3.57}$$

For $\lambda_0 = 800\,\text{nm}$, $\Delta(2kz_m)/2\pi$ takes a value of $1\,\%$ when $\Delta\lambda = 6.4\,\text{pm}$.

3.8.1.2 Measuring $g_0^2\bar{n}_{\text{th}}$

As explained in the previous subsection, we may determine the effective membrane bath temperature by fitting the function in equation (3.56) to simultaneous measurements of T_s and $g_0^2\bar{n}_{\text{th}}$. The latter is achieved, for each mechanical mode, by first tuning the laser to $\approx 745\,\text{nm}$ and performing optical ring-down measurements, as described in section 3.7.2.2, to extract Γ_m. Then, by setting the laser wavelength to an intermediate value of $\approx 800\,\text{nm}$ and placing a calibration tone near the mechanical peak of interest so as to calibrate the measured PSD in terms of frequency fluctuations (as described in section 3.1.1), the spectral integral, A, and the optical damping, Γ_{opt}, can be retrieved. In principle, once Γ_m is determined only one pair of (A, Γ_{opt}) is needed to determine $g_0^2\bar{n}_{\text{th}}$ from equation (3.52), but to get better statistics, we make a small detuning series and collect 4-5 such pairs. An overview of one such measurement, for a single mode for a single temperature, is shown in Figure 3.30.

As explained in section 3.8.1.1, we conclude that g_0 is constant in the range from $0\,\text{K}$ to $25\,\text{K}$. We take five points in this range and monitor four different mechanical modes. All four modes show thermalisation behaviour in good agreement with our expectation. In Figure 3.31 an overview of this measurement is shown. For the results presented in the next chapter, we assume the temperature calibration curve obtained here by linearly averaging the four fits in Figure 3.31 to hold. This produces the following temperature calibration function:

$$T_{\text{obtained}} = 0.99 \times T_s + 2.71\,\text{K}. \tag{3.58}$$

This concludes our exposition of the experimental setup. In the next, concluding section, we present the results obtained when pushing the experiment to its limits and operating it in the quantum regime.

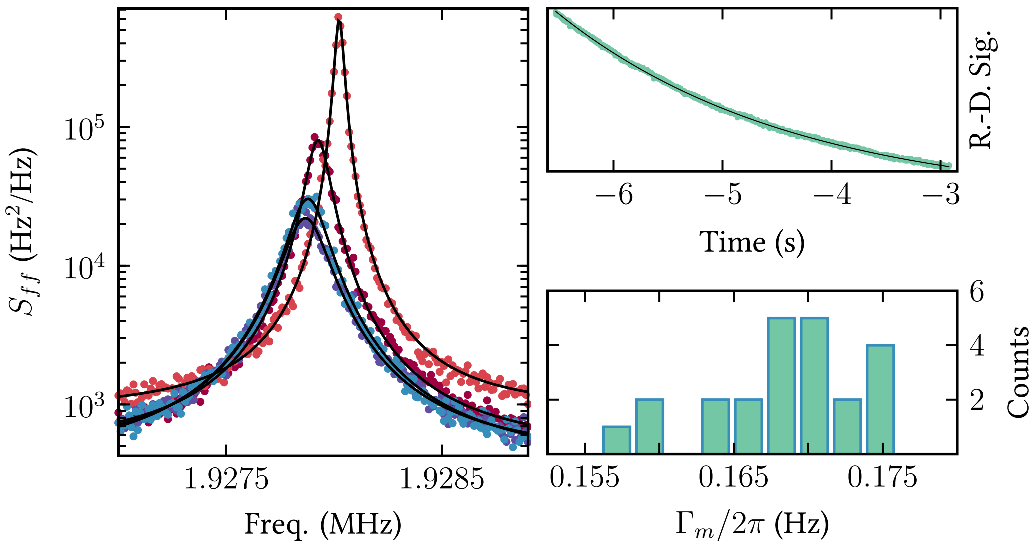

Figure 3.30: The measurements needed for determining a single point. Left: four calibrated spectra with fits (black lines) yielding Γ_{opt} and A. Right: ring-down measurements. Top: an exemplary trace. Bottom: histogram showing usual spread of values. Measurements for the $(3, 2)$-mode at 20 K.

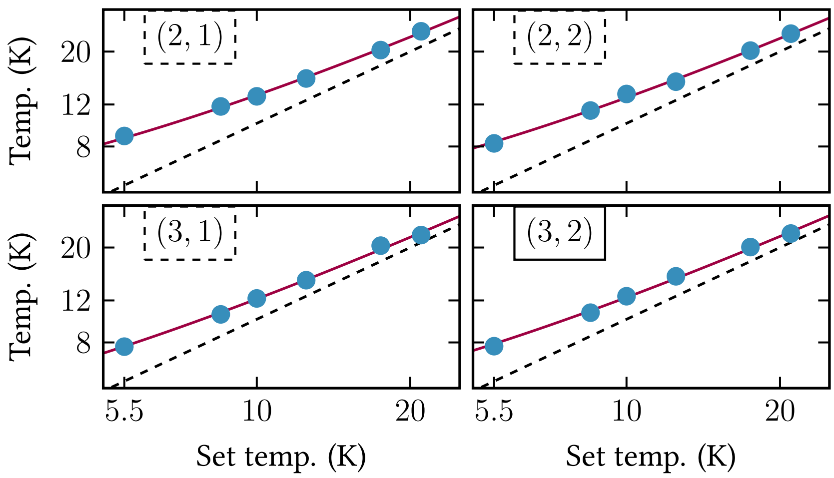

Figure 3.31: Thermal calibration for four mechanical modes. Dots: extracted bath temperature. Solid lines: fit using equation (3.56). Dashed line: identity. The error bars are within the dots.

Chapter 4

In the Quantum Regime

With the theory well understood and the full experiment standing ready on the table, we may now harvest the fruits of our labour. In this chapter, we present compelling evidence that we have reached our goal of realising a quantum-enabled optomechanical system.

The chapter falls naturally in two parts, each describing a separate endeavour. In the first part, we present the highlights of a very long list of attempted ground-state cooling runs. We argue that a mean phonon occupancy below unity has been reached, although that statement does come with a few assumptions. In the second part, we turn our attention to the results regarding ponderomotive squeezing, were there is little room for doubt. In that sense, the contents of section 4.2 constitute the main result of this work.

4.1 Ground State Cooling

For a long time, the experimental efforts of our group were focused on the goal of cooling a single vibrational mode to the ground state. Although the necessary quantum cooperativity to do so was reached, we cannot really claim to have been successful in that venture. There are two main reasons for this: excess noise and the difficulty of calibrating the phonon number precisely.

As discussed carefully in [Kippenberg et al., 2013], excess phase noise of the laser gives rise to an additional fluctuating force, leading to a heating of the mechanics. This also agrees with our discussion in section 2.3.4.2, were we found that the *quantum* noise of laser light leads to a non-vanishing heating contribution. With additional classical noise, the situation only gets worse. Now, we have argued in section 3.3.1 that input light is shot noise limited in the relevant spectral region, but perhaps the cavity is not. A mechanical mode of a mirror also leads to phase fluctuations of the light, which in turn may heat the mechanics. The same goes for any noise peak observed in the vicinity of the mechanical mode. We are deliberately being a bit vague on this matter, as one would need to explicitly model the physics of the noise in question to quantitatively determine the amount of added phonons. The main point is, however, clear enough: to confidently state that the shot-noise-only model of chapter 2 yields the correct phonon occupation, no excess noise near the mechanics can be tolerated. Considering both how sensitively one needs to measure to see the ground state and its expected spectral width, this shot-noise-only restriction turns out to be a very stringent one.

Regarding the calibration, it is of course not sufficient to state the estimated phonon number; one must include an uncertainty. It has not proven possible to simultaneously calibrate all input parameters with the sufficient precision to get a strict uncertainty bounding the occupancy to be below unity.

In spite of this somewhat pessimistic introduction, the cooling results we have obtained are indicative at the very least of an optomechanical system operating in the quantum regime. We now cover two different cooling runs which present some peak achievements of the experiment and also explore different parts of the parameter space. As we refrain from making strong claims about the occupation, we do not specify uncertainties on the experimental parameters. The uncertainties can be taken to be on the last digit.

4.1.1 Cooling Run A

In this cooling run, the overall plan was to make use of good sideband resolution to achieve a low phonon occupancy. A base wavelength of $818\,\mathrm{nm}$ was used, which from our measured mirror transmissivities (see Figure 3.16) should give a bare cavity linewidth of $1.6\,\mathrm{MHz}$. As explained in section 2.4, the precise position of the membrane in the intra-cavity standing wave leads to a periodic modulation of the cavity linewidth. In section 3.5.1 it was described how to experimentally order the cavity resonances according to their position in that period. For this run, we used the resonance yielding a narrow linewidth.

For a certain input power, the detuning is varied, yielding a different cavity-enhanced coupling for each detuning. This is repeated for different input powers as a way to exhaust the available parameter space and optimise the cooling. In Figure 4.1 we display three resulting spectra with model predictions superimposed. It is important to clarify which parameters enter the model and how they come about.

From broad OMIT measurements (see section 3.2.2.2), the cavity linewidth and

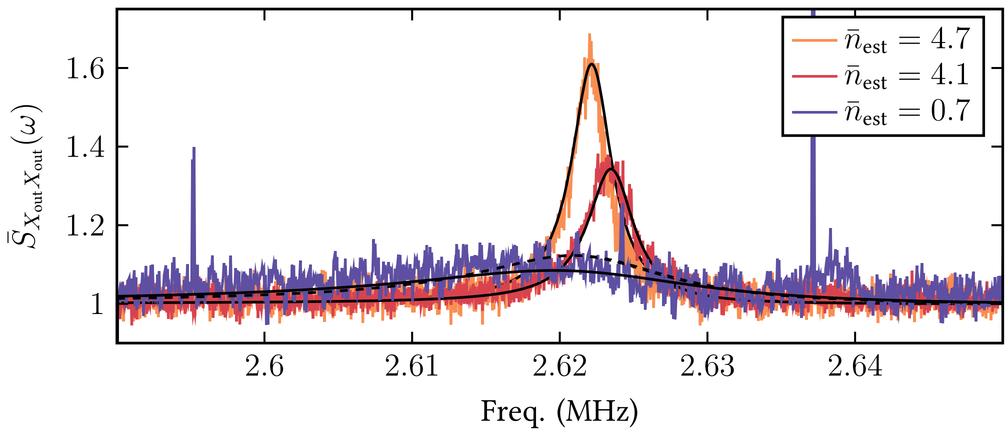

Figure 4.1: Serious cooling attempt. The legend shows the extracted phonon occupation from the solid line models. The dashed line shows the model for $\bar{n}_f = 1$.

detuning is inferred for each trace. The temperature is extracted from the temperature calibration measurement described in section 3.8.1 given the knowledge of the cryostat set temperature, which for these traces varied between $5.2\,\mathrm{K}$ and $5.4\,\mathrm{K}$. The mechanical resonance frequency and damping rate are both determined from the *in situ* ring-down measurements described in section 3.7.2. What remains to be fixed is the cavity-enchanced coupling and the detection efficiency. These parameters are adjusted until good agreement is found between data and model. A single detection efficiency simultaneously fits all three curves.

The traces are acquired with the highly sensitive APD at light levels yielding output fluctuations far above the electronic level. The traces are normalised to the noise level of a spectral region showing only shot noise, residing between $2.74\,\mathrm{MHz}$ and $2.75\,\mathrm{MHz}$, i.e. a $10\,\mathrm{kHz}$ spectrally flat region containing 1000 points.

A surprisingly low detection efficiency is necessary to fit the data. We arrive at $\eta = 0.033$, which agrees with the very low signal-to-noise ratio in the data, but not with the expected value. Let us estimate what η should be. From the mirror transmission curves of Figure 3.16, we get $\eta_c = 0.78$. On the "narrow linewidth" side of the $2kz_m$ curve, this gets modulated to $\eta_c = 0.61$ and the expected linewidth is $\kappa_{\text{exp}} = 2\pi \times 1.1\,\mathrm{MHz}$. Now, the linewidth that we measure is $\kappa_{\text{meas}} = 2\pi \times 2.0\,\mathrm{MHz}$. If we for simplicity assume the losses responsible for this to occur evenly throughout the cavity, we may calculate a new, modified coupling parameter as

$$\eta_c^{\text{lossy}} = \eta_c \frac{\kappa_{\text{exp}}}{\kappa_{\text{meas}}} \approx 0.32. \tag{4.1}$$

When multiplying this number by the quantum efficiency of the APD, the resulting detection efficiency remains a factor of almost 8 too high. We have not been able to find a satisfactory explanation for this low detection efficiency.

In Table 4.1 we summarise the parameters of the cooling run, both those measured independently and those adjusted in the analysis.

Parameter	Value	Measurement method
	Common parameters	
$\kappa/2\pi$	$2.0\,\mathrm{MHz}$	OMIT
$\Gamma_m/2\pi$	$0.24\,\mathrm{Hz}$	Ring-down
$\omega_m/2\pi$	$2.622\,551\,\mathrm{MHz}$	Ring-down
η	0.033	Not measured
	Individual traces	
T	$8.0\,\mathrm{K}$	Temperature calib.
$-\Delta/2\pi$	$0.42\,\mathrm{MHz}$	OMIT
$g/2\pi$	$4.1\times10^4\,\mathrm{Hz}$	Not measured
$\bar{n}_{\text{est}}$	4.7	Derived
C_q	0.22	Derived
T	$8.1\,\mathrm{K}$	Temperature calib.
$-\Delta/2\pi$	$0.28\,\mathrm{MHz}$	OMIT
$g/2\pi$	$6.0\times10^4\,\mathrm{Hz}$	Not measured
$\bar{n}_{\text{est}}$	4.1	Derived
C_q	0.47	Derived
T	$7.9\,\mathrm{K}$	Temperature calib.
$-\Delta/2\pi$	$0.40\,\mathrm{MHz}$	OMIT
$g/2\pi$	$11.0\times10^4\,\mathrm{Hz}$	Not measured
$\bar{n}_{\text{est}}$	0.7	Derived
C_q	1.6	Derived

Table 4.1: An overview of the parameters used in the analysis of cooling run A.

We now argue that the parameters set by us are trustworthy. From the independently acquired knowledge of ω_m, κ, and Δ, and the optical broadening, parametrised through g, the shape and position of the peak in the output light is established. If the peak broadening and position is to fit the data, a unique choice of g exists. For the vertical scaling, there is in principle a freedom of choice, in the sense that a high detection efficiency is balanced by a low occupation (and vice versa). In the few phonon regime, however, this is not quite true since the peak asymmetry is washed out for higher phonon occupations. This is particularly apparent in the high-asymmetry regime where ponderemotive squeezing is seen. We illustrate this in Figure 4.2 below, where we fix all parameters except T and η. For a given η, we then vary T until a certain peak height is obtained. This results in different peak shapes. Furthermore, as the bath temperature is independently calibrated, there is a fairly strict limit to the freedom in trading η for T. For these particular data, the only real concern is the very low signal-to-noise ratio making the uncertainty in the unique parameter rather large. In Figure 4.1 a dashed model curve showing $\bar{n}_f = 1$ for the same parameters (expect g) used in the $\bar{n}_{\text{est}} = 0.7$-curve is shown. Albeit a marginal difference, we believe that the dashed curve fits the data worse.

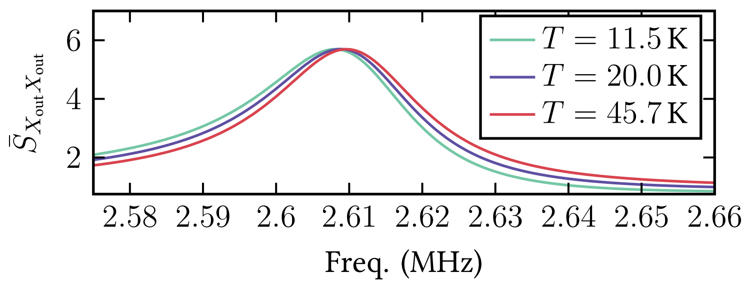

Figure 4.2: The trade-off between η and T for the parameters from section 4.1.2. The detection efficiencies used are 0.74, 0.5 and 0.25. The resulting phonon occupations are 1.2, 1.8, and 3.8.

4.1.2 Cooling Run B

Abandoning the resolved sideband regime, this cooling run was performed at a base wavelength of $807\,\text{nm}$. Furthermore, we this time worked at the $2kz_m$ position yielding a large cavity linewidth. This entails a larger output signal, allowing us to use the QD detector. For this detector, more carefully calibrated shot noise traces are available. For the calibration of the measured traces, we then apply the following transformation

$$S_{VV}^{\text{meas}} \to \frac{(S_{VV}^{\text{meas}} - C_{\text{el}})C_{\text{SN}}^{\text{DC}}}{(C_{\text{SN}} - C_{\text{el}})C_{\text{meas}}^{\text{DC}}} + C_{\text{el}}, \tag{4.2}$$

where the four calibration constants are the DC levels of respectively the shot noise trace and the measured trace and the average of the spectral region between $2.48\,\text{MHz}$ and $2.74\,\text{MHz}$ for the electronic noise trace and the shot noise trace.

Apart from this more precise calibration, the analysis proceeds equivalently to what was presented in the last section. From ring-down measurements we extract ω_m and Γ_m, OMIT measurements yield κ and Δ, and we extract the bath temperature from our temperature calibration measurements. Finally, η and g are adjusted to make the data fit the model. In Figure 4.3 we show the record trace of this particular cooling run.

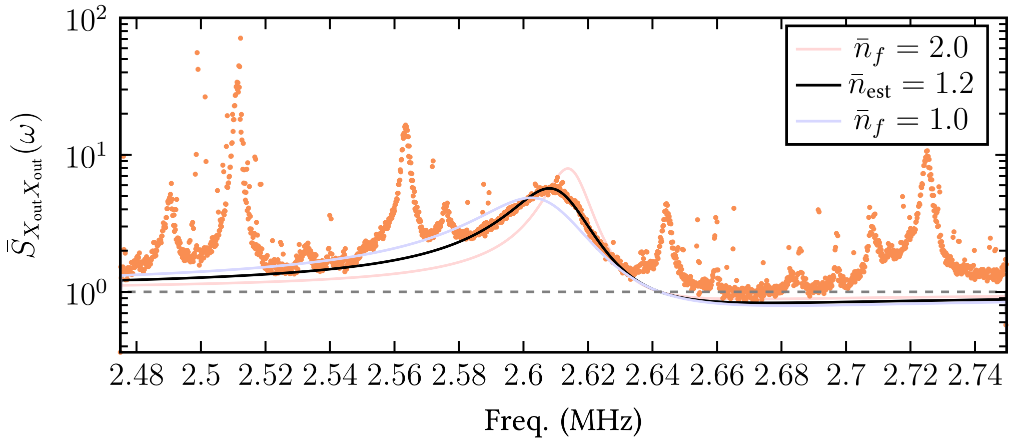

Figure 4.3: Serious cooling attempt. The legend shows the extracted phonon occupation from the solid line models. The dashed line shows the shot noise level of the model.

Encouragingly, the signal-to-noise ratio is better than before, but this improved sensitivity reveals some additional noise of unknown and unwelcome origin. As already discussed, without a specific model for this noise it is not possible to quantitatively assert what heating effect it could have on the mechanics. Nonetheless, assuming no effect, our model prediction seems to agree with the data. We arrive at a value for the detection efficiency of $\eta = 0.74$. The shape of the curve fits very well with our model prediction, and a phonon occupancy close to unity is reached. In the spirit of our semi-qualitative data analysis, we also show the two curves corresponding to occupations of 1 and 2, obtained by varying g. With the resolution at hand, the data seems easily discernible from those cases. In Table 4.2 an overview of all experimental parameters is found.

Shown in Figure 4.3 is also the expected shot noise level, indicating that some modest level of ponderomotive squeezing should be present. The excess noise in this spectral region may be assumed to wash out the squeezing correlations. This result is encouraging, however, in the sense that both the cooperativity and the detection efficiency necessary to observe ponderomotive squeezing are present.

Parameter	$\kappa/2\pi$	$-\Delta/2\pi$	T	$\omega_m/2\pi$	$\Gamma_m/2\pi$
Value	$6.3\,\mathrm{MHz}$	$3.1\,\mathrm{MHz}$	$11.5\,\mathrm{K}$	$2.620\,440\,\mathrm{MHz}$	$0.24\,\mathrm{Hz}$

Parameter	$g/2\pi$	η	$\bar{n}_{\mathrm{est}}$	C_q
Value	$23 \times 10^4\,\mathrm{Hz}$	0.74	1.2	1.5

Table 4.2: Parameter overview for this cooling run. Top table: independently measured parameters. Bottom table: Fitted and derived parameters.

Even if the ground state is just barely out of experimental reach, squeezing should not be. Indeed, it is not, and in the next section we present the results of focusing the experimental efforts in that direction.

4.2 Ponderomotive Squeezing

From the experimentalist's point of view, a squeezing experiment is nice and clean in the sense that very little calibration is necessary. Unlike the sideband cooling described in the previous section, where different noise contributions should be accounted for in order to gauge the final mechanical occupation, squeezing is self-calibrating and model agnostic. With a careful independent shot-noise calibration of the detector (in this case the QD detector), we can unambiguously infer the amount of light squeezing achieved.

We now present the best squeezing run out of several successful ones. From the considerations of chapter 2, it follows that we should "attack" at a large linewidth (see Figure 2.16) and at a wavelength corresponding to $2kz_m \approx 0.8$ in Figure 2.23. Here, the maximal bare coupling is achieved simultaneously with the largest degree of cavity overcoupling. In this particular experimental run, a wavelength of $799.877\,\mathrm{nm}$ brought us very close to the optimal working point. For different input powers, different degrees of detuning can be reached, owing to the different instabilities of the system (see section 3.2.2.1). As a consequence, we vary the input power and thereby find the optimal working point, similarly to what was done in connection with the cooling described above.

In Figure 4.4 we show the raw data trace of the best squeezing run. In the large-cooperativity regime where we operate, the output spectrum is completely dominated by the broad spectral features of the mechanical modes. Squeezing

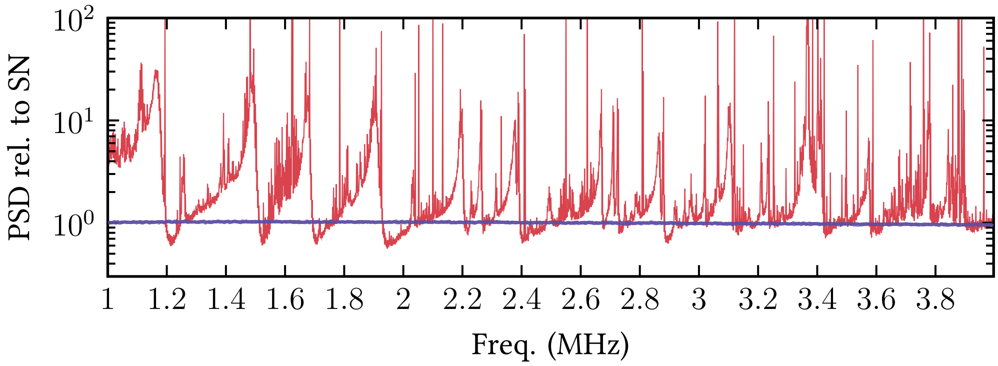

Figure 4.4: Raw broadband squeezing data. The red curve is the recorded output spectrum. The purple curve is the shot noise reference. Both traces are *globally* scaled, meaning that small discrepancies occur wrt. the y-axis (a careful eye will notice a small bend of the purple trace). The amount of squeezing can, at any frequency, be directly inferred from comparing the two curves.

is seen for more than 13 distinct mechanical modes. This is it! Strong quantum correlations between light and mechanics are unquestionably present in the output light from the cavity.

To gauge our theoretical understanding of the data, six modes are selected for comparison to the model presented in section 2.3.5.2. In Figure 4.5 we show a comparison between sections of the data trace from figure 4.4. All parameters entering the model are independently determined using methods described in chapter 3. The cavity linewidth is determined via a sideband calibration, and found to be $14.0\,\mathrm{MHz}$. From broad OMIT sweeps, the detuning may then be inferred to be $-1.8\,\mathrm{MHz}$. The temperature follows from the temperature calibration curves, $T = 10.1\,\mathrm{K}$ for a cryostat set temperature of $7.4\,\mathrm{K}$. These are the parameters common for all modes. For four of the modes, optically excited ring-downs yield quality factors of respectively $(11.5 \pm 0.2) \times 10^6$ for the (1, 2)-mode, $(11.4 \pm 0.1) \times 10^6$ for the (1, 3)-mode, $(11.5 \pm 0.3) \times 10^6$ for the (1, 3)-mode, and $(11.5 \pm 0.2) \times 10^6$ for the (2, 2)-mode. From this strong consistency of Q-value, a consequence of the phononic bandgap, we set the quality factor to be 11.5×10^6 for all modes in the model. The mechanical frequency and cavity-enhanced coupling rate are both inferred from OMIT fits, also shown in Figure 4.5. The final parameter that requires fixing is the detection efficiency. Contrary to the cooling analysis, where we left this as a free parameter, we independently measure it for this run.

The calculation of η involves two steps. First, the degree of cavity overcoupling is evaluated from the transfer matrix model. This model takes eight input parameters. We have independently measured the membrane reflectivity and the mirror reflectivities. Together with the inferred transmissivities, this constitutes six parameters. The cavity length and membrane position are inferred from a model fit to the resonance frequencies. The transfer matrix model then predicts a cavity linewidth of 14 MHz and a cavity overcoupling of 0.96. Next, we propagate losses after the cavity into the efficiency. The output window of the cryostat is *not* anti-reflection coated and thus constitutes a small Fabry-Pérot etalon. A careful measurement of the window transmission reveals that it is very near unity at $\lambda = 799.877\,\text{nm}$. The QD detector has a nominal diode quantum efficiency of 0.87 and a glass shielding of the diode with an estimated transmissivity of 0.92. Assuming no further losses, the expected detection efficiency is $\eta = \eta_c \times 0.87 \times 0.92 \approx 0.76$. Using this value, we thus have a zero-free-parameters fit to superimpose on the data. In Figure 4.5 this is seen as the grey curves. They do not quite fit the data, and in particular simultaneously overshoot the measured peak value and overestimate the degree of measured squeezing. Reducing the detection efficiency simultaneously addresses both these errors, whereas e.g. a higher thermalisation temperature than expected would only move the model curves upwards. If we allow ourselves to vary the detection efficiency (but of course using the same number for all six modes), we can obtain good agreement between model and data by assuming $\eta = 0.61$. At the time of writing, we can not immediately account for the mismatch between expected and realised detection efficiency. Candidate explanations include imprecisions on the transfer matrix model implying an incorrect value η_c, beam focusing mismatch on the detector diode, scratches in or silicon debris on the back surface of the outcoupler mirror, and lossy (dirty) optics.

From the fixed parameters entering our model, we may also evaluate the quantum cooperativity for the six modes of Figure 4.5. These are shown in Table 4.3.

Mode number	(1, 2)	(2, 2)	(1, 3)	(2, 3)	(1, 4)	(3, 4)
C_q	6.1	5.0	3.4	5.4	3.2	1.8

Table 4.3: The measured quantum cooperativities for the six most strongly coupled mechanical modes.

We now make a few remarks on the shortcomings of our model. Evidently, the squeezing decreases as a function of Fourier frequency much faster than our model predicts. This is partly due to the inherent single-mode nature of our model, which, as we already remarked upon in section 2.3.2, becomes compromised when

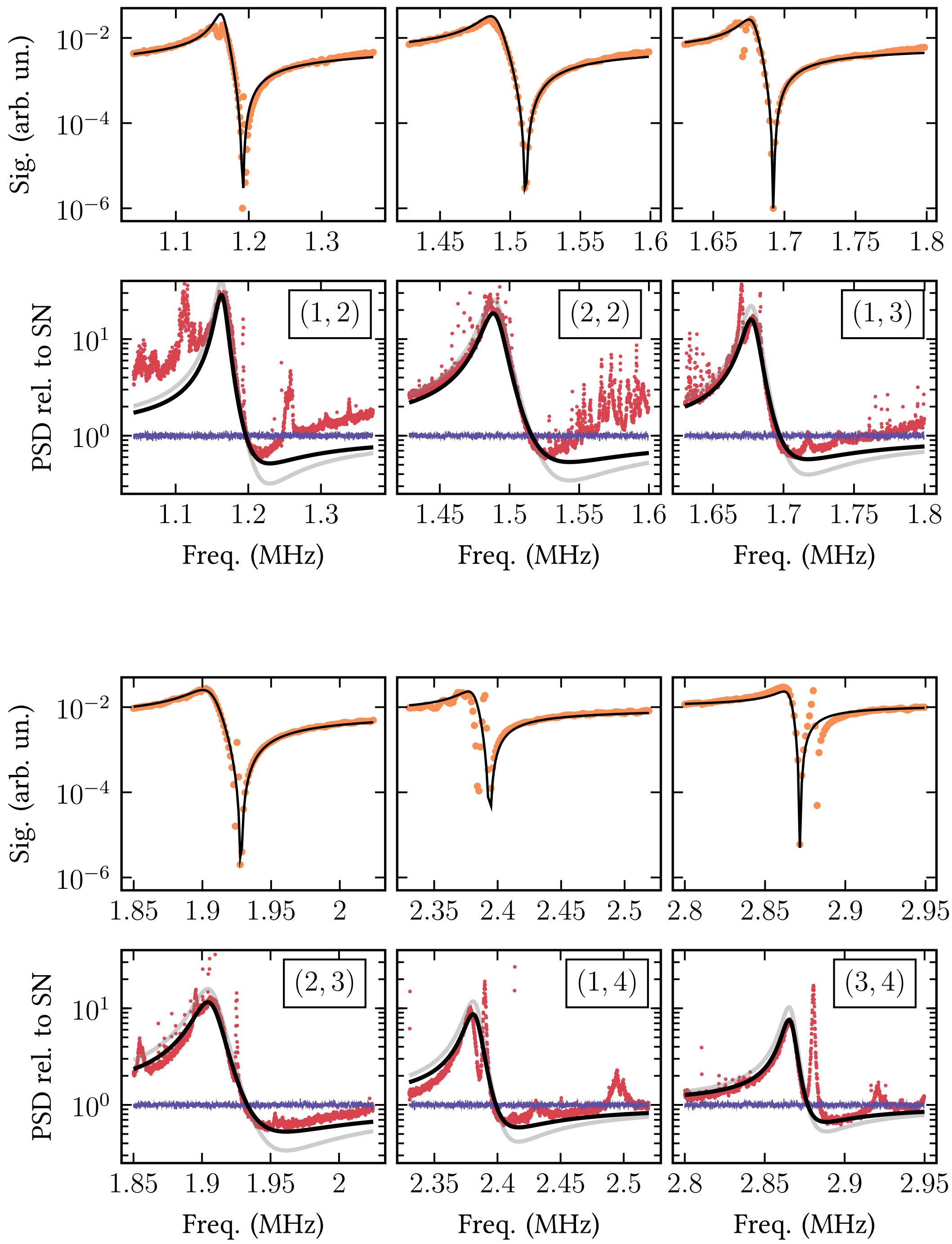

Figure 4.5: Record squeezing run. Top panels: OMIT response (orange) and fit (black) from each mechanical mode. Bottom panels: Measured spectra (red) normalised to shot noise (purple) and superimposed model prediction for both the expected (grey) and adjusted (black) detection efficiency. For the adjusted detection efficiency, good agreement is seen between model and data.

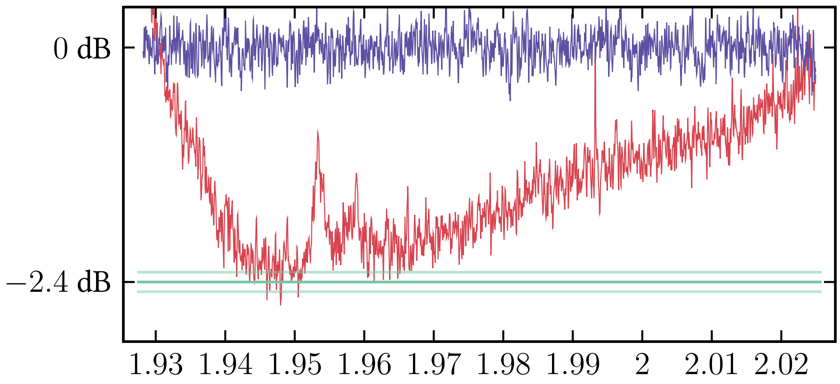

Figure 4.6: The maximal amount of squeezing. The green lines indicate the level of -2.4 dB and 0.1 dB to either side.

the mechanical linewidths become comparable to the inter-modal spacing. A quick look at Figure 4.4 will reveal that this is certainly the regime we are in. In the region to the right of the mechanical peak, where our single-mode model predicts a slowly rising fluctuation spectrum, the tail of the next mechanical mode is already making a significant contribution. Furthermore, the mirror noise levels presented in section 3.4.4 are relatively high and should, in a more thorough treatment, be taken into account, as extraneous noise sources will wash out the quantum correlations.

From the raw data of the response of the (2, 3)-mode, we infer a maximal amount of squeezing of -2.4 dB ± 0.1 dB. This is illustrated in Figure 4.6.

4.3 Concluding Remarks

The overall conclusion is the happy one that we have indeed been successful in reaching the quantum regime. The experiment, in its present state of operation, constitutes a compact and robust optomechanical system showing a simultaneous quantum-enabled coupling of light to several mechanical modes. Although other optomechanical systems have observed ponderomotive squeezing, first in the optomechanical crystals [Safavi-Naeini et al., 2013] and more recently another MIM system [Purdy et al., 2013], we note that the amount of squeezing presented here is appreciably larger, and thus represents the hitherto strongest correlations between light and mechanics reported for an optomechanical system. It is the combination of high quantum cooperativities and good detection efficiencies that distinguishes our system and allows for the large degree of observed squeezing.

On the assembly side, the essential ingredients in reaching the goal was the addition of a phononic structure around the membrane, which lead to consistently high quality factors for a wide range of mechanical modes as well as the spectral suppression of large amounts of spurious modes and the use of a very stable and noise-free laser.

Although the system is functioning satisfactorily, there are a few places where improvements would be welcome. First, the jitter induced in the cavity by the helium flow is a large inconvenience, and hinders the effective acquisition of large amounts of data over several days. A different cryogenic solution might alleviate this. Second, the vibrational modes of the mirrors seem to currently be a limiting noise source for certain experiments. Using smaller-mass mirrors with higher vibrational eigenfrequencies and, potentially, higher quality factors would alleviate most of the mirror noise. One might even the mirrors to also be protected by a phononic structure. Smaller mirrors could also allow for a shorter cavity leading to an increase in the mode-specific optomechanical coupling g_{nm} both through the increase in $\partial\omega_{\mathrm{cav}}/\partial z_m$ and the transverse overlap.

Finally, as the goal of our project was to prepare an optomechanical setup for more advanced experiments, the future prospects of the experiment are very compelling. In the QUANTOP laboratory, the hybrid atom-membrane experiment [Hammerer et al., 2009] is already in its early stages, and another experiment to entangle two laser beams is being initiated shortly. The system presented here generally is a promising platform for going beyond the canonical single-mode optomechanics.

Bibliography

[Abbott et al., 2016] Abbott, B. P., Abbott, R., Abbott, T. D., Abernathy, M. R., Acernese, F., Ackley, K., Adams, C., Adams, T., Addesso, P., Adhikari, R. X., and et al. (2016). Observation of gravitational waves from a binary black hole merger. *Phys. Rev. Lett.*, 116(6). (Cited on page 2.)

[Agarwal and Huang, 2010] Agarwal, G. S. and Huang, S. (2010). Electromagnetically induced transparency in mechanical effects of light. *Phys. Rev. A*, 81(4). (Cited on page 54.)

[Arcizet et al., 2009] Arcizet, O., Rivière, R., Schliesser, A., Anetsberger, G., and Kippenberg, T. J. (2009). Cryogenic properties of optomechanical silica microcavities. *Phys. Rev. A*, 80(2). (Cited on page 90.)

[Aspelmeyer et al., 2014] Aspelmeyer, M., Kippenberg, T. J., and Marquardt, F. (2014). Cavity optomechanics. *Rev. Mod. Phys.*, 86(4):1391–1452. (Cited on pages 3, 27, 29, 39, and 45.)

[Bao et al., 2002] Bao, M., Yang, H., Yin, H., and Sun, Y. (2002). Energy transfer model for squeeze-film air damping in low vacuum. *J. Micromech. Microeng.*, 12:341. (Cited on page 104.)

[Black, 2000] Black, E. D. (2000). An introduction to Pound–Drever–Hall laser frequency stabilization. *Am. J. Phys.*, 69:79–87. (Cited on page 71.)

[Bose et al., 1997] Bose, S., Jacobs, K., and Knight, P. L. (1997). Preparation of nonclassical states in cavities with a moving mirror. *Phys. Rev. A*. (Cited on page 3.)

[Bowen and Milburn, 2016] Bowen, W. P. and Milburn, G. J. (2016). *Quantum Optomechanics*. CRC Press. (Cited on pages 33 and 34.)

[Braginsky and Khalili, 1992] Braginsky, V. B. and Khalili, F. Y. (1992). *Quantum Measurement*. Cambridge University Press. (Cited on page 3.)

[Braginsky and Manukin, 1967] Braginsky, V. B. and Manukin, A. B. (1967). Ponderomotive effects of electromagnetic radiation. *Soviet Physics JETP*. (Cited on page 2.)

[Braginsky et al., 1970] Braginsky, V. B., Manukin, A. B., and Tikhonov, M. Y. (1970). Investigation of dissipative ponderomotive effects of electromagnetic radiation. *Soviet Physics JETP*. (Cited on page 2.)

[Broersen, 2006] Broersen, P. H. (2006). *Automatic Autocorrelation and Spectral Analysis*. Springer-Verlag. (Cited on page 17.)

[Campillo and Hsu, 2002] Campillo, A. L. and Hsu, J. W. P. (2002). Near-field scanning optical microscope studies of the anisotropic stress variations in patterned sin membranes. *J. Appl. Phys.*, 91(2):646. (Cited on page 60.)

[Caves, 1980] Caves, C. M. (1980). Quantum-Mechanical Radiation-Pressure Fluctuations in an Interferometer. *Phys. Rev. Lett.*, 45(2):75. (Cited on page 2.)

[Caves, 1981] Caves, C. M. (1981). Quantum-mechanical noise in an interferometer. *Phys. Rev. D*, 23(8):1693. (Cited on page 2.)

[Chakram et al., 2014] Chakram, S., Patil, Y. S., Chang, L., and Vengalattore, M. (2014). Dissipation in ultrahigh quality factor sin membrane resonators. *Phys. Rev. Lett.*, 112(12). (Cited on page 104.)

[Chan et al., 2011] Chan, J., Alegre, T. P. M., Safavi-Naeini, A. H., Hill, J. T., Krause, A., Gröblacher, S., Aspelmeyer, M., and Painter, O. (2011). Laser cooling of a nanomechanical oscillator into its quantum ground state. *Nature*, 478(7367):89–92. (Cited on page 3.)

[Clerk et al., 2010] Clerk, A. A., Devoret, M. H., Girvin, S. M., Marquardt, F., and Schoelkopf, R. J. (2010). Introduction to quantum noise, measurement, and amplification. *Rev. Mod. Phys.*, 82(2):1155–1208. (Cited on pages 28 and 43.)

[Cohadon et al., 1999] Cohadon, P. F., Heidmann, A., and Pinard, M. (1999). Cooling of a mirror by radiation pressure. *Phys. Rev. Lett.* (Cited on page 3.)

[Edwards et al., 2004] Edwards, R. L., Coles, G., and Sharpe, W. N. (2004). Comparison of tensile and bulge tests for thin-film silicon nitride. *Exp. Mech.*, 44(1):49–54. (Cited on page 20.)

[Eichenfield et al., 2009] Eichenfield, M., Chan, J., Camacho, R. M., Vahala, K. J., and Painter, O. (2009). Optomechanical crystals. *Nature*, 462:78. (Cited on page 3.)

[Einstein, 1915] Einstein, A. (1915). Feldgleichungen der Gravitation. *Königlich Preußische Akademie der Wissenschaften, Sitzungsberichte*, pages 844–847. (Cited on page 2.)

[Einstein, 1916] Einstein, A. (1916). Näherungsweise Integration der Feldgleichungen der Gravitation. *Königlich Preußische Akademie der Wissenschaften, Sitzungsberichte*, pages 688–696. (Cited on page 2.)

[Fabre et al., 1994] Fabre, C., Pinard, M., Bourzeix, S., Heidmann, A., Giacobino, E., and Reynaud, S. (1994). Quantum-noise reduction using a cavity with a movable mirror. *Phys. Rev. A*. (Cited on page 3.)

[Faust et al., 2014] Faust, T., Rieger, J., Seitner, M. J., Kotthaus, J. P., and Weig, E. M. (2014). Signatures of two-level defects in the temperature-dependent damping of nanomechanical silicon nitride resonators. *Phys. Rev. B*, 89(10). (Cited on page 104.)

[Fogedby and Imparato, 2011] Fogedby, H. C. and Imparato, A. (2011). A bound particle coupled to two thermostats. *J. Stat. Mech. Theor. Exp.* (Cited on page 25.)

[Gardiner, 2009] Gardiner, C. (2009). *Stochastic Methods A Handbook for the Natural and Social Sciences*. Springer-Verlag, fourth edition. (Cited on pages 14 and 24.)

[Gardiner, 1991] Gardiner, C. W. (1991). *Quantum Noise*. Springer. (Cited on page 34.)

[Gardiner and Collett, 1985] Gardiner, C. W. and Collett, M. J. (1985). Input and output in damped quantum systems: Quantum stochastic differential equations and the master equation. *Phys. Rev. A*. (Cited on page 34.)

[Gillespie, 1996] Gillespie, D. T. (1996). The mathematics of Brownian motion and Johnson noise. *Am. J. Phys.*, 64:225–240. (Cited on page 24.)

[Giovannetti and Vitali, 2001] Giovannetti, V. and Vitali, D. (2001). Phase-noise measurement in a cavity with a movable mirror undergoing quantum brownian motion. *Phys. Rev. A*, 63(2). (Cited on page 34.)

[Gorodetsky et al., 2010] Gorodetsky, M. L., Schliesser, A., Anetsberger, G., Deleglise, S., and Kippenberg, T. J. (2010). Determination of the vacuum optomechanical coupling rate using frequency noise calibration. *Opt. Express*, 18:23236. (Cited on pages 69 and 112.)

[Grote et al., 2013] Grote, H., Danzmann, K., Dooley, K. L., Schnabel, R., Slutsky, J., and Vahlbruch, H. (2013). First Long-Term Application of Squeezed States of Light in a Gravitational-Wave Observatory. *Phys. Rev. Lett.*, 110(18). (Cited on page 2.)

[Hammerer et al., 2009] Hammerer, K., Aspelmeyer, M., Polzik, E. S., and Zoller, P. (2009). Establishing Einstein-Podolsky-Rosen Channels between Nanomechanics and Atomic Ensembles. *Phys. Rev. Lett.*, 102:020501. (Cited on pages 4 and 128.)

[Harry and Bodiya, 2012] Harry, G. and Bodiya, T. P., editors (2012). *Optical Coatings and Thermal Noise in Precision Measurement*. Cambridge University Press. (Cited on page 69.)

[Haus, 1984] Haus, H. A. (1984). *Waves and fields in optoelectronics*. Prentice Hall. (Cited on page 6.)

[Jacobs et al., 1984] Jacobs, S. F., Shough, D., and Connors, C. (1984). Thermal expansion uniformity of materials for large telescope mirrors. *Appl. Opt.*, 23(23):4237. (Cited on page 114.)

[Jayich et al., 2008] Jayich, A. M., Sankey, J. C., Zwickl, B. M., Yang, C., Thompson, J. D., Girvin, S. M., Clerk, A. A., Marquardt, F., and Harris, J. G. E. (2008). Dispersive optomechanics: a membrane inside a cavity. *New J. Phys.*, 10:095008. (Cited on pages 59 and 61.)

[Jöckel et al., 2011] Jöckel, A., Rakher, M. T., Korppi, M., Camerer, S., Hunger, D., Mader, M., and Treutlein, P. (2011). Spectroscopy of mechanical dissipation in micro-mechanical membranes. *Appl. Phys. Lett.*, 99(14):143109. (Cited on page 106.)

[Julsgaard et al., 2001] Julsgaard, B., Kozhekin, A., and Polzik, E. S. (2001). Experimental long-lived entanglement of two macroscopic objects. *Nature*, 413:401. (Cited on page 4.)

[Kalinkevich, 1978] Kalinkevich, A. A. (1978). Effect of a dielectric film on the characteristics of an open fabry-pérot resonator cavity. *Izvestiya Vysshikh Uchebnykh Zavedenii, Radiofizika*, 21(11):1648. (Cited on page 87.)

[Kaushik et al., 2005] Kaushik, A., Kahn, H., and Heuer, A. (2005). Wafer-level mechanical characterization of silicon nitride MEMS. *J. Microelectromech. Syst.*, 14(2):359–367. (Cited on page 20.)

[Kippenberg et al., 2013] Kippenberg, T. J., Schliesser, A., and Gorodetsky, M. L. (2013). Phase noise measurement of external cavity diode lasers and implications for optomechanical sideband cooling of ghz mechanical modes. *New J. Phys.*, 15(1):015019. (Cited on pages 90 and 117.)

[Kippenberg and Vahala, 2007] Kippenberg, T. J. and Vahala, K. J. (2007). Cavity opto-mechanics. *Opt. Express*, 15(25):17172. (Cited on page 3.)

[Landau and Lifshitz, 1986] Landau, L. D. and Lifshitz, E. M. (1986). *Theory of Elasticity*, volume 7 of *Course of Theoretical Physics*. Pergamon Press, third english edition. (Cited on pages 18 and 19.)

[Law, 1995] Law, C. K. (1995). Interaction between a moving mirror and radiation pressure: A Hamiltonian formulation. *Phys. Rev. A*, 51:2537–2541. (Cited on page 31.)

[Leissa, 1969] Leissa, A. W. (1969). *Vibration of Plates*. NASA. (Cited on page 18.)

[Lifshitz, 2002] Lifshitz, R. (2002). Phonon-mediated dissipation in micro- and nano-mechanical systems. *Physica B*. (Cited on page 104.)

[Loudon, 1973] Loudon, R. (1973). *The Quantum Theory of Light*. Clarendon Press. (Cited on page 82.)

[Lyon et al., 1977] Lyon, K. G., Salinger, G. L., Swenson, C. A., and White, G. K. (1977). Linear thermal expansion measurements on silicon from 6 to 340 K. *J. Appl. Phys.*, 48(3):865. (Cited on page 114.)

[Maldovan, 2013] Maldovan, M. (2013). Sound and heat revolutions in phononics. *Nature*, 503(7475):209–217. (Cited on page 105.)

[Mancini et al., 2002] Mancini, S., Giovannetti, V., Vitali, D., and Tombesi, P. (2002). Entangling macroscopic oscillators exploiting radiation pressure. *Phys. Rev. Lett.*, 88(12). (Cited on page 3.)

[Mancini and Tombesi, 1994] Mancini, S. and Tombesi, P. (1994). Quantum noise reduction by radiation pressure. *Phys. Rev. A*, page 4055. (Cited on page 3.)

[Mancini et al., 1998] Mancini, S., Vitali, D., and Tombesi, P. (1998). Optomechanical cooling of a macroscopic oscillator by homodyne feedback. *Phys. Rev. Lett.*, page 688. (Cited on page 3.)

[Marquardt et al., 2007] Marquardt, F., Chen, J. P., Clerk, A. A., and Girvin, S. M. (2007). Quantum theory of cavity-assisted sideband cooling of mechanical motion. *Phys. Rev. Lett.*, 99(9). (Cited on page 43.)

[Marshall et al., 2003] Marshall, W., Simon, C., Penrose, R., and Bouwmeester, D. (2003). Towards quantum superpositions of a mirror. *Phys. Rev. Lett.* (Cited on page 3.)

[Milonni and Eberly, 1988] Milonni, P. W. and Eberly, J. H. (1988). *Lasers*. John Wiley & Sons Inc. (Cited on pages 9 and 96.)

[Philipp, 1973] Philipp, H. R. (1973). Optical Properties of Silicon Nitride. *J. Electrochem. Soc.*, 120:295–300. (Cited on page 60.)

[Pierson, 1999] Pierson, H. O. (1999). *Handbook Of Chemical Vapor Deposition (CVD)*. Noyes Publications, Park Ridge, New Jersey, U.S.A. (Cited on page 20.)

[Press et al., 2007] Press, W. H., Teukolsky, S. A., Vetterling, W. T., and Flannery, B. P. (2007). *Numerical Recipes*. Cambridge University Press, 3 edition. (Cited on page 101.)

[Priestley, 1981] Priestley, M. B. (1981). *Spectral Analysis and Time Series*, volume I. Academic Press. (Cited on page 17.)

[Purdy et al., 2013] Purdy, T. P., Yu, P.-L., Peterson, R. W., Kampel, N. S., and Regal, C. A. (2013). Strong optomechanical squeezing of light. *Phys. Rev. X*, 3(3). (Cited on page 127.)

[Rao, 2011] Rao, S. S. (2011). *Mechanical Vibrations*. Prentice Hall, fifth edition. (Cited on page 19.)

[Riley et al., 2006] Riley, K. F., Hobson, M. P., and Bence, S. J. (2006). *Mathematical Methods for Physics and Engineering*. Cambridge University Press, 2 edition. (Cited on page 15.)

[Safavi-Naeini et al., 2013] Safavi-Naeini, A. H., Gröblacher, S., Hill, J. T., Chan, J., Aspelmeyer, M., and Painter, O. (2013). Squeezed light from a silicon micromechanical resonator. *Nature*, 500:185. (Cited on page 127.)

[Saleh and Teich, 2007] Saleh, B. E. A. and Teich, M. C. (2007). *Fundamentals of Photonics*. John Wiley & Sons Inc. (Cited on page 75.)

[Saulson, 1994] Saulson, P. R. (1994). *Fundamentals of Interferometric Gravitational Wave Detectors*. World Scientific. (Cited on pages 14 and 24.)

[Schliesser, 2010] Schliesser, A. (2010). Cavity optomechanics with whispering-gallery mode optical micro-resonators. *Adv. At. Mol. Opt. Phys.* (Cited on page 3.)

[Schließer, 2009] Schließer, A. (2009). *Cavity Optomechanics and Optical Frequency Comb Generation with Silica Whispering-Gallery-Mode Microresonators*. PhD thesis, Fakultät für Physik der Ludwig–Maximilians–Universität. (Cited on pages 54 and 55.)

[Serra et al., 2015] Serra, E., Bawaj, M., Borrielli, A., Giuseppe, G. D., Forte, S., Kralj, N., Malossi, N., Marconi, L., Marin, F., Marino, F., Morana, B., Natali, R., Pandraud, G., Pontin, A., Prodi, G., Rossi, M., Sarro, P., Vitali, D., and Bonaldi, M. (2015). Microfabrication of large area high-stress silicon nitride membranes for optomechanical devices. arXiv:1601.02669. (Cited on page 22.)

[Sherson et al., 2006] Sherson, J. F., Krauter, H., Olsson, R. K., Julsgaard, B., Hammerer, K., Cirac, I., and Polzik, E. S. (2006). Quantum teleportation between light and matter. *Nature*, 443:557. (Cited on page 4.)

[Siegman, 1986] Siegman, A. E. (1986). *Lasers*. University Science Books. (Cited on pages 6 and 60.)

[Tabata et al., 1989] Tabata, O., Kawahata, K., Sugiyama, S., and Igarashi, I. (1989). Mechanical property measurements of thin films using load-deflection of composite rectangular membrane. In *Proceedings: IEEE Micro Electro Mechanical Systems*. (Cited on page 20.)

[Teufel et al., 2011a] Teufel, J. D., Donner, T., Li, D., Harlow, J. W., Allman, M. S., Cicak, K., Sirois, A. J., Whittaker, J. D., Lehnert, K. W., and Simmonds, R. W. (2011a). Sideband cooling of micromechanical motion to the quantum ground state. *Nature*, 475(7356):359–363. (Cited on page 3.)

[Teufel et al., 2011b] Teufel, J. D., Li, D., Allman, M. S., Cicak, K., Sirois, A. J., Whittaker, J. D., and Simmonds, R. W. (2011b). Circuit cavity electromechanics in the strong-coupling regime. *Nature*, 471(7337):204–208. (Cited on page 3.)

[The LIGO Scientific Collaboration, 2013] The LIGO Scientific Collaboration (2013). Enhanced sensitivity of the ligo gravitational wave detector by using squeezed states of light. *Nature Photon.*, 7(8):613–619. (Cited on page 2.)

[Thompson et al., 2008] Thompson, J. D., Zwickl, B. M., Jayich, A. M., Marquardt, F., Girvin, S. M., and Harris, J. G. E. (2008). Strong dispersive coupling of a high-finesse cavity to a micromechanical membrane. *Nature*, 452:72. (Cited on page 4.)

[Tsaturyan et al., 2014] Tsaturyan, Y., Barg, A., Simonsen, A., Villanueva, L. G., Schmid, S., Schliesser, A., and Polzik, E. S. (2014). Demonstration of suppressed phonon tunneling losses in phononic bandgap shielded membrane resonators for high-q optomechanics. *Opt. Express*, 22(6):6810. (Cited on page 104.)

[Uhlenbeck and Ornstein, 1930] Uhlenbeck, G. E. and Ornstein, L. S. (1930). On the Theory of the Brownian Motion. *Phys. Rev.*, 36:823–841. (Cited on page 23.)

[Usami et al., 2012] Usami, K., Naesby, A., Bagci, T., Nielsen, B. M., Liu, J., Stobbe, S., Lodahl, P., and Polzik, E. S. (2012). Optical cavity cooling of mechanical modes of a semiconductor nanomembrane. *Nat. Phys.*, 8:168–172. (Cited on page 110.)

[van Kampen, 2007] van Kampen, N. G. (2007). *Stochastic Processes in Physics and Chemistry*. Elsevier. (Cited on pages 24 and 28.)

[Verhagen et al., 2012] Verhagen, E., Deléglise, S., Weis, S., Schliesser, A., and Kippenberg, T. J. (2012). Quantum-coherent coupling of a mechanical oscillator to an optical cavity mode. *Nature*, 482:63. (Cited on page 3.)

[Villanueva and Schmid, 2014] Villanueva, L. G. and Schmid, S. (2014). Evidence of surface loss as ubiquitous limiting damping mechanism in sin micro- and nanomechanical resonators. *Phys. Rev. Lett.*, 113(22). (Cited on page 104.)

[Weis et al., 2010] Weis, S., Rivière, R., Deléglise, S., Gavartin, E., Arcizet, O., Schliesser, A., and Kippenberg, T. J. (2010). Optomechanically induced transparency. *Science*, 330:1520–1523. (Cited on page 54.)

[Wilson, 2012] Wilson, D. J. (2012). *Cavity Optomechanics with High-Stress Silicon Nitride Films*. PhD thesis, California Institute of Technology. (Cited on pages 59, 61, and 69.)

[Wilson et al., 2009] Wilson, D. J., Regal, C. A., Papp, S. B., and Kimble, H. J. (2009). Cavity Optomechanics with Stoichiometric SiN Films. *Phys. Rev. Lett.*, 103(20). (Cited on pages 4 and 64.)

[Zwickl et al., 2008] Zwickl, B. M., Shanks, W. E., Jayich, A. M., Yang, C., Jayich, A. C. B., Thompson, J. D., and Harris, J. G. E. (2008). High quality mechanical and optical properties of commercial silicon nitride membranes. *Appl. Phys. Lett.*, 92:103125. (Cited on pages 4 and 102.)

Appendix A

Calculation of the Beam Overlap Factor

Introduction

For our schemes for finding the position of the laser beam spot on the membrane we frequently need to calculate the so-called *overlap factor*, η_{nm}. Doing this numerically can be surprisingly time-consuming, so in this note we find the analytic expression.

Definitions

We define the overlap factor as

$$\eta_{nm}(x, y) := \int_{\mathcal{D}} \mathrm{d}x'\mathrm{d}y' \; \phi(x' - x, y' - y)\psi_{nm}(x', y'), \tag{A.1}$$

where $\mathcal{D}$ is the domain of the membrane, ϕ is the normalised Gaussian beam intensity profile, and ψ is the membrane mode function. We define the latter two as

$$\phi(x, y) := \frac{2}{\pi w(z_m)^2} \exp\left(-\frac{2(x^2 + y^2)}{w^2(z_m)}\right), \tag{A.2}$$

where $w(z_m)$ is the beam waist size on the membrane, and

$$\psi_{nm}(x, y) := \sin\left(\frac{n\pi}{L_x}x\right)\sin\left(\frac{m\pi}{L_y}y\right), \tag{A.3}$$

with $(n,\ m)$ being the integer excitation numbers and $(L_x,\ L_y)$ the membrane side lengths, respectively.

Calculation

As a first approximation, we will expand the domain of the integration to the entire plane. Since our optical losses from clipping on the membrane side are immeasurably small, this is a good approximation.

Next, we recognise the overlap integral to be the product of two convolutions; rewriting ϕ and ψ with obvious notation, we get that

$$\eta_{nm}(x,y) = \int_{\mathbb{R}^2} \mathrm{d}x'\mathrm{d}y'\ \phi^x(x'-x)\psi_n^x(x')\ \phi^y(y'-y)\psi_m^y(y') \tag{A.4}$$

$$= (\phi^x * \psi_n^x)(x)(\phi^y * \psi_n^y)(y). \tag{A.5}$$

Since x and y are independent variables, the two-dimensional Fourier transform of η_{nm} factorises, and by virtue of the convolution theorem

$$\mathcal{F}[\eta_{nm}](k_x,k_y) = \mathcal{F}[\phi^x](k_x)\mathcal{F}[\psi_n^x](k_x) \times \mathcal{F}[\phi^y](k_y)\mathcal{F}[\psi_m^y](k_y). \tag{A.6}$$

These Fourier transforms are readily found in a mathematical handbook to be given by[1]

$$\mathcal{F}[\phi^x](k_x) = \sqrt{\frac{2}{\pi w^2(z_m)}}\,\frac{w(z_m)}{2}\exp\left(-\frac{w^2(z_m)k_x^2}{8}\right), \tag{A.7}$$

and

$$\mathcal{F}[\psi_n^x](k_x) = \frac{\sqrt{2\pi}}{2\mathrm{i}}(\delta(k_x - n\pi/L_x) - \delta(k_x + n\pi/L_x)), \tag{A.8}$$

respectively.

As was the case for the Fourier transform, its inverse of course also factorises. The x-part of the inverse Fourier transform of the Fourier transform of η_{nm}, call it η_n^x, is then given by

$$\eta_n^x(x) = \mathcal{F}^{-1}\left[\mathcal{F}[\phi^x](k_x)\mathcal{F}[\psi_n^x](k_x)\right](x) \tag{A.9}$$

$$= \int_{\mathbb{R}} \mathrm{d}k_x \exp\left(-\frac{w^2(z_m)k_x^2}{2}\right) \tag{A.10}$$

$$\times \frac{1}{2\mathrm{i}}(\delta(k_x - n\pi/L_x) - \delta(k_x + n\pi/L_x))\exp(\mathrm{i}k_x x)$$

$$= \exp\left(-\frac{w^2(z_m)n^2\pi^2}{2L_x^2}\right)\frac{1}{2\mathrm{i}}\left(\exp(\mathrm{i}n\pi x/L_x) - \exp(-\mathrm{i}n\pi x/L_x)\right) \tag{A.11}$$

$$= \exp\left(-\frac{w^2(z_m)n^2\pi^2}{2L_x^2}\right)\sin(n\pi x/L_x). \tag{A.12}$$

[1] We distribute the pre-factor of ϕ evenly between ϕ^x and ϕ^y.

The y integral can be performed analogously and we obtain the final result that

$$\eta_{nm}(x,y) = \exp\left[-\frac{w^2(z_m)}{8}\left(\frac{n^2\pi^2}{L_x^2}+\frac{m^2\pi^2}{L_y^2}\right)\right]\sin(n\pi x/L_x)\sin(m\pi y/L_y) \tag{A.13}$$

$$=: P(w(z_m), n, m, L_x, L_y)\psi_{n,m}(x,y), \tag{A.14}$$

where we in the last line have defined the *Penalty function*, P.

Appendix B

Membrane Cleaning Procedure

Introduction

As described e.g. in section 3.7.2 and exemplified in Figure 3.25, contamination of the membrane is a very real threat to the experiment. As samples were always rather sparse in this project, it was never favourable to simply dispose of a contaminated membrane. Instead, a lot of effort went into finding ways of "reviving" seemingly "dead" membranes. Eventually, a cleaning procedure emerged in the laboratory. Here, we share this accumulated experience, expressed as a series of tips for how to handle a membrane with a dirt particle on top of it.

Do's

Acetone, also used to remove the photoresist from the membrane during the fabrication process, is the chemical of choice for day-to-day cleaning of membranes. Clamping the membrane chip with a pair of tweezers and gently stirring it in a beaker full of clean acetone is a safe and relatively efficient way of removing contaminating agents. Note, however, that acetone (even the ultra-pure spectrophotometric grade variant) upon drying leaves residues on the surface off of which it dried. This is shown in Figure B.1.

Such residuals compromise the parallelity between spacers and membrane and may, if found on the membrane, be just as detrimental to the Q-value as the dirt originally sought eradicated. Therefore, the membrane should be rinsed with milli-Q water immediately after being taken out off the acetone bath. Both steps can be repeated *ad libitum*, as long as the membrane chip is not allowed to go dry after the acetone bath.

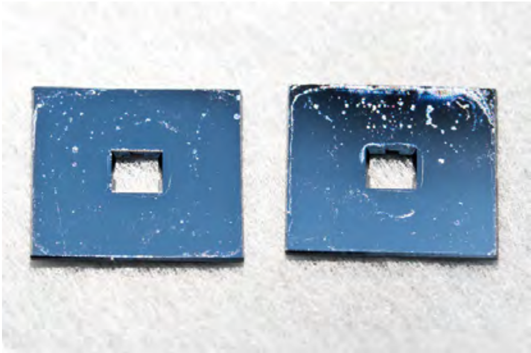

Figure B.1: Dried-up acetone residuals. Here shown on two commercial Norcada Si spacers.

Don’ts

The membrane is very small and fragile. Any attempt of mechanical dirt removal has a high risk of shattering the membrane. Using canned air to blow off dust or ultrasound baths to shake off the offending particle has proven to be almost certain ways of losing a sample.